Graduate Theses and Dissertations

Iowa State University Capstones, Theses and Dissertations

2014

An experimental investigation on wind turbine aeromechanics and wake interferences among multiple wind turbines

Ahmet Ozbay
Iowa State University

Follow this and additional works at: https://lib.dr.iastate.edu/etd

Part of the Aerospace Engineering Commons, and the Oil, Gas, and Energy Commons

Recommended Citation

An experimental investigation on wind turbine aeromechanics and wake interferences among multiple wind turbines

by

Ahmet Ozbay

A dissertation submitted to the graduate faculty

in partial fulfillment of the requirements for the degree of

DOCTOR OF PHILOSOPHY

Major: Aerospace Engineering

Program of Study Committee:
Hui Hu, Major Professor
Partha Sarkar
Eugene S. Takle
Anupam Sharma
Baskar Ganapathysubramanian

Iowa State University

Ames, Iowa

2014

TABLE OF CONTENTS Page

LIST OF FIGURES Page

LIST OF TABLES
Page

ACKNOWLEDGEMENTS

ABSTRACT

A comprehensive experimental study was conducted to investigate wind turbine aeromechanics and wake interferences among multiple wind turbines sited in onshore and offshore wind farms. The experiments were carried out in a large-scale Aerodynamic/Atmospheric Boundary Layer (AABL) Wind Tunnel available at Iowa State University. An array of scaled three-blade Horizontal Axial Wind Turbine (HAWT) models were placed in atmospheric boundary layer winds with different mean and turbulence characteristics to simulate the situations in onshore and offshore wind farms. The effects of the important design parameters for wind farm layout optimization, which include the mean and turbulence characteristics of the oncoming surface winds, the yaw angles of the turbines with respect to the oncoming surface winds, the array spacing and layout pattern, and the terrain topology of wind farms on the turbine performances (i.e., both power output and dynamic wind loadings) and the wake interferences among multiple wind turbines, were assessed in detail. The aeromechanic performance and near wake characteristics of a novel dual-rotor wind turbine (DRWT) design with co-rotating or counter-rotating configuration were also investigated, in comparison to a conventional single rotor wind turbine (SRWT). During the experiments, in addition to measuring dynamic wind loads (both forces and moments) and the power outputs of the scaled turbine models, a high-resolution Particle Image Velocity (PIV) system was used to conduct detailed flow field measurements (i.e., both free-run and phase-locked flow fields measurements) to reveal the transient behavior of the unsteady wake vortices and turbulent flow structures behind wind turbines and to quantify the characteristics of the wake interferences among the wind turbines sited in non-homogenous surface winds. A miniature cobra anemometer was also used to provide high-temporal-resolution data at points of interest to supplement the full field PIV measurement results. The detailed flow field measurements are correlated with the dynamic wind loads and power output measurements to elucidate underlying physics in order to gain further insight into the characteristics of the power generation performance, dynamic wind loads and wake interferences of the wind turbines for higher total power yield and better durability of the wind turbines sited in atmospheric boundary layer (ABL) winds.

CHAPTER 1. OVERVIEW

1.1 Problem Background

Today, approximately 20% of the energy is produced via renewable energy sources such as hydro, wind, solar, etc. (REN21 report, 2014). However, with the tremendous growth of worldwide investments in renewable technologies due to the rapid consumption of non-renewable energy sources, renewable energy sources could play a significant role in solving the world's energy demand in the future.

Wind energy has become one of the most promising renewable energy sources having great potential to contribute to the world's energy demand. Although wind is a sustainable and relatively cheaper energy resource, the amount of energy to be harnessed from the wind is versatile depending on the wind speed and direction. Therefore, it is essential to understand how to capture the energy available in the wind in a more efficient and reliable way.

Today, wind energy contributes to 4% of the total U.S. electricity generation with 62 GWs of installed wind capacity (AWEA, 2014). Furthermore, according to a report published by the U.S. Department of Energy (DOE), wind energy could contribute 20% of the nation's electricity demand by 2030. It would require the installation of additional 248 GWs of wind capacity to reach a cumulative installed capacity of 310 GWs. Moreover, the number of turbine installations should be increased to almost 7000 per year in 2017 (20% Wind energy by 2030, 2008). Therefore, large numbers of wind arrays/farms having clusters of wind turbines need to be installed onshore and offshore.

As the wind turbine components (rotating: Rotor and non-rotating: Tower and Nacelle) interacts with the incoming wind flow with stochastic behavior (due to turbulence), there is a need for better understanding of wind turbine aeromechanics, involving wind turbine aerodynamic performance and wind loads acting on a wind turbine.

An essential problem with wind turbines in wind arrays/farms is the wake produced after each turbine which expands, superimposes and impinges upon downstream wind turbines. Therefore, downstream turbines in a wind farm/array are more likely to suffer from multiple wake effects. These effects could result in up to 23% losses in the total wind farm power production (Barthelmie, et al., 2009; Dahlberg & Thor, 2009; Beyer et al., 1994). Moreover, enhanced turbulence (due to the formation of tip vortices) levels in subsequent rows of wind

farms/arrays could impose dynamic (fatigue) loads on the downstream wind turbines (Sanderse, 2009). Therefore, the factors affecting the wake dynamics within a wind farm/array need to be addressed and understood for more efficient and reliable power production.

1.2 Problem Description

Wind tunnel investigations showed that wake effects (velocity deficit and enhanced turbulence) could still be noticeable even after fifteen turbine diameters downstream of a wind turbine (Chamorro & Porte-Agel, 2009). Furthermore, Meneveau and Meyers (2012) developed a new model for wind turbine spacing which takes the interaction of wind turbines with the atmospheric wind flow inside a wind farm/array into account. They proposed that wind turbines should be placed at least fifteen turbine diameters apart for a cost-efficient power generation. However, it is not always feasible due to space and economic constraints especially for large wind turbines with a diameter greater than a hundred meters (D >100 m).

The spacing between wind turbines in current wind farm/array layouts is between six to ten turbine diameters (Sanderse, 2009). Therefore, (multiple) wake effects degrade the wind farm power production performance as a result of significant power losses in downstream turbines. In recent years, investigations purely focus on maximizing the energy production or minimizing the cost of energy within a wind farm/array. This can be achieved in several different ways. The numerical and experimental efforts primarily concentrate on the optimization of wind farms/arrays by finding the best configuration/layout or the best location for wind turbines so that the wake interference effects within a wind farm/array is minimized (Gonzalez et al., 2010; Chamorro et al., 2011). In addition, operational settings of the wind turbines could be changed (changing the pitch or yaw settings) to increase the wind farm/array efficiency (Adaramola & Krogstad, 2011). Furthermore, the wind turbines could be designed to extract more power from the wind by utilizing dual-rotor wind turbine concept (Habash et al., 2011; Shen et al., 2007).

Moreover, higher turbulence levels generated in the wake impose greater dynamic loads on the downstream wind turbines. The decay of the turbine-generated turbulence was found to be slower than the decay of the velocity deficit in the wake (Sanderse, 2009). Apart from the turbine-generated turbulence, ambient turbulence also plays a central role on the wind farm/array wake dynamics. The higher ambient turbulence levels not only impose additional

dynamic loads on the wind turbines but also promote faster wake recovery (Wu et al., 2012). There is a strong dependence between ambient turbulence levels and atmospheric stability conditions. As atmospheric stability increases (i.e. ambient turbulence levels decrease), wake effects become more persistent (Hansen et al., 2012; Zhang et al., 2013; Abkar & Porte-Agel, 2014). The lower turbulence levels will induce deep array effects (pronounced for offshore environments) within the wind farm/array, causing greater velocity deficits; hence greater power deficits for downstream turbines. Therefore, deep array effect would lead to under-prediction of wake losses in large offshore wind farms (Barthelmie & Jensen, 2010).

1.3 Literature Review

The turbulent wake structure behind a wind turbine is characterized by reduced momentum (velocity deficit) and enhanced turbulence intensity levels. The wake field is formed due to the distraction of the mean flow field as the energy available in the mean flow is partly (limited by Betz limit) harnessed by the wind turbine rotor. The momentum deficit in the wake, and the pressure loss across the wind turbine rotor could be used to determine the thrust force/coefficient which is a function of rotor tip speed ratio, blade pitch angle, etc. Thus, higher momentum deficits or higher pressure drop across the rotor will correspond to higher thrust coefficient values. As there is a strong link between thrust and power, they both depend on the incoming mean flow velocity; momentum deficit in the wake could be used to analyze these global properties. In addition, turbulent wake flow has a tangential/swirl velocity component related to the torque generated by the wind turbine rotor. The torque is dependent on the aerodynamic forces produced along the wind turbine blades, and the pressure difference between the lower (pressure) and upper (suction) sides of the blades is responsible for the lift force. The presence of the lift force leads to the formation of tip vortices shedding from the tips of the rotor blades with finite lengths. The tip vortices follow a helical trajectory with rotation opposite to the rotor. They are located in the shear (viscous) layer where strong velocity gradients occur due to the velocity difference between the wake flow and adjacent freestream flow. As the wake flow progresses downstream, the shear layer expands via the turbulent diffusion of the momentum to disperse the momentum equally. Meanwhile, tip vortices lose strength and increases in diameter due to viscous diffusion. Tip vortices formed in the shear layer are also the main sources of the turbine-generated turbulence and noise; thus

understanding the formation and evolution of tip vortices is noteworthy to provide a better understanding of unsteady wake aerodynamics. The unsteady tip vortex structures in the wake were studied extensively by using experimental and numerical methods (Whale et al., 2000; Vermeer et al., 2003; Massouh & Dobrev, 2007; Hu et al., 2011; Zhang et al., 2013; Sherry et al., 2013). Furthermore, the flow in the root section of turbine blades is highly complex due to the interaction between the rotating blades and turbine structures such as nacelle, hub and tower (Zahle & Sorensen, 2011). Therefore, root vortices is quickly dissipated due to the existence of nacelle boundary layer, tower and low-velocity region in the central wake immediately downstream of the nacelle (Sherry et al., 2013). Sherry et al. (2013) also observed the vortices produced within the nacelle boundary layer, which is of the same order of magnitude but opposite in sign to root vortices. As a result, there will be cross-annihilation of root vorticity by the nacelle boundary layer vorticity.

The wake region is considered separately as the near wake and far wake regions. The near wake region (~1D) is in the close vicinity of the rotor. The flow in the near wake is strongly affected by the presence of the rotor, and is characterized by complex coupled vortex systems, three dimensionality and unsteadiness. Vermeer (2003) stated that the most promising results about the near wake flow come from full-scale measurements. However, full-scale measurements are costly in the wind tunnels, and the blockage effects need to be considered thoroughly. Therefore, the good near wake flow data is scarce despite its value to elicit information on the turbine performance and dynamic loading. The far wake region comes after the near wake region, and the wake can be defined as fully developed wake where shear layer reaches the rotor axis. The wake induced effects start to recover in the far wake as the disturbed flow convects downstream. The wake flow reenergizes itself via the turbulent diffusion mechanism, implying the connection with the atmospheric conditions (i.e. ambient turbulence and atmospheric stability). There is also a strong linkage between ambient turbulence and atmospheric stability levels. It has been shown both numerically (Wu et al., 2012; Abkar & Porte-Agel, 2014) and experimentally (Zhang et al., 2013; Chamorro & Porte-Agel., 2009) that wake recovery rate is strongly dependent on the ambient turbulence or atmospheric stability. Turbine wakes recover faster in higher ambient turbulence levels (or in unstable conditions) due to the strong turbulent mixing. In particular, the wake recovery length is greatly reduced

in onshore wind farms with significantly higher ambient turbulence levels than offshore wind farms. Furthermore, the wake recovery is slower under night-time (stable) conditions characterized by relatively lower ambient turbulence levels (Baker & Walker, 1984). Therefore, ambient turbulence could have a huge impact on the performance of downstream turbines in large wind farms. The higher the ambient turbulence levels, the smaller the power deficit for downstream turbines. Full-scale measurements at Horns-Rev offshore wind farm showed nearly 20% recovery on the maximum power deficit of the downstream turbines at higher ambient turbulence levels (Hansen et al., 2012). Barthelmie & Jensen (2010) also estimated that wind farm efficiency at Nysted wind farm will improve up to 9% in unstable conditions with higher ambient turbulence levels.

The formation and evolution of the coherent turbulent structures (tip vortices) in the turbine wakes are also affected by the ambient turbulence levels. The vortex wake dissipation rate could be increased by increasing the ambient turbulence in the atmosphere (Sarpkaya & Daly, 1987). In addition, the tip speed ratio of the rotor will change the distance between tip vortices shedding from each blade of the rotor. As tip speed ratio increases, the distance between consecutive tip vortices decreases due to the fact that the distance a tip vortex travels in a single revolution decreases (Sherry et al., 2013).

Another expected and serious effect of the ambient turbulence is dynamic (fatigue) loading on the wind turbines. Dahlberg (1991) showed that dynamic loads on the downstream turbines are significantly increased as the spacing between the turbines is decreased at full-wake conditions. Field measurements on Vindeby farm in Denmark also indicated a significant enhancement of fatigue loading when two turbines are aligned. However, the dynamic loads under single-wake or multiple-wake conditions do not show essential differences (Sanderse, 2009).

The far wake flow is also vital to wind farm investigations where the main focus is to come up with strategies on how to minimize the wake interference effects. The objective of the research studies is to decrease the wake-induced power deficits in wind farms, thereby providing higher productivity from wind farms. However, there are also a lot of different factors need to be considered such as atmospheric conditions, spacing and alignment of wind turbines, wind turbine size and terrain characteristics. As discussed earlier, the turbulence is a

major contributor to the wake recovery in wind farms. Therefore, wind farm/array losses could be more severe in offshore wind farms where ambient turbulence levels are relatively lower (deep array effect). In this case, the simple solution to boost the wind farm power production is to increase spacing between wind turbines, thus giving the wake flow more space to recover. In addition, staggering the wind turbines can be another option to reduce wind farm/array losses without expanding the boundaries of the wind farms. Archer et al. (2013) showed through a number of different large-eddy simulations that staggering could reduce the array losses from 36% to 27%. They also found that staggering the wind turbines with more spacing would be the most efficient combination with array losses reduced down to 14%. Therefore, the annual power capacity of the wind farms can be increased by 13% to 33%. Furthermore, Chamorro et al. (2011) conducted a wind tunnel study on the flow characteristics within and above a staggered array of model wind turbines. Their results showed that staggered configuration is more efficient than the aligned one on the order of 10% under similar turbine spacing of five and four turbine rotor diameters in the streamwise and spanwise directions respectively. The maximum turbulence levels within the staggered wind farm were also found to be very similar to those generated in single-wake conditions. This reveals the fact that superimposed (multiple) wake effects are completely suppressed in staggered configuration. Markfort et al. (2012) carried out wind tunnel experiments to study the effect of turbine layout on the turbulent flow characteristics within the wind farm. They found out that the wake flow adjusts within and grows faster over the staggered farm. Thus, the flow equilibrates faster and the overall momentum absorption in staggered farm is higher than that in aligned farm. The presence of the turbulent scale within the wind farm was found to be responsible for significant portion of the vertical flux which determines the amount of power available for harvesting. They also proposed a canopy-type similarity model for wind farm optimization. This modeling treats wind farm as a canopy or added roughness element in regional scale. The experimental results were consistent with the canopy modeling, and staggering was found to lead to a larger effective roughness. Moreover, Porte-Agel et al. (2014) proposed a LES framework and validated with experimental results in atmospheric boundary layer wind tunnel. The simulation results showed strong lateral interaction between the wakes for the staggered wind farm case. They observed that the growth of wake within the staggered farm is similar to an internal

boundary layer. Furthermore, their results also showed that surface heat flux can be changed by wind farms, resulting warming in stable conditions and cooling in convective/unstable conditions near the surface.

The velocity distribution in the wake is strongly dependent on the performance of the upstream turbine. Therefore, the more power produced by the upstream turbines would mean much less power produced by the downstream turbines. Adaramola & Krogstad (2011) showed that decreasing the power output from the upstream turbine could increase the overall power of a wind farm with two turbines in aligned configuration. This is only possible when the power gain in the downstream turbine is greater than the power loss in the upstream turbine. They operated the upstream wind turbine slightly outside its optimum settings by misaligning (yawing) the turbine. However, the misalignment (yaw) angle is also critical to optimize the wind farm settings due to the fact that the power output performance of the upstream turbine decreases in relation with the cosine of the misalignment (yaw) angle (Fingersh et al., 2001; Mamidipudi et al., 2011; Pedersen et al., 2002). Therefore, they claimed that efficiency of the wind farm could be increased by about 12% by operating the upstream wind turbine at an optimum yaw angle. In addition, misaligning the upstream turbine could also reduce the turbine spacing required for a wind farm which increases the wind farm power density. However, Bastankhah et al. (2014) observed that the power production from two turbines in tandem arrangement is not significantly improved by misaligning the upstream one unless the downstream turbine is shifted laterally (staggered). They claimed that it can also decrease the fatigue loads on downstream turbine by completely deflecting the wake away. Furthermore, Gebraad et al. (2014) used a novel parametric model to optimize yaw settings of the upstream wind turbines in a 3x2 wind array, and optimal yawing was found to increase the power output from the wind array by 13%.

The performances of the wind turbines in onshore wind farms are also significantly affected from the topology of the terrain. Wind turbines could be installed over complex terrains such as hills, ridges, escarpments, etc. as well as flat terrains, of which the flow characteristics are very well known. However, the flow characteristics over complex terrains are versatile, and characterized by speed-up effects, flow separation and anisotropic turbulence. Wood (2000) described the historical development of our understanding of turbulent flow over complex

terrains, and discussed the application of LES technique to flow over hills. An extensive review of wind flow over complex terrains was given by Bitsuamlak et al. (2004). They have done a comparative study using existing experimental (both wind tunnel and field) and numerical studies on the wind flow over hills, escarpments, valleys and other complex terrain configurations. In general, numerical results were found to agree better with the field data on the upstream as opposed to the downstream sides of the complex terrains. Although the wind speed-up predictions mainly rely on physical simulations for complex terrain situations, the agreement between numerical simulations and wind tunnel tests was found to offer a promising future for the computational approach. Furthermore, the size of discrepancy between results was found to be larger near the steep hilltop due to the presence of flow separation and recirculation region for which isotropic turbulence models may not apply. The size of the separation/recirculation region behind two-dimensional hills was found to increase as the hill gets steeper (Kobayashi et al., 1994; Ferreira et al., 1995). Moreover, Kobayashi et al. (1994) studied the effects surface roughness on the wind flow pattern over hills comparing forested and non-forested two dimensional hills. Lun et al. (2003) also studied the flow around smooth and rough two dimensional hills. They both found out that the recirculation region behind the non-forested (smooth) hill has a much thinner profile than that behind the forested (rough) hill, thus having more momentum to overcome the adverse pressure gradient. Therefore, separation region was found to extend farther downstream for the forested (smooth) case.

The recirculation region behind the hill, characterized by greater velocity deficits and turbulence levels, then gets stronger as the hill gets steeper and rougher. Although the wind turbines closer to the hilltop will experience higher wind speeds (speed-up), the turbines on leeside of the hill will suffer from great power deficits and enhanced dynamic loading. Therefore, placing the wind turbines over complex terrains is very critical in terms of their power output performance and fatigue lifetimes.

Considering all the underlying factors affecting the performances and loadings of wind turbines in wind farms, researchers focus on wind farm optimization using different mathematical models or numerical algorithms (Samorani, 2013; Villarreal et al., 2011; Gonzalez et al., 2010; Perez et al., 2013). In addition, Chamorro et al. (2014) proposed using variable-sized wind turbines for wind farm optimization. They performed wind tunnel

experiments using an array (3x8) of variable-size wind turbines in a boundary layer flow developed over both a smooth and rough surfaces under neutrally stratified thermal conditions. They suggested that wind turbine size heterogeneity introduces distinctive flow characteristics in comparison to its homogeneous counterpart. They observed reduced levels of turbine-induced turbulence which may have positive effect on turbine dynamic loading. In addition, surface roughness (inducing mechanical turbulence) was found to impact velocity recovery and spectral content of the turbulent flow within the wind farm. After all, wind farm optimization still remains a biggest challenge with all these factors mentioned here to consider.

Wind turbines can also be optimized to harness more energy from the wind. Today, most of the commercial horizontal axis wind turbines in modern wind farms are single-rotor wind turbines (SRWT). The maximum energy conversion efficiency for a conventional SRWT is limited by Betz limit which is around 59%. However, in practice, today's best aerodynamically designed modern SRWT systems can only extract up to 50% proving the fact that half of the energy in the wind goes unharnessed. Therefore, dual-rotor Wind Turbine (DRWT) concept has been suggested in recent years. This concept is based on installing an additional rotor in the near wake of front rotor with back-to-back configuration. Thus, a second rotor in the back can exploit the unharnessed energy in the near wake of the front rotor thereby increasing the total energy generation from the system. Furthermore, the rotors in DRWT are installed with counter-rotation concept such that they rotate at opposite directions, therefore the back rotor take advantage of the circumferential velocity induced in the wake of the front rotor. That benefit is more pronounced in DRWT systems where rotors are installed very close to each other.

A prototype of 6 kW DRWT was built in California and completed field testing in 2002 (Appa, 2002). The results indicated that DRWT system could extract additional 30% more power from the same wind stream, compared with a conventional SRWT design. Another study of the field measurements of a 30 kW prototype DRWT also showed that the power increase of the DRWT system will reach about 21% over a conventional SRWT system at a rated wind speed of 10.6 m/s (Jung et al., 2005). More recently, a wind tunnel study with a small-scale DRWT system was conducted by Habash et al. (2011) and they found out that the DRWT

system can produce up to 60% more energy than a SRWT system of the same type and was capable to reduce cut-in speed while maintaining the turbine performance.

1.4 Wind Tunnel Testing and Limitations

Wind tunnel facilities have been widely used to study the aeromechanics of the wind turbines as well as the wake interference effects within different wind farm layouts. The main advantage of wind tunnels is their capability to produce well-controlled flow conditions. As wind turbines operate in the atmospheric boundary layer, it is also important to simulate these real life conditions in the wind tunnel. Therefore, atmospheric boundary layer wind tunnels are used to generate environmental boundary layer winds. The wind speed profile and flow turbulence characteristics can then be adjusted accordingly depending on the terrain type required for the experiments.

The vertical profile of the horizontal wind in the wind tunnel can be described by the logarithmic law and the power law. Although the logarithmic law has a scientific foundation, empirically derived power law is used more often. In the logarithmic law, wind speed variation with height is dependent on surface roughness and atmospheric stability. However, measuring the friction velocity and the stability parameter in the wind tunnel or in the field is not so easy; therefore researchers mostly rely on the power law. If neutral stability conditions are assumed, wind speed can be determined only from the surface roughness. Manwell et al. (2003) and Wieringa (1992) classified the terrains according to their surface roughness length. As the terrain roughness increases, surface roughness length increases.

The power law uses power law exponent to relate the normalized wind speeds to normalized heights. Wind speed and height is normalized with respect to the reference values (reference height is generally taken as ten meters or the hub height). The power exponent is also a function of surface roughness and stability. The power exponent can be assumed approximately 1/7, or 0.14 under neutral stability conditions. However, it could significantly change depending on the roughness elements impeding the near-surface wind. The value of power exponent could be as low as 0.10 - 0.11 (Hsu et al., 1994; Choi, 2009) for offshore applications and it could go up to 0.362 for city centers surrounded by tall buildings (Choi, 2009). In addition, Mwanyika et al. (2006) showed that the power law exponent can show variability throughout the year, and even it can change during the day.

The atmospheric turbulence can be affected from the surface roughness (due to the presence of buildings, trees, etc.) and thermal stability (due to surface heating – convective or unstable; and surface cooling – stable effects during the day). These effects can also change the wind shear profile of the atmospheric boundary layer wind. The mechanical turbulence produced by the surface roughness elements will induce wind shear closer to the surface, thereby leading to the formation of highly turbulent eddies at different length scales. The thermal turbulence produced depending on the diurnal changes in the atmospheric stability conditions. Wharton et al. (2012) showed that day-time conditions are unstable or convective with higher atmospheric turbulence levels, whereas the night-time conditions are stable with lower atmospheric turbulence levels. They classified the atmospheric stability conditions from strongly stable to strongly convective. They also claimed that wind shear in stable conditions is higher than that in unstable or convective conditions.

The mechanical turbulence in atmospheric boundary layer wind tunnel can be produced through roughness elements such as isosceles triangle-shaped spires, which are equally distributed at the inlet of the test section, wooden blocks and chains, which are installed on the wind tunnel floor. The stability conditions can be changed either by heating or cooling the floor or the airflow. The convective boundary layer conditions in Zhang et al. (2013) were generated by cooling the airflow and heating up the test section floor. The vice-versa can be done to simulate the stable conditions. Otherwise, the neutral-stability conditions were assumed in atmospheric boundary layer wind tunnels.

In wind tunnel experiments, scaled models are used for testing. Therefore, dimensionless similarity parameters (i.e. geometric, dynamic and kinematic) need to be used to match the conditions in the field. The geometric similarity requires all the geometric dimensions scaled down proportionally. The limitation to the geometric scaling is the model to tunnel ratio or the blockage ratio. The suggested upper limit is up to 10% to ensure the free expansion of the wake without any interference on the measurements (Spera, 1994; Guglsang, 2004). The dynamic similarity requires all the forces acting on the model scaled proportionally, in other words the Reynolds number similarity. Reynolds number is the ratio of dynamic forces to viscous forces. However, the wind turbine models used in wind tunnel testing generally have significantly lower Reynolds numbers than large-scale wind turbines in the field. Reynolds number based

on the blade chord length was found to have a significant effect on wind turbine power output performance (Alfredsson et al., 1982; Medici et al., 2006), and Chamorro et al. (2011) claimed that wake flow statistics would be independent of the Reynolds number at around $Re_d \approx 9.3*10^4$, where Re_d is based on the diameter of the model turbine and turbine hub height velocity. Finally, the kinematic similarity or wake similarity requires the tip speed ratio match. Tip speed ratio is the ratio of the tangential speed at the blade tip to the turbine hub height velocity. It is a key parameter for the wind turbines since it characterizes the power output efficiency, blade loading, wake structures, and even the acoustic noise levels. Furthermore, tip speed ratio of the wind turbine rotor can be controlled depending on the wind flow situations.

1.5 Research Objectives

As mentioned previously, there are several factors affecting the performance and loading of the wind turbines within large wind farms/arrays. Therefore, it is important to know how these factors can affect the wind turbine/farm dynamics, and how wind turbines interact with each other and their surroundings. The present thesis will focus on the effects of;

- The terrain topography (complex terrain – 2D Ridge with different geometries)
- The oncoming flow turbulence character
- Turbine layout (aligned and staggered) and spacing
- Operating conditions of the wind turbines (misalignment/yaw)
- The wind turbine optimization (DRWT concept)

on the wind turbine performance/loading and wake development. These effects are going to be extensively investigated in the following chapters.

CHAPTER 2. AN EXPERIMENTAL INVESTIGATION ON THE PERFORMANCES OF WIND TURBINES SITED OVER NON-FLAT (2D-RIDGE) TERRAINS

2.1 Introduction

Wind energy, as a renewable and clean energy source, has become the center of attention in recent years due to its vast potential and availability. The U.S. Department of Energy (DOE) set a target of producing 20% of nation's electricity from the wind by 2030. Thus, exploitation of areas with greater wind potential such as deep offshore and mountainous onshore terrains is of great importance for the role of wind in the nation's energy portfolio. Despite the accelerated offshore wind energy development, it is foreseen that the contribution of the onshore market will remain larger than the offshore market for the next decade. Therefore, onshore wind farms will continue to play a central role in the nation's wind energy market.

It is crucial to know the atmospheric boundary layer wind characteristics in a proposed wind farm site. In particular, for the onshore terrains, the characteristics of the surface winds could significantly change depending on the local topography. Therefore, the wind speed and direction along with its turbulence characteristics are subject to variability based on the complexity of the terrain. In addition, the flow measurements over non-flat terrains are often influenced by local, dynamically- or thermally-induced convection. There have been numerous studies on the homogenous (straight-line) surface wind characteristics over flat terrains and their effects on the wind turbine/array power production. However, there is still too much to learn about the flow characteristics over non-flat terrains such as hills, ridges and escarpments and their effects on the wind turbines/arrays.

The flow over the non-flat terrains such as hills or ridges will accelerate and experience higher wind speeds, known as speed-up effect, on the top of the hills or ridges. A number of studies on the flow over hills focused on the behavior of the speed-up effect with different atmospheric conditions and hill geometries (Jackson and Hunt, 1975; Kim and Lee et al., 1997). Furthermore, Arya et al. (1987) reported that speed-up of the flow on the hilltops is proportional to the average slope and largest speed-ups are observed over hills of moderate slope. The hills with moderate slope don't have any significant separation on the lee side, and

with further increase in slope, the flow on the lee side of the hill starts to separate and produces a wake characterized by reduced mean flow speed and enhanced turbulence. Behind long steep ridges, the wake region may extend to ten hill heights in the downstream direction (Arya, 1988). It was also stated by Kaimal and Finnigan (1994) that both for naturally shaped and triangularly shaped two-dimensional ridges, the critical angle for steady separation is around 18°-20°. Based on the previously mentioned studies, the flow characteristics (i.e., wind speed and turbulence) could greatly differ at various locations of the hilly terrain, causing significant variations in the power output performance of the wind turbines sited along the hilly terrain. Moreover, the versatile flow turbulence along the hill/ridge could be of great importance in order to evaluate the effects of the terrain topography on the dynamic (fatigue) loads of the wind turbines. As a result, the atmospheric boundary layer wind flow characteristics over hilly terrains and the interaction of the terrain induced flow structures with wind turbines need to be fully understood.

The wind farm/array power output performance could be greatly reduced due to the wake interferences among multiple wind turbines. Thus, wind farm optimization has been extensively studied to minimize the wake effects under different atmospheric boundary layer wind conditions. However, majority of these research studies were carried out on a simplified topology (i.e., flat terrain). Recently, Barthelmie et al. (2007) and Politis et al. (2012) evaluated the performance of CFD models and examined the development of turbine wakes in non-flat terrains. Furthermore, Makridis (2012) worked on the modelling of real wind farms over non-flat terrain and validated his results with full-scale measurements. He stated that the linear wake models proposed for the wind farms would give errors in cases of non-flat terrains due to arising non-linearities. Thus, there is still limited knowledge of how a wind farm operates in a non-flat terrain environment. As large-scale wind farms are installed in non-flat terrain environments, the need for more comprehensive studies on the wake development over these terrains arises.

In the present work, a wind tunnel study was conducted to assess and investigate the boundary layer wind flow characteristics over two dimensional Gaussian hill models with different geometries. Furthermore, power output performance of the wind turbines along with the dynamic wind loads acting on them were quantified so as to fully understand the effect of

the terrain topology on the wind turbine performance and loading. Moreover, non-flat terrain wind farms were simulated by placing five wind turbines along the two Gaussian hill models with different geometries to characterize the wake interactions, and evaluate the performance of the wind farms over non-flat terrains. The experimental (quantitative) results from these terrains were then compared to those obtained from the simple (flat) terrain. These results could also be used for the validation and verification of the numerical simulations.

2.2 Experimental Set-up and Procedure

The experimental study was performed in the Aerodynamic/Atmospheric Boundary Layer (AABL) Wind Tunnel located at the Aerospace Engineering Department of Iowa State University. The AABL wind tunnel, as shown in Figure 2-1, is a closed-circuit wind tunnel with a test section of 20 m long, 2.4 m wide and 2.3 m high, optically transparent sidewalls, and a capacity of generating a maximum wind speed of 45 m/s in the test section. The triangular spires at the beginning of the test section and the wooden blocks on the wind tunnel floor were used to simulate the flow conditions similar to those observed in typical onshore boundary layer winds. The tunnel ceiling was also adjusted along the length of the test section so as to ensure zero pressure gradient along the flow direction.

Figure 2-1 AABL wind tunnel test section

Figure 2-2 gives the measured normalized mean flow velocity (with respect to the hub height velocity) and turbulence intensity profiles of the onshore boundary layer wind simulated in the wind tunnel. As shown in Figure 2-2(a), the normalized mean flow velocity profile fits well with the power and logarithmic laws, which could be used to define the boundary layer profiles over open terrains. The power law exponent for an atmospheric boundary layer wind

over an open terrain in nature usually ranges from 0.1 to 0.2 according to ASCE standard (ASCE 2005). The power law exponent of the curve fitting to the present measurement data is 0.16, representing the onshore boundary layer wind over open country terrain with low scrub or scattered trees based on ASCE standard (Zhou, 2002). Furthermore, the turbulence intensity, as shown in Figure 2-2(b), at the turbine hub height is about 16%.

(a)   **(b)**
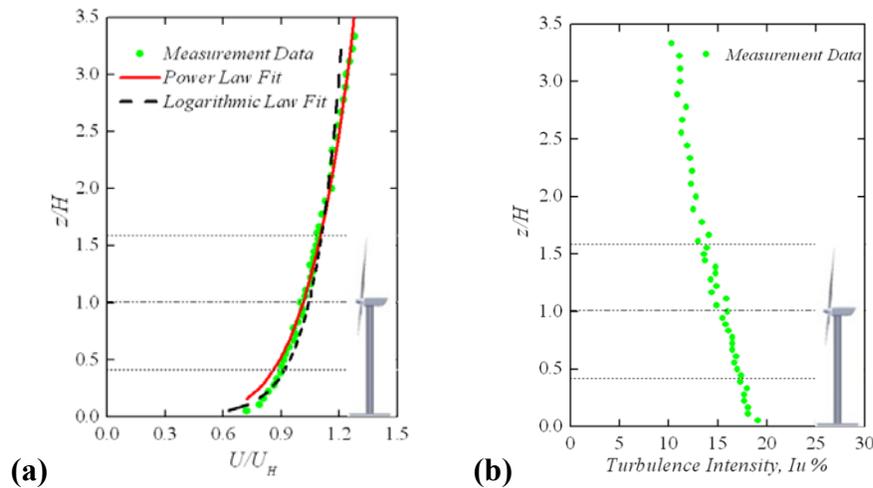
Figure 2-2 Atmospheric boundary layer profiles (a) mean streamwise velocity; (b) turbulence intensity

Figure 2-3 shows a schematic of the three-bladed horizontal axis wind turbine model. The model turbine has a rotor radius of 140 mm and hub height of 226 mm (see Table 2-1 for detailed design parameters). With the scale ratio of 1:320, the test model would represent a commercial wind turbine in a wind farm with a rotor diameter about 90 m and a tower height about 80 m. The ratio of the blade swept area to the cross-section area in the wind tunnel was found to be less than 1.5%. Thus, blockage effects for this study would be very small, and could be neglected. The blade sections of the wind turbine model were generated by mathematically applying a spline in tension to interpolate between the defined input stations based on the ERS-100 wind turbine blade prototype developed by TPI Composites. A constant circular cross section from the root of the blade to a distance of 5% radius of blade (R) and three NREL airfoils (S819, S820, S821) placed at various locations as inputs were used to generate the blade profile. The S821 root airfoil was used between 0.208R and 0.40R, the S819 primary airfoil was positioned at 0.70R, and the S820 tip airfoil was specified at 0.95R. Further information about the ERS-100 rotor blades is available at Locke et al. (2003).
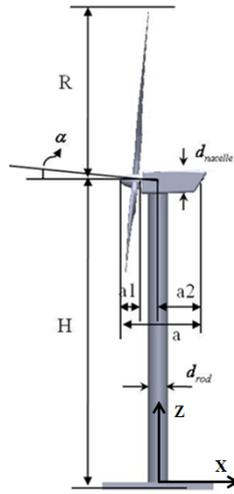
Figure 2-3 Schematic of the tested wind turbine model

Table 2-1 The primary design parameters of the wind turbine model

Parameter	R	H	d_{rod}	$d_{nacelle}$	a	a	$a1$	$a2$
Dimension (mm)	140	226	18	18	5°	78	15	50

The two-dimensional hill models were made of wooden frames covered with thin film surface. The geometry of the two-dimensional hill is defined by the following Gaussian curve:

$$z = h * \exp\left[-0.5\left(\frac{x}{\sigma} \right)^2 \right], \sigma = L/1.1774 \qquad (1)$$

where h=285 mm is the height of the hill top from the wind tunnel floor, L is the length measured in the x direction between the hill heights from $h/2$ to h. The hill slope can be defined as $s=h/(2L)$. The 2-D hill models with slopes of s=0.25 and s=0.50 were tested in the current study (see Figure 2-4). According to the study of Mason and King (1985), the critical hill slope for the flow separation is around s=0.3. Therefore, this investigation could help see the differences in the flow characteristics over hills with different geometries, and investigate the wind turbine/array performances sited at five different locations along the hilly terrain, as shown in Figure 2-4. The distance between adjacent positions is 3D, where D is the diameter of the model wind turbine rotor. Moreover, the results from the simulated non-flat terrain wind farms (with five wind turbines in tandem arrangement) were compared with those obtained from the baseline (flat terrain) wind farm.
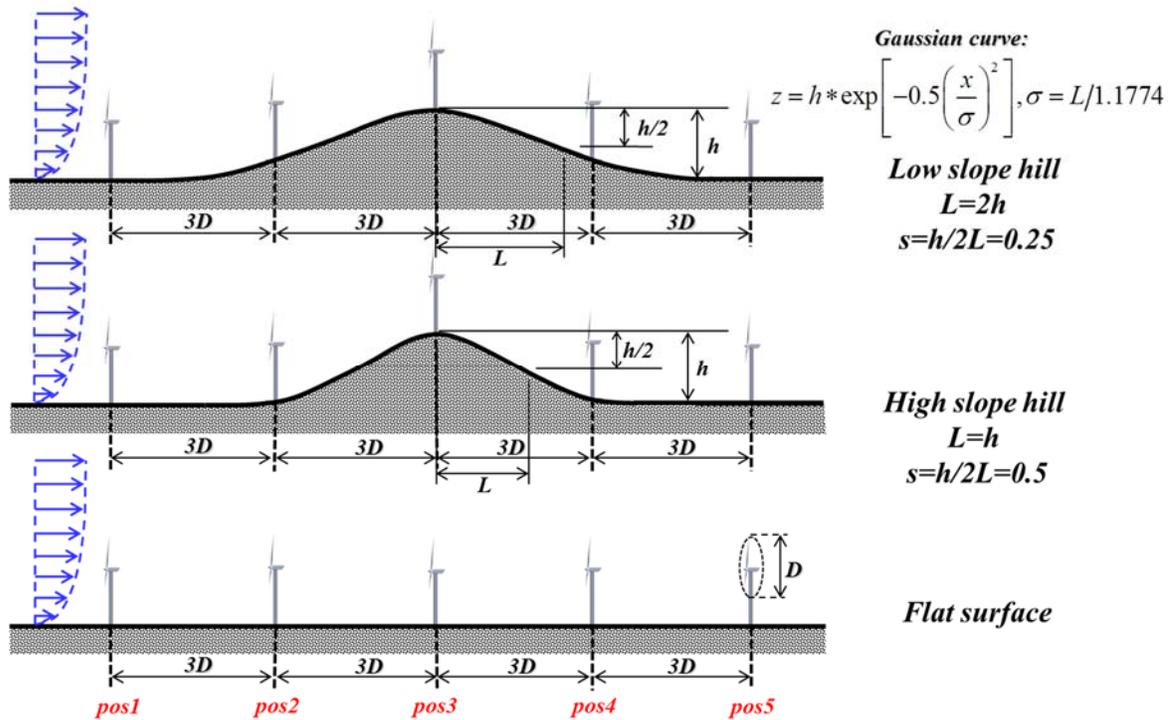
Figure 2-4 Schematic of the experimental layouts

In the present study, the rotor blades were mounted on a turbine hub with a pitch angle of 3.0 degrees (i.e., θ=3.0 deg.), and a DC electricity generator was installed in the nacelle of the model wind turbine, which would produce electricity as driven by the rotating blades. The voltage readings from the generator were used to calculate the electrical power output from the model wind turbine. The voltage data were acquired at a rate of 1 kHz for 180 seconds under optimum electrical loading condition (maximum efficiency).

The JR3 load cell with transducer full scale of 40N and an accuracy of ±0.25% was used to measure both the thrust (axial) and bending loads acting on the model wind turbine. An aluminum rod was used as the turbine tower, and it was connected to the high-sensitivity JR3 force-moment sensor through a hole on the wind tunnel floor. The thrust coefficient (i.e., the force coefficient along x direction) and bending moment coefficient (i.e., the moment coefficient along y direction) of the model wind turbines were calculated by using the expressions of $C_T = T / (0.5 \rho U_{Hub}^2 \pi R^2)$ and $CM_y = M_y / (0.5 \rho U_{Hub}^2 \pi R^2 H)$ respectively, where ρ is the air density, R is the radius of the wind turbine rotor, H is the hub height of the wind

turbine and U_{Hub} is the velocity at the turbine hub height. For each tested case, the wind load data were acquired for 120 seconds at a sampling rate of 1 kHz.

The flow characteristics including the mean flow velocity and turbulence intensity were measured by using a cobra probe (Turbulent Flow Instrumentation Pty Ltd) with an accuracy of 0.5%. For each measurement location, the data were sampled at a rate of 1.25 kHz for 60 seconds.

2.3 Results and Discussions

The mean flow streamwise velocity distribution plots were given at five pre-selected positions (pos1 and pos2 - uphill, pos3 - top, pos4 and pos5 - downhill) along the low slope and high slope 2-D ridges/hills (see Figure 2-5 and Figure 2-6). The velocity profile of the oncoming flow over the flat terrain (baseline) was also plotted for comparison. The velocities were normalized with respect to the oncoming flow hub height velocity (U_H) over the flat terrain.

As the flow approaches towards the upwind side of the hill, it was found to decelerate due to the accumulated pressure becoming more evident closer to the hill. The significant reduction (in comparison to the baseline profile) in the flow velocity was observed in the region below the turbine hub height. However, the slope of the hill was found to be an essential factor affecting the rate of reduction in the flow velocity, and the extent of the low momentum zone on the foot of the uphill. As shown in Figure 2-5 and Figure 2-6, these effects could be more pronounced towards the foot of the high slope hill. Thus, as the hill slope increases, the approaching uphill flows, especially on the foot of the hill (i.e., pos2), could experience higher velocity deficits below the turbine hub height due to the accumulated pressure, and low momentum zone could extend greater vertical distances.

The flow, then, accelerates as it climbs the top of the hill. The low momentum zone below the hub height was found to diminish towards the top of the hill, and speed (ramp)-up effects could dominate the flow field as the flow converges. The speed-up effect was found to reach a maximum near the ground at the top of the hill (pos3) with a distinct enhancement in the flow velocity as compared to the flow field over the flat terrain. This enhancement can be expressed
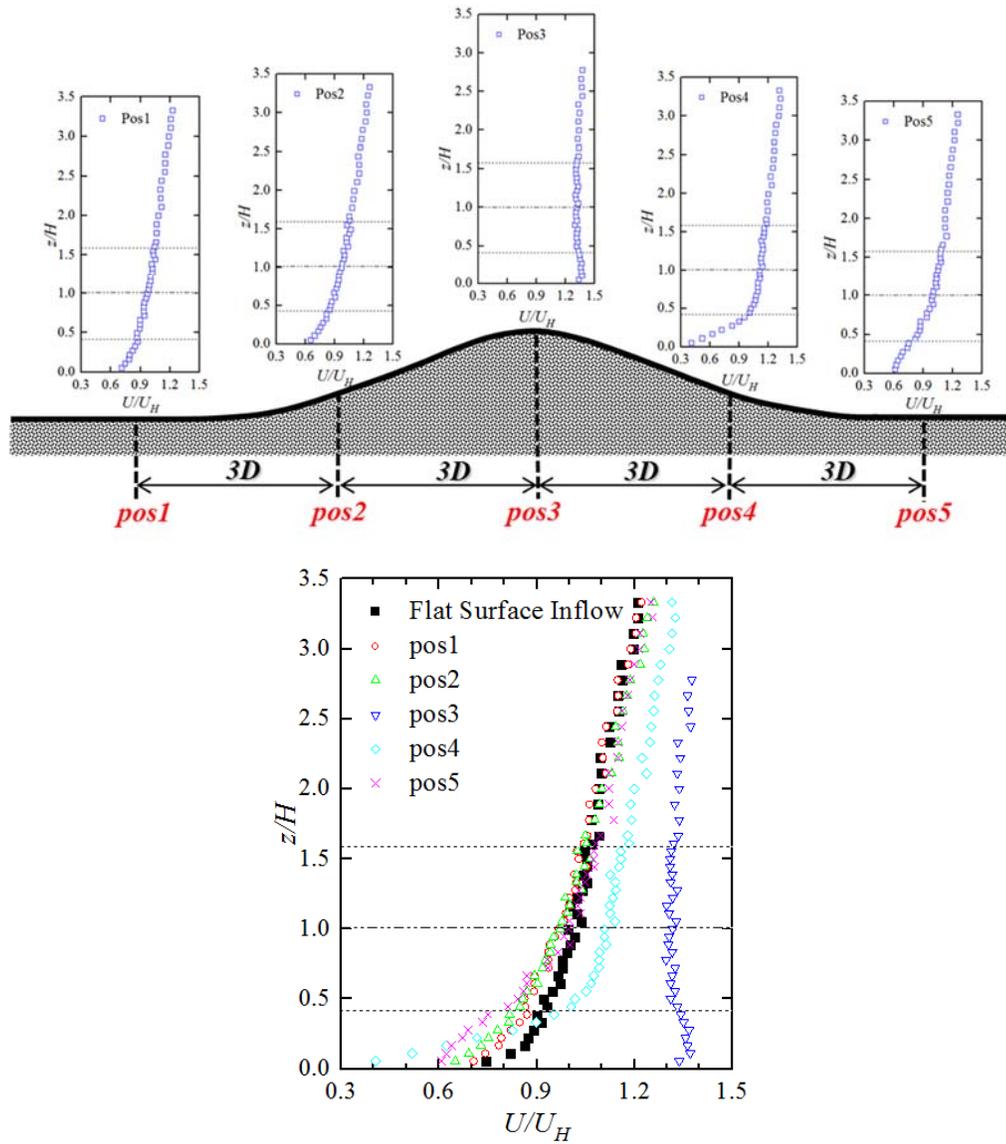
Figure 2-5 The mean flow normalized velocity distributions over a *low slope* 2-D hill

Table 2-2 The performance and loading of a model wind turbine over a *low slope* 2-D hill

Wind turbine position	Position 1	Position 2	Position 3	Position 4	Position 5
Normalized power outputs	0.92	0.93	1.82	1.28	0.94
Thrust coefficient, C_T	0.140	0.145	0.301	0.160	0.128
Bending moment coefficient, C_{MY}	0.144	0.144	0.280	0.163	0.143
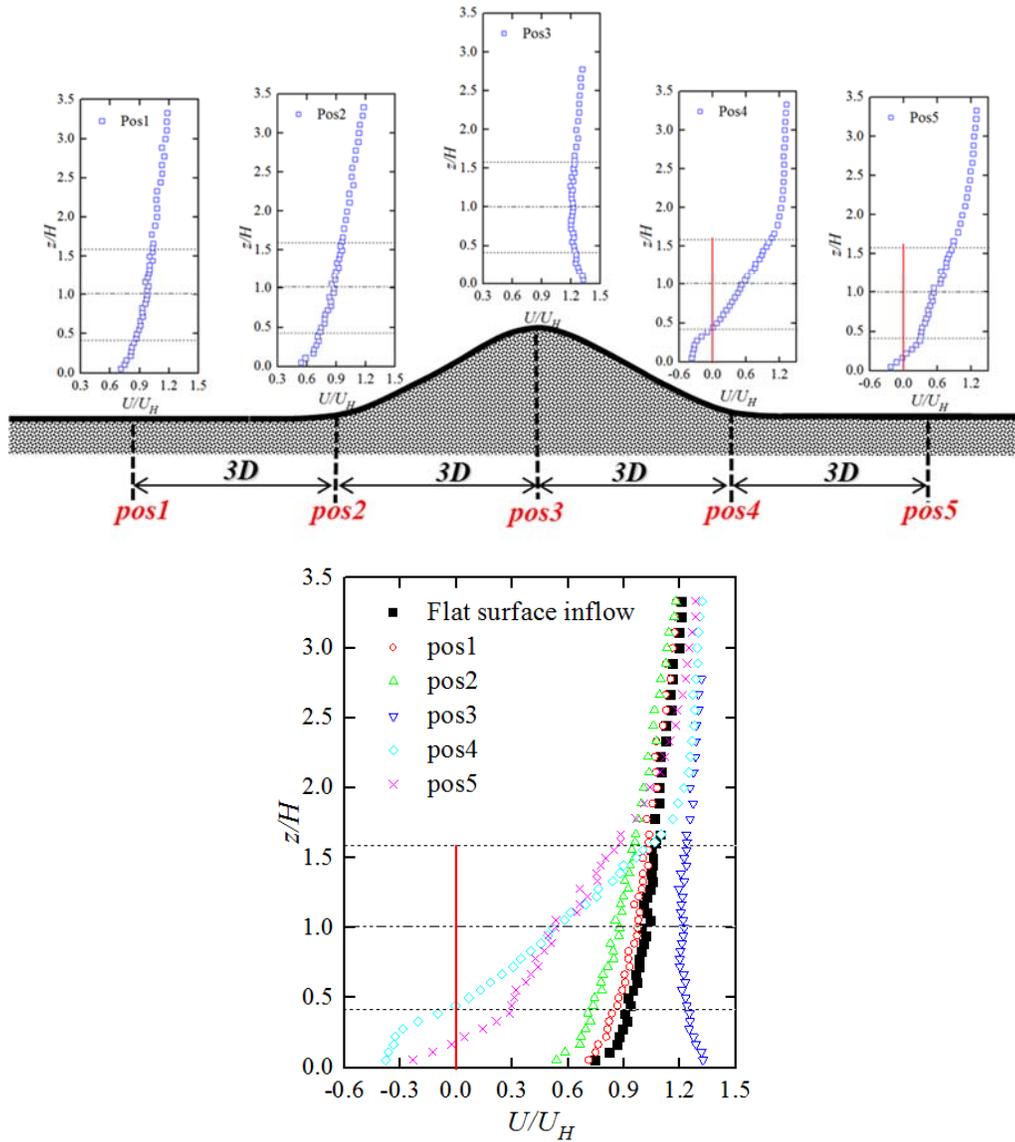
Figure 2-6 The mean flow normalized velocity distributions over a *high slope* 2-D hill

Table 2-3 The performance and loading of a model wind turbine over a *high slope* 2-D hill

Wind turbine position	Position 1	Position 2	Position 3	Position 4	Position 5
Normalized power outputs	0.92	0.79	1.45	0.04	0.20
Thrust coefficient, C_T	0.140	0.115	0.252	0.015	0.042
Bending moment coefficient, C_{MY}	0.144	0.124	0.232	0.017	0.045

as the fractional change in mean flow velocity with respect to the approaching baseline profile, also identified as the fractional speed-up ratio ($\Delta U/U_{hub}$). The maximum fractional speed-up ratio measured at the hilltop was found to be around 0.6 near the ground ($z/H \approx 0.055$). Furthermore, the fractional speed-up ratios in all measurement points above the hilltop indicates increased velocities compared to the corresponding heights above the flat terrain, even at the uppermost measured point ($z/H = 2.78$) where the fractional speed-up ratio is around 0.23.

The mean flow velocity distribution would become more like a uniform flow at the top of the hill with wind shear levels considerably less than the baseline profile. Therefore, wind turbines can operate under almost uniform flow over the entire rotor area which is a very favorable condition for wind turbines (Rokenes, 2009).

As reported by Arya et al. (1987), the speed-up of the flow on the hilltop was proportional to the slope of the hill. Rokenes (2009) showed that speed-up increases further with increasing slope. However, the separation in the wake region (downhill) of the high slope hill (s >0.3) could significantly change the flow field around the hill; even limit the speed-up effects on the hilltop (Holmes, 2007; Rokenes, 2009). Therefore, the speed-up effects near the ground were found to be mitigated for the high slope hill case. However, in general, the streamwise velocity profiles on the hilltops are very similar for the low slope and high slope cases due to the fact that both hilltops have the same height.

The separation region on the lee side of the hill (downhill) could be more susceptible to the strong adverse pressure gradients depending on the slope of the hill since the downhill flow characteristics over a 2D hill were found to be strongly dependent on the slope. As shown in Figure 2-5, no flow separation was observed on the leeward side (pos4 and pos5) of the low slope hill. However, the speed-up effects were found to gradually decrease downhill, and the velocity profile eventually would return to the baseline inflow profile further downstream of the hill (shadowing effect from the hill could still be seen from the velocity profile at pos5 below $z/H < 1.0$). For the high slope hill, as shown in Figure 2-6, the separation on the leeward side (pos4 and pos5) was obvious with greater velocity deficits extending up to the vertical region of $z/H \approx 1.5$. Arya (1988) stated that the wake region behind steep hills, characterized by reduced mean flow velocity and enhanced turbulence, may extend up to ten hill heights in

the free stream flow direction. It was also shown that both for naturally shaped and triangularly shaped 2D ridges/hills, the critical angle for steady separation is around 18˚- 20˚ (Kaimal and Finnigan, 1994). Moreover, Hyun Goo Kim et al. (1997) proposed a critical slope of s = 0.3 for the flow separation over 2D hills.

The performances of an individual model wind turbine were tested at pre-selected positions along the low slope and high slope hills. The normalized power output performances (with respect to the power output performance of the model wind turbine in the flat terrain) of the model wind turbine along with the mean (thrust and bending) wind loads acting on the turbine at prescribed positions (see Table 2-2 and Table 2-3) were found to be in good agreement with the velocity profiles shown in Figure 2-5 and Figure 2-6.

The mean flow velocity distribution along the hill was the decisive element on the wind turbine performance and loading. As previously mentioned, the deceleration due to accumulated pressure below the hub height (foot of the uphill) and the flow separation (downhill) were found to play a central role on the velocity deficit depending on the geometry of the hill. As shown in Table 2-2 and Table 2-3, the effects of the accumulated pressure and flow separation on the turbine performance and loading were far more pronounced along the high slope hill. The power deficit due to the accumulated pressure would be around 7% - 8% for the low slope hill; however, it would reach 21% in the high slope hill. As the slope increases, the flow deceleration was found to be more severe towards the upwind foot of the hill. Furthermore, the model wind turbines on the leeward side of the high slope hill (pos4 and pos5) were observed to either operate very poorly or stop due to the dominance of strong adverse pressure gradients. The flow separation in the wake region of the high slope hill could have severe impacts on the performances of the downhill wind turbines. Moreover, the performance of the model wind turbine sited in the leeward side of the low slope hill (pos4 and pos5) was found to gradually decrease downhill, and eventually become quite similar (slightly less - 6% - due to the shadowing effect from the hill at pos5) to the performance of the model wind turbine in the flat terrain.

The model wind turbine was found to perform much better on the top of the hill (i.e., pos3) due to the previously mentioned speed-up effect. As shown in Table 2-2 and Table 2-3, the normalized power output of the model wind turbine sited at the hilltop could reach 1.82 for the

low slope hill, implying a power generation almost twice as much. However, it was around 1.45 for the high slope hill corresponding a 20% less power generation as compared to the low slope hill. This is associated with the strong adverse pressure gradient (flow separation) in leeward slope, influencing the whole flow field and mitigating the speed-up effects. In addition, the ascending flow has a non-zero vertical velocity component, which is much stronger in steeper slopes. Therefore, it can also play part on degradation of speed-up effects for the high slope case.

The thrust and bending moment coefficients of the model wind turbine sited at pre-selected positions were also given in Table 2-2 and Table 2-3. It should be noted that these coefficients were normalized using the same reference velocity (the turbine hub height velocity U_H in the flat terrain). The mean wind loads acting on the model wind turbine at pre-selected positions were found to be in good agreement with the power output measurements since they are strongly dependent on the mean flow velocity profile. The prediction of the mean wind loads on a wind turbine is of great importance in the mechanical design phase; however, the effects of the unsteady turbulent flows should also be taken into account in terms of the dynamic loads. Therefore, wind turbines sited in non-flat terrains would be more vulnerable to these fluctuating (dynamic) loads due to the higher turbulence intensity levels observed in these environments. The effects of dynamic loads on a wind turbine could be severe (reduced lifetime) since dynamic loads not only contribute to the extreme wind loads but also impose fatigue loading on wind turbine components.

The intensity of thrust load fluctuations were correlated with the turbulence intensity measurements at prescribed positions along the low and high slope hills. The intensity of thrust load fluctuations were defined, analogous to the power fluctuation calculations proposed by Rosen (1996), as the ratio of the standard deviation (σ_{CT}) in instantaneous thrust loads to the mean thrust loads (C_T). Figure 2-7 shows the mean flow (streamwise) turbulence intensity profiles at prescribed locations along the low and high slope hills. The turbulence intensity profiles over the flat terrain were also given for comparison. The flow turbulence along the hill was found to show distinct characteristics depending on the geometry of the hill. As shown in Figure 2-7, the enhancement in the turbulence intensity levels was more noticeable and intense at the high slope hill, especially on the foot of the hill (pos2) and on the leeward side of the hill

(pos4 and pos5). Furthermore, the wake flow behind the high slope hill (pos4 and pos5) was found to be highly turbulent due to the adverse pressure gradient (flow separation). The vertical expansion of the separated region with higher turbulence levels was evident for the high slope hill (see Figure 2-7) expanding up to z/H ≈ 2.5 further downstream of the leeward slope (pos5); on the contrary, for the low slope hill without the flow separation in the wake, higher turbulence levels were found to appear in the region closer to the ground expanding up to the turbine hub height level (z/H ≈ 1.0). The intensity of thrust fluctuations data for the low and high slope hills, as tabulated in Table 2-4, indicate that fluctuating (dynamic) loads acting on a wind turbine sited in the wake (downhill) of the high slope hill could dramatically increase in agreement with the enhanced turbulence levels on the leeward side of the high slope hill. As the separation induced wake develops downhill, it was found to expand and become weaker as the flow progresses further downstream (reduced wake effects). Therefore, the intensity of thrust fluctuations was found to decrease further downstream of the high slope hill. However, the opposite effect was observed for the low slope hill where flow separation did not occur. As the turbulence (due to the shadowing effect from the hill) develops downstream of the low slope hill (high turbulence region expands vertically, thereby affecting the dynamic loading of the wind turbine rotor), the intensity of trust load fluctuations was found to increase.
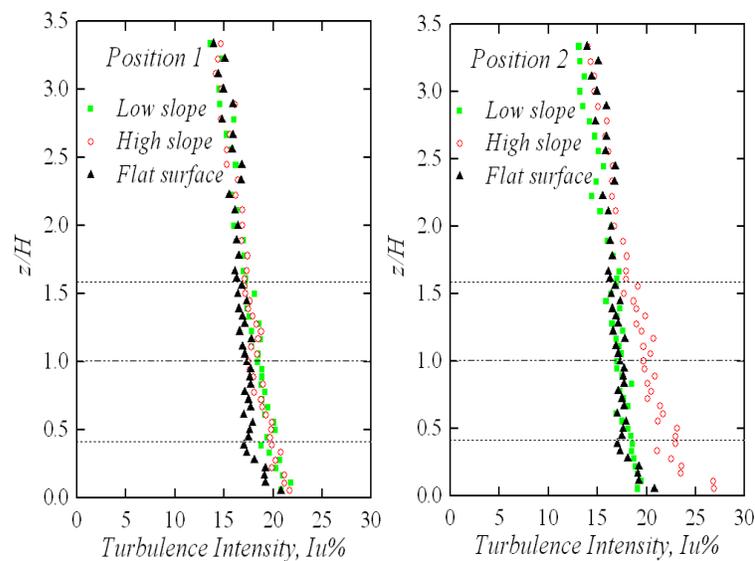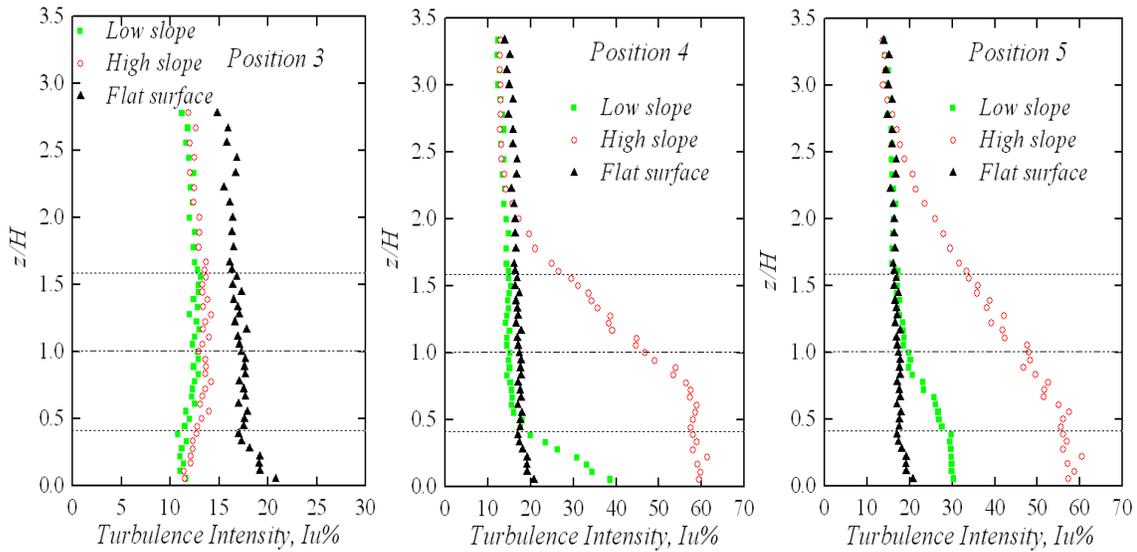
Figure 2-7 The mean flow turbulence intensity profiles over flat and complex terrains

Table 2-4 The dynamic wind loads on the model wind turbine over complex terrains

Wind turbine position	Position 1	Position 2	Position 3	Position 4	Position 5
Intensity of thrust fluctuation, σ_{C_T}/C_T *(Low slope hill)*	0.64	0.62	0.44	0.62	0.80
Intensity of thrust fluctuation, σ_{C_T}/C_T *(High slope hill)*	0.62	0.69	0.50	2.36	1.81

As a result, the flow characteristics in the wake of a hill were found to differ depending on the geometry of the hill, which could determine the severity of the flow separation and shadowing effects. The shadowing effect from the hill was found to dominate the flow behind the low slope hill, while separation due to adverse pressure gradient was found to be intense behind the high slope hill. It can be deduced from these results that wind turbines sited on the foot (blockage, pos2) or leeward side of the high slope hills (with flow separation, pos4 and pos5) are more likely to suffer from the fluctuating (dynamic) loads.

In addition to the speed-up effects, hilltops (pos3) were also found to experience much lower turbulence intensity levels in comparison to the baseline (flat) terrain. This is due to the fact that reduced wind shear on the hilltops will result in decreased turbulence intensity levels since wind shear contributes to the turbulence production in the flow. It is also another

beneficial outcome for the turbines sited on the hilltops. As a result, the intensity of the thrust load fluctuations was reduced significantly at the top of the hill, as shown in Table 2-4. Furthermore, the flow separation behind the high slope hill was also found to alter the flow turbulence character on the hilltop. As shown in Figure 2-7, the turbulence intensity levels at the top of the high slope hill were found to be slightly higher, also resulting in greater (14% more) intensity of thrust load fluctuations, compared to those at the top of the low slope hill. Therefore, the dynamic (fatigue) loads imposed on the wind turbines sited on the hilltops could drop dramatically; however, the flow separation behind the steep hills could have a negative impact on the dynamic loading of the wind turbines on the hilltops.

Wake interference of wind turbines sited over flat and hilly terrains:

A modern wind farm usually has multiple wind turbines arranged in an organized pattern or array. As the wind turbines in a wind farm interact with each other, it may have severe consequences on the downstream turbines located in the wake of upstream ones. The wake interference effects could cause greater power deficits along with the enhanced fatigue loads for the downstream turbines. However, majority of the previous experimental studies on the wake interference effects were conducted over simplified flat surfaces. The wake interference effects in non-flat terrain wind farms may be influenced by topography of the terrain, thus making these effects quite distinct for these types of environments.

The flat terrain wind farm layout of five turbines in tandem arrangement was studied as a baseline case, and the wake interference effects among wind turbines were investigated and compared to those in non-flat (hilly) terrain environments. Figure 2-8 gives the normalized velocity (with respect to the undisturbed incoming flow) and turbulence intensity profiles within the flat terrain wind farm. As shown in Figure 2-8(a), the maximum rate of reduction in the streamwise velocity (more pronounced below the hub height, $z/H<1.0$, due to the tower shadowing) was observed just after the first (upstream) turbine, and the velocity profile was found to reach equilibrium after the second turbine. Thus, the velocity profiles behind the second, third and fourth turbines were identical, which reveals the quick adjustment of the mean velocity inside the wind farm.

Furthermore, each turbine generates turbulent flow (shear generated) behind, and coexistence of multiple turbines in the wind farm with superimposed turbulent structures

(vortices) could increase the turbulence intensity levels (more pronounced above the hub height, $z/H > 1.0$), as shown in Figure 2-8(b), inside the wind farm. As the wake flow develops within the wind farm, the turbulence intensity profile was also found to stabilize after the second turbine. It is also important to note that ambient turbulence intensity levels and turbine size and spacing could significantly change the wake development inside a wind farm.
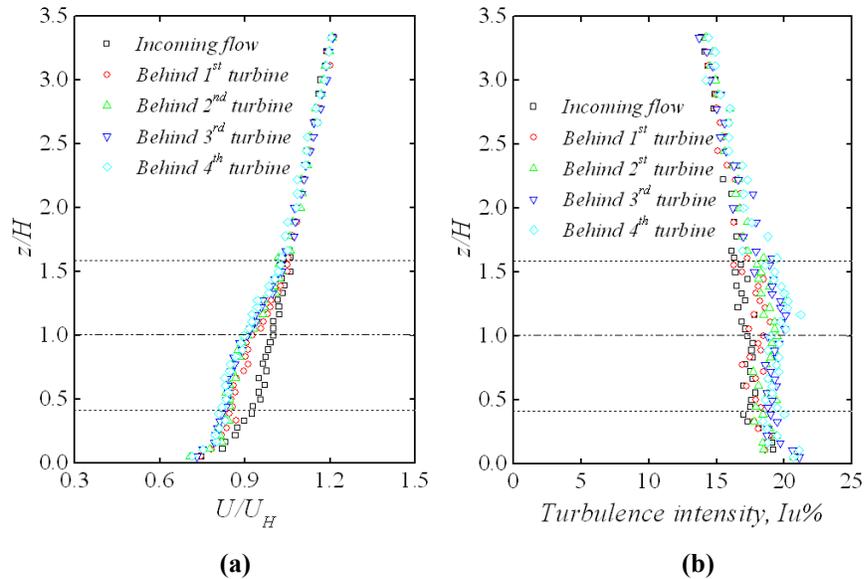
Figure 2-8 Flow characteristics in a flat terrain wind farm with wind turbines in tandem arrangement
(a) mean streamwise normalized velocity profile; (b) turbulence intensity profile
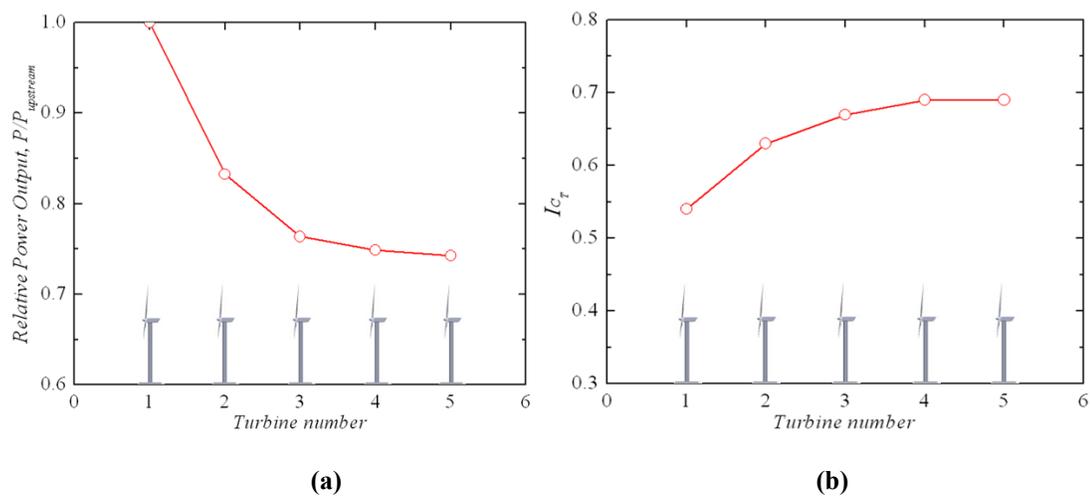
Figure 2-9 The performance and loading of wind turbines in a flat terrain wind farm
(a) relative power outputs; (b) intensity of thrust fluctuations

The power losses in a wind farm is primarily associated with the wake interference effects (velocity deficit). Therefore, the wind turbines located in the subsequent downstream rows of the wind farm could experience power deficits, as shown in Figure 2-9(a). The measured power output values were normalized with respect to the power output value of the upstream turbine. The significant power losses (17%) were observed for the wind turbine immediately after the upstream turbine. The drop rate in the power output was found to slow down after the second turbine and reach equilibrium at a power deficit of 26% in the last row. In addition, intensity of the thrust load fluctuations were correlated with the enhanced turbulence levels in the wind farm. It was shown in Figure 2-9(b) that fluctuating (dynamic) loads for the downstream turbines first increase and eventually level when equilibrium is reached. As a result, wake interference effects would not only degrade the power output performances of the wind turbines in the subsequent downstream rows of the wind farm but also reduce the fatigue lifetime of the wind turbine components.

The wake interference effects among multiple wind turbines sited at pre-selected positions along the low and high slope hills were correlated with the flow measurements, and the results were compared with those previously obtained for the simple (flat) terrain. In Figure 2-10 and Figure 2-11, the wake interference effects on the mean velocity profiles (with no-wake and in the wake scenarios) were given for each selected position along the hills. The measured mean flow velocity profiles in the wake were found to differ significantly depending on the topology of the terrain. Furthermore, the geometry of the hill (for the hilly terrains) was also found to be an important parameter affecting the wake flow statistics.

Hilly terrain environments show distinct topography due to the variable height along the hill, as compared to the flat terrain environments. As the hill height increases towards the top of the hill, wake effects were observed to mitigate due to the fact that successive wakes imposed by the upstream turbines could be partially blocked by the hill. In addition to that, speed-up effects would reduce the wake-induced velocity deficits. As shown in Figure 2-10 and Figure 2-11, wake-induced velocity deficits were found to become less significant at the top of the hill (pos3), and no significant velocity differences were observed between no-wake and wake situations for both low slope and high slope cases.
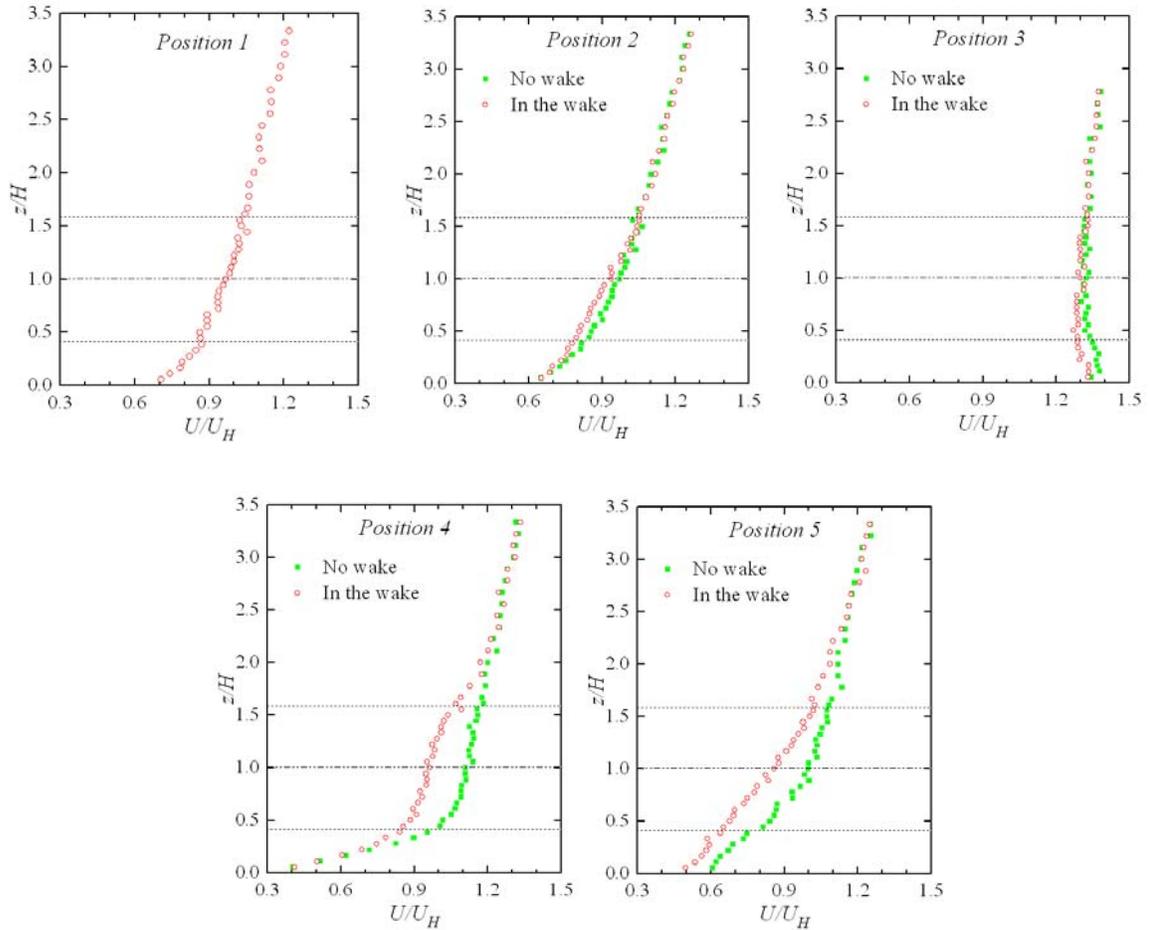
Figure 2-10 The comparison of mean streamwise normalized velocity profiles with and without wake interference effects at different positions of the low slope hill

Table 2-5 The wake interference effects on the power output performance of the wind turbines
Low slope hilly terrain vs. Flat terrain

Normalized power output		Position 1	Position 2	Position 3	Position 4	Position 5
Hilly terrain (Low slope)	No wake	0.92	0.93	1.82	1.28	0.94
	In the wake		0.82 (12% less)	1.69 (7% less)	1.02 (20% less)	0.73 (22% less)
Flat terrain		1.00	0.83 (17% less)	0.76 (24% less)	0.75 (25% less)	0.74 (26% less)
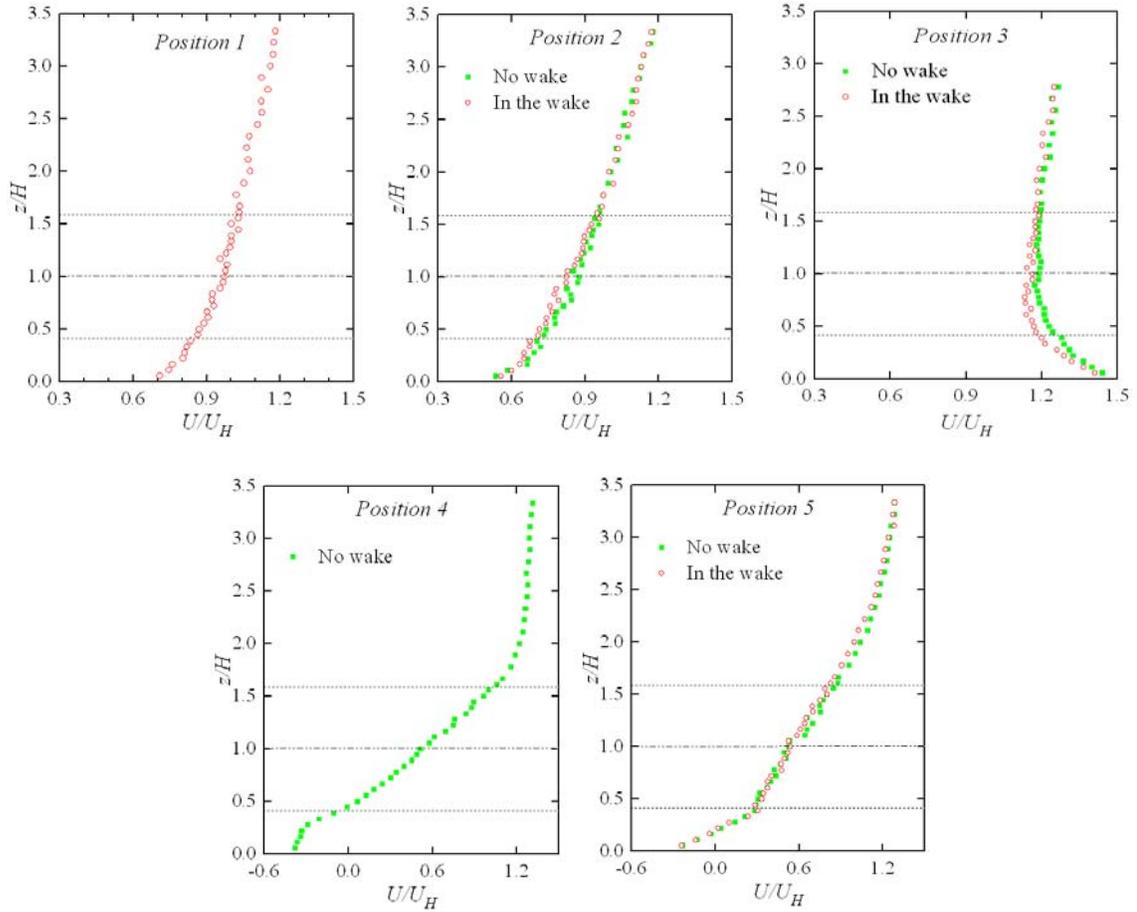
Figure 2-11 The comparison of mean streamwise normalized velocity profiles with and without wake interference effects at different positions of the high slope hill

Table 2-6 The wake interference effects on the power output performance of the wind turbines
High slope hilly terrain vs. Flat terrain

Normalized power output		Position 1	Position 2	Position 3	Position 4	Position 5
Hilly terrain (High slope)	No wake	0.92	0.79	1.45	0.04	0.20
	In the wake		0.63 (20% less)	1.33 (8% less)	0.04 (0% less)	0.19 (5% less)
Flat terrain		1.00	0.83 (17% less)	0.76 (24% less)	0.75 (25% less)	0.74 (26% less)

Hill geometry was found to play a central role in the wake interference effects behind the top of the hill. As shown in Figure 2-10, wake interference effects in the low slope hill case were more pronounced for the downstream turbines located behind the hill (pos4 and pos5) along with the wake growth up to z/H > 2.0 in the vertical direction. However, as shown in Figure 2-11, the flow separation was found to outweigh the wake interference effects behind the high slope hill, thus causing almost no difference in the wake flow velocity profile.

The power deficits (due to the wake interference effects) observed at each turbine sited along the low and high slope hills were quantitatively shown in Table 2-5 and Table 2-6, and compared to those in a flat terrain. The results highlight the fact that the wind turbines at the top of the hill (pos3) could experience reduced power deficits (7% - 8%) due to the wake induced velocity deficits, which is significantly lower than that of the wind turbine (located at pos3) with a power deficit of 24% in a flat terrain. The wake interference effects behind the top of the hill (pos4 and pos5) were found to be strongly dependent on the geometry of the hill (i.e., the slope), and these effects could cause power deficits up to 22% for the downstream turbine located behind the low slope hill (pos5). However, the power deficits for the downstream turbine (located at the same position, pos5) in a simple (flat) terrain would still be greater (26%). Furthermore, the flow separation behind the high slope hill (pos4 and pos5) was found to significantly degrade the performance of the wind turbines, implying that the wake interference effects would be almost negligible behind the high slope hill.

Table 2-7 The wind farm performance comparison in flat and complex (hilly) terrain environments

Normalized Power	Position 1	Position 2	Position 3	Position 4	Position 5	Total
Hilly terrain wind farm (Low slope)	0.92	0.82	1.69	1.02	0.73	5.18 (27% more)
Hilly terrain wind farm (High slope)	0.92	0.63	1.33	0.04	0.19	3.11 (24% less)
Flat terrain wind farm	1.00	0.83	0.76	0.75	0.74	4.08

In Table 2-7, the total power output from the wind turbine array, having five turbines in tandem arrangement, was calculated in simple (flat) and hilly (low slope and high slope) terrain environments. In flat terrain, the total power output of the wind turbine array was found to be 4.08 times as much as the upstream turbine power output (it should be 5.00 without any wake interference effects, thereby indicating a total power deficit of around 18% for the wind turbine

array). However, the wind turbine array sited along the low slope hill could generate 27% more power than the one sited in a flat terrain. The total power output of the wind turbine array along the low slope hill was calculated to be 5.18 times as much as the upstream turbine power output (it is greater than 5.00, implying the fact that speed-up effects outweigh the wake interference effects). Moreover, flow separation effects would become more important for the high slope hill (outweighing the speed-up and wake interference effects behind the hill), therefore the total power output from the wind turbine array was found to be 3.11 times as much as the upstream turbine power output, which is 24% less than the one in a flat terrain. As a result, the hilly terrains with the low/gentle slope could be considered as a wind farm site with great wind energy potential.

The wake interference effects (enhanced turbulence) could also increase the dynamic loading on the wind turbine components. The intensity of thrust fluctuations was given in Table 2-8 to illustrate the effect of the wake-induced turbulence on the turbine dynamic loading in hilly terrain wind farms. As shown in Table 2-8, the intensity of thrust fluctuations was found to significantly reduce at the top of the hill regardless of the hill geometry, indicating no sign of wake interference effects (due to the terrain topology). However, wake-induced turbulence was found to become more evident behind the low slope hill, thus causing greater intensity of thrust fluctuations for the downstream turbines (pos4 and pos5). On the contrary, the wake influence was found to be almost negligible behind the high slope hill due to the topological effects (enhanced turbulence due to flow separation). Therefore, wind turbines sited behind the high slope hills could encounter highly turbulent flow regimes, enhancing the dynamic loads on the wind turbine components. It should also be noted that the intensity of thrust fluctuations for the downstream turbines (pos4 and pos5) sited in flat terrain was found to be smaller than those sited in hilly terrains. As a result, the fatigue lifetime of the wind turbine components, associated with the dynamic loads, should be seriously considered in the mechanical design of the wind turbines to be sited in hilly terrain environments.

Table 2-8 The wake interference effects on the turbine dynamic wind loads in a wind farm
High slope hilly terrain vs. Low slope hilly terrain

Wind turbine position		Position 1	Position 2	Position 3	Position 4	Position 5
Intensity of thrust fluctuations, σ_{C_T}/C_T (Low slope hill)	No wake	0.64	0.62	0.44	0.62	0.80
	In the wake		0.65	0.46	0.77	0.92
Intensity of thrust fluctuations, σ_{C_T}/C_T (High slope hill)	No wake	0.62	0.69	0.50	2.36	1.81
	In the wake		0.71	0.54	2.79	1.88

2.4 Conclusion

An experimental study was conducted to characterize the performance of onshore wind farms sited in flat and hilly (low and high slope) terrain environments under atmospheric boundary layer conditions. The detailed flow field measurements were related with the wind load and power output measurements so as to investigate the effect of the terrain topology on the oncoming flow character and wind turbine/array performance.

The accumulated pressure on the foot of the hills was found to significantly affect the flow statistics (mean velocity and turbulence intensity), causing power deficits and enhanced dynamic loads on the turbines (pos2). These effects were more pronounced on the foot of the high slope hill. As the flow reaches the top of the hill, the mean flow velocity was significantly enhanced (due to the speed-up effect), and turbulence intensity levels were reduced. Therefore, the wind turbines on the top of the hill (pos3) could generate more power under relatively lower turbulent flow conditions (reduced dynamic loads). However, the flow separation behind the high slope hill was found to not only affect the flow field on the leeward slope but also on the top of the hill, causing reduced speed-up effects on the top of the high slope hill, as compared to the low slope hill. The separated flow could be characterized with higher velocity deficits and enhanced turbulence levels, thus wind turbines behind the high slope hill (pos4 and pos5) were found to suffer in terms of the power production performance and dynamic loads. In case of a low slope hill with no flow separation, speed-up effects were observed to diminish gradually behind the hill, and shadowing effect from the hill was also found to affect the flow field towards the foot of the leeward slope (pos5).

The topology of the terrain was found to significantly affect the wind turbine/array performance. The performance of a wind farm sited along the hilly terrain could be quite different than the wind farm performance in flat terrain. In addition, the hill geometry was found to play a central role in the wind turbine/array performances and wake interactions. The results indicate that wind farm sited along the low slope hill could generate more power in comparison to the wind farm in flat terrain. However, the wind turbine/array performance along the high slope hill could be significantly lower due to the flow separation observed behind the hill. Furthermore, the flow separation effects were found to outweigh the wake interference effects behind the high slope hill. Along with the wind turbine/array performance, the dynamic loads were also quantified by calculating the intensity of thrust fluctuations. The dynamic wind loads on the downstream turbines (pos4 and pos5) were found to be higher in hilly terrains than those in a flat terrain. The dynamic loads on the downstream wind turbines was primarily due to the wake interference effects behind the low slope hill; however, it was mainly due to the flow separation behind the high slope hill. These fluctuating (fatigue) loads are of great importance for the (fatigue) lifetime of the wind turbine components.

CHAPTER 3. THE EFFECTS OF THE ONCOMING (AMBIENT) FLOW CONDITIONS ON THE WAKE CHARACTERISTICS AND DYNAMIC WIND LOADS ACTING ON A WIND TURBINE MODEL

3.1 Introduction

Today, with the rapid development of the wind energy, wind turbines sited in wind farms would operate under many different terrain conditions, ranging from rather flat terrains such as open sea/ocean for offshore wind farms to much rougher complex terrains for onshore wind farms. However, significant differences exist in the characteristics of the atmospheric boundary layer winds over typical offshore and onshore wind farms. While the near-neutral boundary layer winds over the offshore terrains are found to have relatively shallow boundary layers with relatively low ambient turbulence levels, significant variations are found on the onshore wind characteristics (i.e., wind shear and ambient turbulence) due to the sharp changes in the surface friction (i.e., roughness) and atmospheric stability. Therefore, wind turbines could experience quite different surface wind characteristics depending on the terrain of the site.

A number of studies were conducted to reveal the effects of the ambient turbulence levels on the performance of the wind turbines as well as the wake characteristics behind the turbines. Sheinman and Rosen (1992) indicated that the over-prediction of the turbine power output could be more than 10% when the effects of the ambient turbulence levels were ignored. Furthermore, Chamorro and Porte-Agel (2009) showed that the wake effects (i.e., the velocity deficit and added turbulence intensity) could be still noticeable at a downstream distance of fifteen rotor diameters. Moreover, Ozbay et al. (2012) studied the ambient turbulence effects on the different wind farm layout performances, and they found that higher ambient turbulence levels, corresponding the onshore wind farm case, could improve the wind farm efficiency by up to 6% depending on the wind farm configuration.

The wind turbine wakes are typically divided into near and far wake regions (Vermeer et al., 2003). In the near wake, the rotor characteristics such as the number of the blades, blade rotation and aerodynamics significantly affect the flow, leading to a three dimensional flow with highly turbulent, unsteady flow structures. The evolution of the unsteady vortex and turbulent structures in the near wake were investigated under different atmospheric boundary

layer winds. Whale et al. (2000), Grant and Parkin (2000) and Massouh and Dobrev (2007) conducted experimental investigations on the near wake flow structures behind the model wind turbines in airflows or water flows with uniform flow velocity; however, Chamorro et al. (2011), Hu et al. (2012), Yang et al. (2012) and Zhang et al. (2012) also performed similar studies in nonhomogeneous atmospheric boundary layer flows with stronger vertical velocity gradients and higher ambient turbulence levels. Based on the results from these previous studies, the turbine wake characteristics were found to substantially differ depending on the oncoming flow conditions (i.e., wind profile and ambient turbulence).

Furthermore, Hu et al. (2012), Chamorro et al. (2011) and Lebron et al. (2009) investigated the evolution of the unsteady vortex structures in the turbine wake and/or quantified the dynamic loads acting on the model wind turbines in atmospheric boundary layer winds. Massouh and Dobrev (2007) reported that the unsteady wake vortices could be one of the main sources behind the blade vibration, thereby leading to higher dynamic loads on the wind turbine blades. Schreck and Robinson (2005) highlighted the effects of vortex initiation and convection on the dynamic stall of the wind turbine blades. Robinson et al. (1999) characterized the impact of the wake flow characteristics (i.e., three-dimensionality, unsteadiness, and flow separation) on the downstream wind turbines. In addition, several numerical models have been proposed in order to predict the dynamic responses of the wind turbines. Moriarty et al. (2004) coupled a stochastic turbulence simulator with an aeroelastic code, and generated multiple samples of wind loading data under various wind conditions. More recently, Lee et al. (2011) investigated the atmosheric and wake turbulence impacts on the wind turbine through a two-way coupled aeroelastic tool with large eddy simulation (LES).

The present experimental study investigates the effects of the oncoming (ambient) flow conditions on the turbine wake characteristics and wind loads acting on a model wind turbine. The experiments were carried out in a large-scale atmospheric/aerodynamic boundary layer wind tunnel under different atmospheric boundary layer wind conditions with different wind profiles and turbulence characteristics. Therefore, a model wind turbine was sited in two different environments, corresponding to typical offshore and onshore environments (i.e., the offshore and onshore case), simulated in the wind tunnel. Along with

the wind load measurements, detailed flow field measurements were conducted in the turbine wake by using a high resolution Particle Image Velocimetry (PIV) and Cobra Probe Anemometry system. In this investigation, the evolution of the unsteady vortex and turbulent structures in the wake were quantified and correlated with the dynamic loads in typical offshore and onshore boundary layer winds.

3.2 Experimental Set-up and Procedure

The experimental study was performed in the Aerodynamic/Atmospheric Boundary Layer (AABL) Wind Tunnel located at the Aerospace Engineering Department of Iowa State University. Figure 3-1 shows the test section of the AABL wind tunnel with triangular spires at the beginning of the test section and array of wooden blocks on the floor to simulate the flow conditions similar to those observed in typical offshore and onshore boundary layer winds. Thus, the aspect ratio of the isosceles triangle shaped spire structures at the beginning of the test section as well as the height and spacing of the roughness elements on the floor were adjusted similar to the work reported by Irwin (1981), Sill (1988) and Jia et al. (1998). The tunnel ceiling was also adjusted along the length of the test section so as to ensure zero pressure gradient along the flow direction.

Figure 3-1 AABL wind tunnel used for the present study

The mean velocity profile of an atmospheric boundary layer wind over an open terrain can be fitted well with the power law (Zhou and Kareem, 2002; Jain, 2007). Different power law

exponents represent different types of terrain with different wind characteristics. Figure 3-2 gives the measured mean flow velocity and turbulence intensity profiles of the offshore and onshore cases simulated in the wind tunnel. The measurement data given in Figure 3-2 were obtained from the Cobra Probe measurements at the location where the model wind turbine would be placed. As shown in Figure 3-2(a), the power exponent for the first type of ABL wind was found to be about 0.11, which was reported as a good approximation for offshore applications under near-neutral stability conditions (Hsu et al., 1994). The corresponding turbulence intensity (i.e., 9.5%) at the hub height is also in agreement with the site measurements of Hansen (2012) at Horns Rev offshore wind farm. Moreover, the power exponent of $\alpha = 0.16$ obtained for the second type of ABL wind, as shown in Figure 3-2(b), could represent the onshore boundary layer wind over open country terrain with low scrub or scattered trees based on ASCE standard (Zhou, 2002). The turbulence intensity profile for the onshore case was also found in fairly good agreement with the AIJ standard values as suggested by Architectural Institute of Japan (AIJ, 1996). It should be also noted that, the ambient turbulence levels at the turbine hub height for the onshore case (i.e., Type 2 ABL wind) was about 18%, corresponding to almost twice as much of that observed for the offshore case (i.e., Type 1 ABL wind).

Figure 3-3 shows a schematic of the three-bladed horizontal axis wind turbine model along with typical cross section profiles of the turbine rotor blades. The model turbine has a rotor radius of 140 mm and hub height of 226 mm (see Table 3-1 for detailed design parameters). With the scale ratio of 1:320, the test model would represent a commercial wind turbine in a wind farm with a rotor diameter about 90 m and a tower height about 80 m. The ratio of the blade swept area to the cross-section area in the wind tunnel was found to be less than 1.5%. Thus, blockage effects for this study would be very small, and could be neglected. Furthermore, the wind turbine rotor blades are made of a hard plastic material by using a rapid prototyping machine. The blade sections were generated by mathematically applying a spline in tension to interpolate between the defined input stations based on the ERS-100 wind turbine blade prototype developed by TPI Composites. A constant circular cross section from the root of the blade to a distance of 5% radius of blade (R) and three NREL airfoils (S819, S820, S821) placed at various locations as inputs were used to generate the blade profile. The S821 root

airfoil was used between 0.208R and 0.40R, the S819 primary airfoil was positioned at 0.70R, and the S820 tip airfoil was specified at 0.95R. Further information about the ERS-100 rotor blades is available at Locke et al. (2003).

In the present study, the rotor blades were mounted on a turbine hub with a pitch angle of 3.0 degrees (i.e., θ=3.0 deg.), and a DC electricity generator was installed in the nacelle of the model wind turbine, which would produce electricity as driven by the rotating blades. During the experiments, the mean wind speed at the hub height of the model wind turbine was set to be about 5 m/s (i.e., U_{hub}=5 m/s). The Reynolds number based on the averaged chord length of the rotor blades (c) and the oncoming wind speed at the hub height (U_{hub}) was found to be about 7000 (i.e., $Re_c \approx 7000$). However, it is significantly lower than those of the large-scale wind turbines in the field, i.e., $Re_c > 1.0*10^6$ for the large-scale wind turbines as reported by Wilson (1994). According to Alfredsson et al. (1982) and Medici et al. (2006), the chord Reynolds number may have a significant effect on the power production performance of the wind turbine (i.e., the maximum power coefficient would be much lower for a small-scale model turbine operating at a lower chord Reynolds number); however, the evolution of the unsteady vortices in the turbine wake would become almost independent of the chord Reynolds number when the chord Reynolds number reach a sufficiently high value. De Vries (1983) suggested a required minimum chord Reynolds number range on the order of $Re_c = 3*10^5$ for a reliable comparison of the experimental results with the field data. Recently, Chamorro et al. (2011) conducted a comprehensive experimental study to quantify the Reynolds number dependence of the wake turbulence statistics under atmospheric boundary layer winds. Instead of using the chord Reynolds number, they defined the Reynolds number based on the turbine rotor diameter (D) and the flow velocity at the turbine hub height (U_{hub}). They found that the fundamental flow statistics (i.e., normalized mean velocity profile, turbulence intensity, kinematic shear stress and velocity skewness) in the turbine wake have asymptotic behavior with the Reynolds number. The mean velocity profile in the wake was found to reach the Reynolds number independence at a lower value in comparison to the higher order statistics such as turbulence intensity, turbulence kinetic energy, and Reynolds shear stress. Therefore, Reynolds number independence for the mean velocity could be reached at $Re_c \approx 4.8*10^4$, and for the higher order statistics, this value is at around $Re_c \approx 9.3*10^4$. It should be noted that, the

Reynolds number based on the rotor diameter and the hub height wind speed for the present study is about $9*10^4$ so that the turbine wake statistics would be independent of the Reynolds number, as suggested by Chamorro et al. (2011).

In the present study, the rotational speed of the turbine rotor blades were adjusted by applying different electric loads to the small DC generator installed inside the nacelle. The turbine rotational speed $\acute{\Omega}$ could vary from 0 to 2200 rpm, the corresponding tip speed ratio ($\lambda = \acute{\Omega}R/U_{hub}$) range was between $0 - 6.5$. During the experiments, the model wind turbine was set to operate at a tip speed ratio of $\lambda \approx 5.0$, which falls within the operating tip speed ratio range ($\lambda \approx 4.0 - 8.0$) of wind turbines in the field (Burton et al., 2001).

Furthermore, an aluminum rod was used as the turbine tower, and it was connected to a high-sensitivity force-moment sensor (JR3 load cell) through a hole on the wind tunnel floor. The JR3 load cell is composed of foil strain gage bridges, which are capable of measuring forces and moments on three orthogonal axes. The accuracy of the JR3 load cell measurements is 0.25% of the full range (40 N). The wind load data were acquired for 120 seconds at a sampling rate of 1kHz for each measurement. A Monarch Instrument Tachometer was also used to measure the rotational speed of the turbine rotor blades independently.

In addition to the wind load measurements, a high-resolution Particle Image Velocimetry (PIV) system was used to conduct detailed flow field measurements in the streamwise-vertical plane of the turbine wake. Figure 3-4 gives the schematic of the experimental set-up used for the planar PIV measurements. For these measurements, the airflow was seeded with 1μm oil droplets by using a smoke generator. Illumination was provided by a double-pulsed Nd:YAG laser, emitting two pulses of 200 mJ at the wavelength of 532nm. The thickness of the laser sheet in the measurement region was about 1.0 mm. Two high-resolution 12-bit CCD cameras were used for PIV image acquisition with the axes of the cameras perpendicular to the laser sheet in order to have a larger measurement window along the streamwise direction. The CCD cameras and the double-pulsed Nd:YAG laser were connected to a workstation (host computer) via a digital delay generator, which was used to control the timing of the laser illumination and the image acquisition.
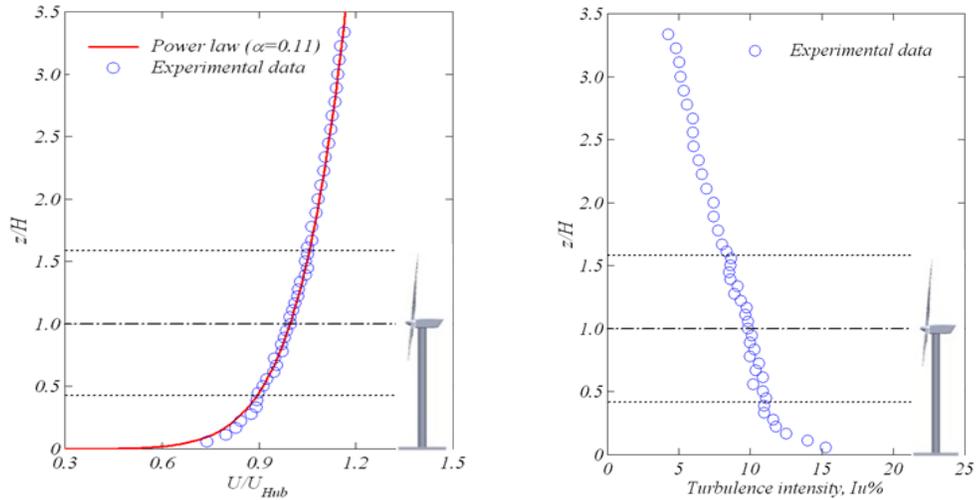
(a) Type-1 incoming ABL wind (i.e. the offshore case)
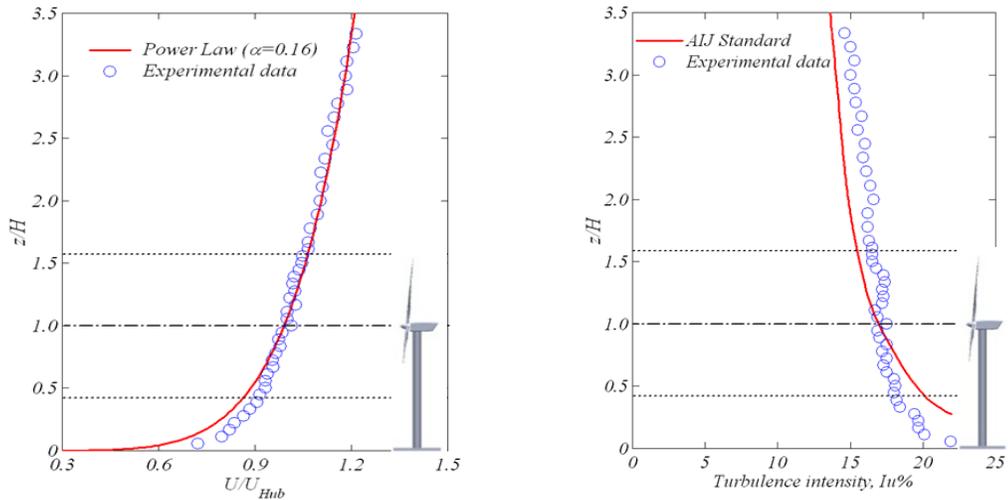
(b) Type-2 incoming ABL wind (i.e. the onshore case)

Figure 3-2 Flow characteristics of the two different incoming ABL winds
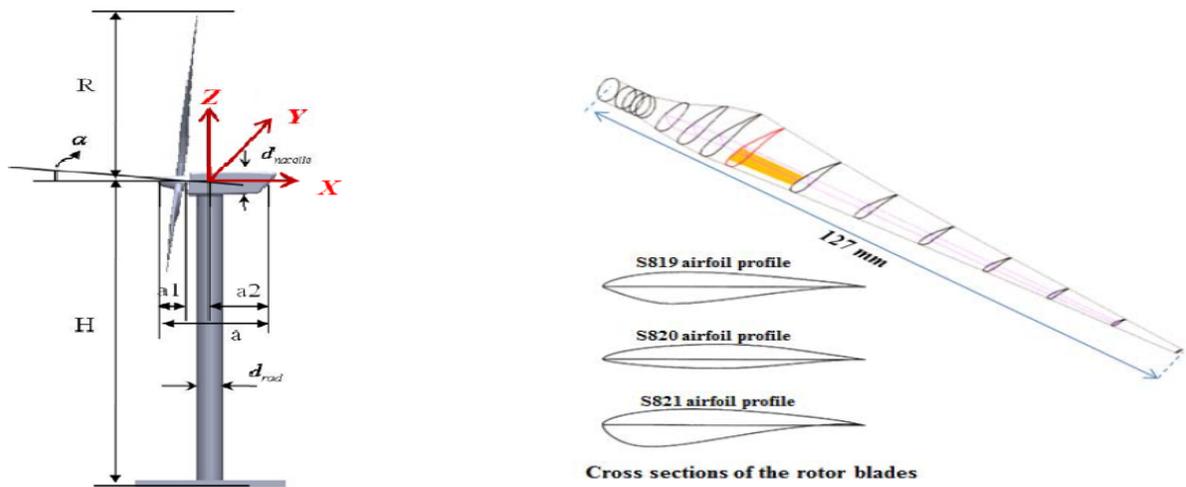
Figure 3-3 The schematic of the wind turbine model

Table 3-1 The design parameters of the wind turbine model

Parameter	R	H_{hub}	d_{rod}	$d_{nacelle}$	γ	a	a_1	a_2
Dimension (mm)	140	226	18	26	5°	68	20	35
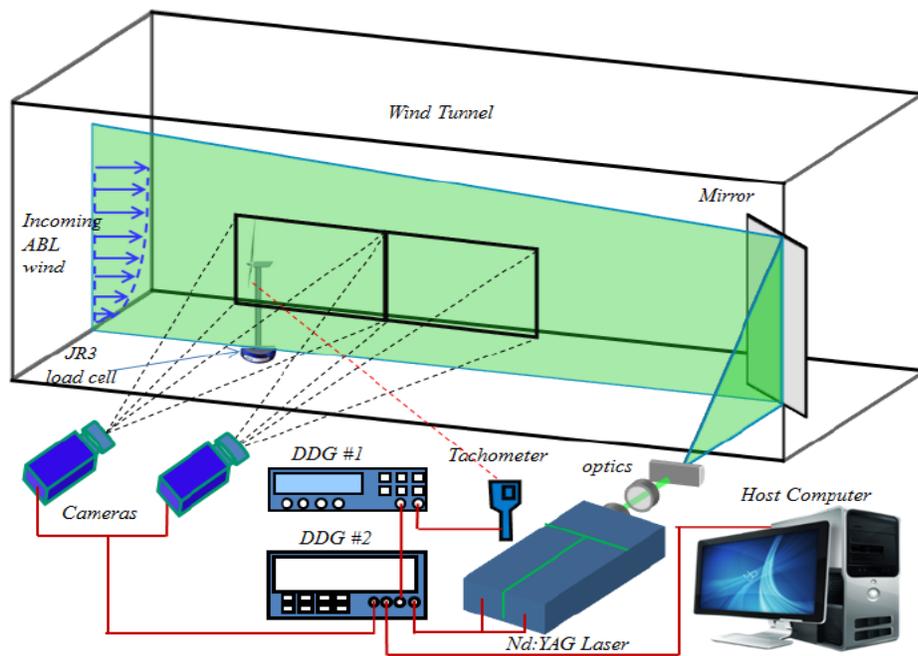
Figure 3-4 The experimental set-up for PIV measurements in the wake

After PIV image acquisition, instantaneous velocity vectors were obtained by a frame to frame cross-correlation technique in interrogation windows of 32*32 pixels with an effective 50% overlap of the interrogation windows. The instantaneous velocity vectors (i.e., streamwise (u) and vertical (v) velocity components) were then determined by the simple equation: speed=distance/time, where distance is the displacement of the seeding particle and time is the time delay between the two image frames. The time delay was adjusted via a digital delay generator, and it was in the order of μs (micro-seconds). Then, the ensemble averaged flow quantities such as normalized velocity (U/U_{hub}), normalized Reynolds stress (R_{uv}/U^2_{hub}), where $R_{uv} = - u'v'$, and normalized Turbulence Kinetic Energy (TKE/U^2_{hub}), where $TKE=0.5(u'^2+v'^2)$, were obtained from approximately 1000 frames of instantaneous PIV measurements. The measurement uncertainty level for the velocity vectors was estimated to be within 2%, and it was about 5% for the second-order flow quantities (i.e., Reynolds stress and turbulence kinetic energy).

In the present study, both free-run and phase-locked PIV measurements were performed in the turbine wake. The free-run measurements were carried out to determine the previously mentioned ensemble averaged flow quantities. The image acquisition rate was pre-selected at a frequency (i.e., typically at a slower rate to make sure the flow fields are not correlated in time) different than the rotational frequency of the turbine rotor blades so as to ensure the physical meaning of the ensemble averaged flow quantities. However, phase-locked measurements were conducted to elucidate more details about the evolution of unsteady wake vortices with respect to the position of the rotor blades. For phase-locked measurements, a digital tachometer was used to detect the position of a pre-marked blade so that tachometer generated pulsed signal was used to trigger the PIV system via a digital delay generator. Therefore, different rotation phase angles of pre-marked rotor blade can be achieved by changing the time delay between the input signal from the tachometer and the signal output from the digital delay generator. For each pre-selected phase angle, 200 frames of instantaneous PIV measurements were used to obtain the phase-averaged velocity and vorticity distributions in the wake flow behind the model turbine.

3.3 Results and Discussions

a) *Wind loads acting on different components of a wind turbine model:*

The wind loads (mean and dynamic) acting on the wind turbine model were measured via a high-sensitivity force transducer (JR3, model 30E12A-I40) with a full scale of 40N and ±0.25% accuracy. It was attached underneath of the tested wind turbine model, and it can provide time-resolved measurements of all three components of the forces and moments acting on the model. In this study, only the thrust coefficient (i.e. the force coefficient along X-axis in the Cartesian coordinate system shown in Figure 3-3) and the bending moment coefficient (i.e. the moment coefficient about Y-axis in the Cartesian coordinate system shown in Figure 3-3) were considered for the analysis, and calculated by using the expressions of $C_T = T / (0.5\rho U_{Hub}^2 \pi R^2)$ and $CM_y = M_y / (0.5\rho U_{Hub}^2 \pi R^2 H)$ respectively, where ρ is the air density, R is the radius of the wind turbine rotor and H is the hub height of the wind turbine. For each tested case, the wind loads data were acquired for 120 seconds at a sampling rate of 1000Hz.

Figure 3-5 shows the contributions of different wind turbine components (i.e. tower, nacelle, stationary and rotating rotor) on the turbine loading. As shown in Figure 3-5(a), the mean thrust (axial) and moment (bending) loads acting on both tower and nacelle together contribute about 10% of the overall wind loads on the turbine operating at the optimum tip speed ratio. As the wind speed increases exponentially with the height in the atmospheric boundary layer, the region corresponding to the rotor of the turbine could experience much higher wind speeds thereby resulting in higher values of the mean wind loads on the turbine. Furthermore, around 60% of the mean wind loads on the turbine were found to occur due to greater aerodynamic forces induced by the rotation. Although the mean wind loads acting on the stationary turbine were observed to constitute 40% of the overall mean wind loads, it would not be the case for a commercial-scale turbine. This is due to the fact that modern commercial-scale wind turbines are pitch controlled and could pitch the blades out of the oncoming wind (or feather the blades) so as to reduce the effect of the aerodynamic forces in the event of shut-down or curtailment when turbines do not operate. Thus, feathering the blades could be crucial for the structural integrity of the rotor at extreme wind conditions (i.e. wind speed exceeds the wind turbine cut-out speed).

Although the mean wind loads are of great importance for the mechanical design of the turbines, the fluctuating (dynamic) loads should also be taken into account since the components of the wind turbines (i.e. rotor blades, drive train) could be susceptible to fatigue failures under these unsteady loads. In the present study, the standard deviations of the measured wind loads were used as a measure of the dynamic loads on the turbine. As shown in Figure 3-5(b), the dynamic loads acting on both tower and nacelle together were found to contribute less than 10% of the overall dynamic wind loads on an operational wind turbine, and around 80% of the fluctuating loads were found to occur due to rotation. This suggests that the effects of rotation could be more intense on the dynamic wind loads in comparison to its effects on the mean wind loads. However, it should be noted that the mean and dynamic wind loads could be much less for a stationary rotor with feathered blades. Therefore, these quantitative results highlight the significance of the rotational effects on the wind turbine loading.
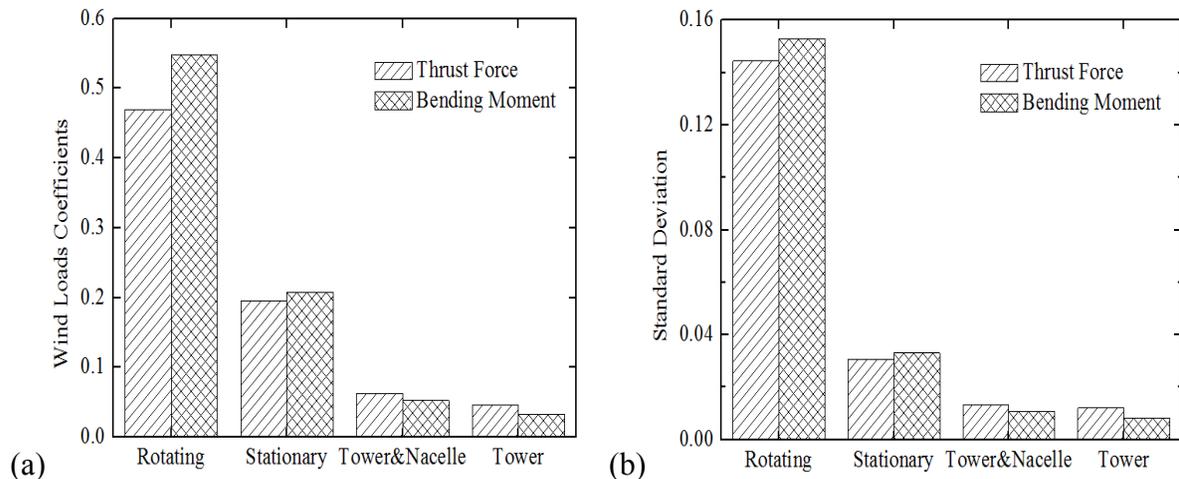
Figure 3-5 The comparison of the mean and dynamic (fluctuating) loads acting on different components of the wind turbine model   (a) mean wind loads; (b) dynamic wind loads

b) Thrust loads acting on a wind turbine sited in different boundary layer winds:

Figure 3-6 shows the measurement results based on the analysis of the instantaneous thrust (axial) loads acting on the model wind turbine sited in two different types of atmospheric boundary layer winds, corresponding to the scenario of having the same turbine in typical offshore and onshore boundary layer wind conditions. The time history of the instantaneous thrust loads acting on the model wind turbine, as shown in Figure 3-6(a), was
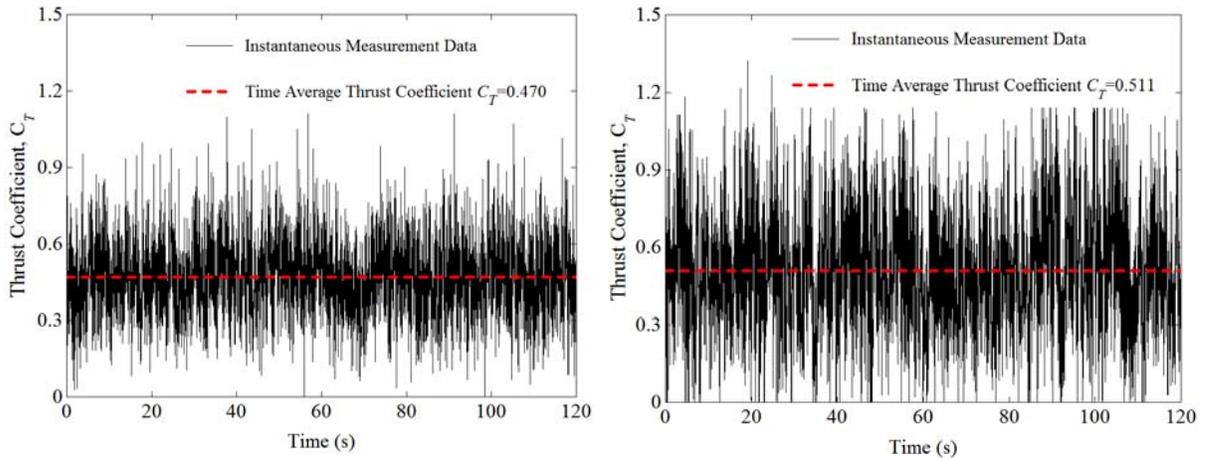
(a)
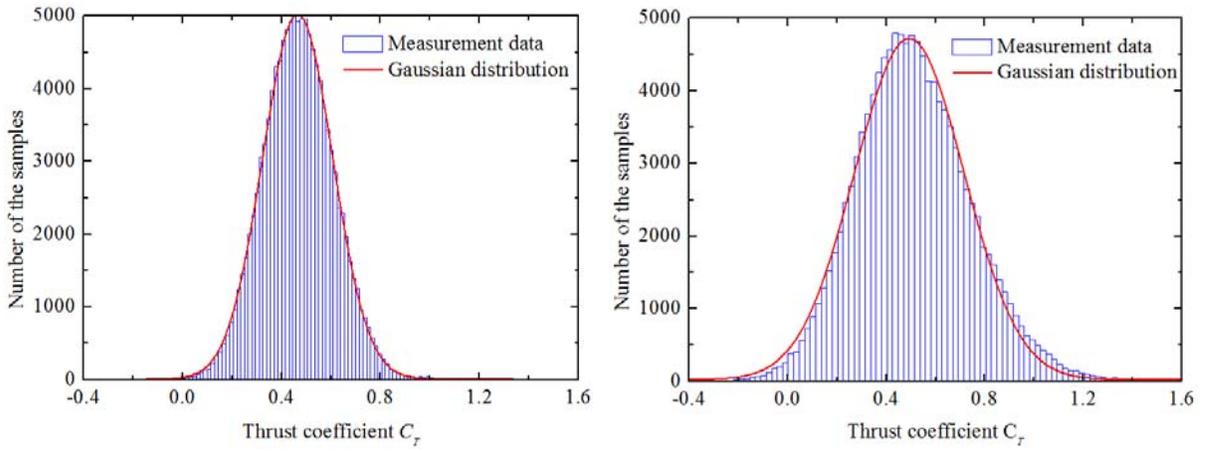
(b)
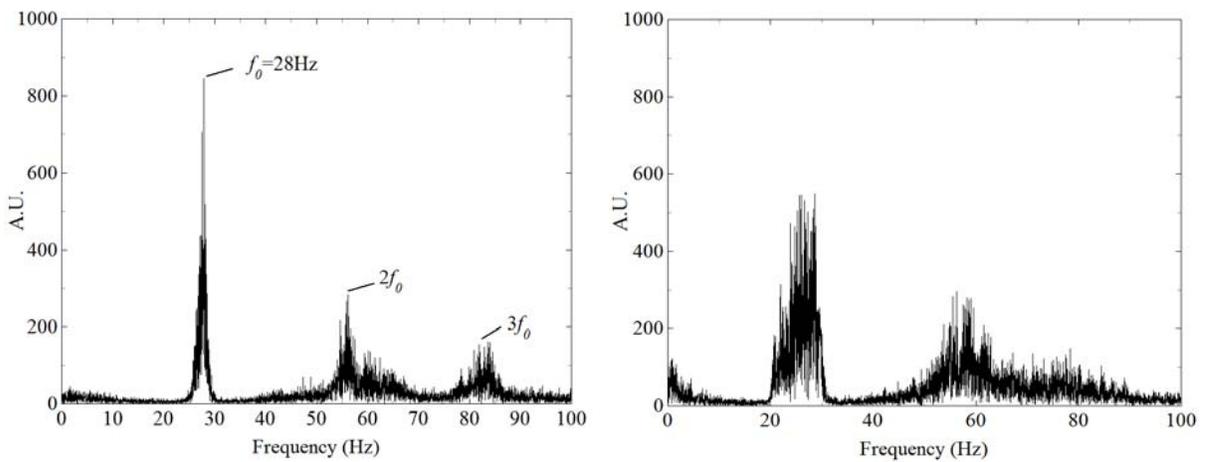
(c)

Figure 3-6 The measurement results of the thrust (axial) loads acting on the model wind turbine for offshore (left) and onshore (right) cases (a) time history; (b) histogram; (c) power spectrum

found to show highly unsteady behaviour under turbulent atmospheric boundary layer wind conditions (i.e., for both the offshore and onshore cases). The dashed lines in the plots were used to represent the time-averaged (mean) values. Thus, the instantaneous thrust loads acting on the turbine were observed to fluctuate significantly about the mean values, and the amplitude of these fluctuations were found to be much higher for the onshore case, in comparison with those of the offshore case. This could be associated with the significant difference in the turbulence intensity levels of the offshore and onshore boundary layer winds. Furthermore, the mean value of the thrust load acting on the turbine for the onshore case (i.e., C_T=0.511) was found to be slightly higher than that of the offshore case (i.e., C_T=0.470).

Figure 3-6(b) shows the histograms of the measured instantaneous thrust loads acting on the model turbine, and they were fitted reasonably well with the Gaussian curves. However, the shapes of the Gaussian curves (i.e., the width) were found to differ for the offshore and onshore cases. The width of the Gaussian curve was found be larger for the onshore case, thereby indicating greater deviation from the mean value. Thus, the standard deviation value of the instantaneous thrust coefficient for the onshore case was found to be about 0.23 (i.e., σ=0.23), which is 1.7 times higher than that of the offshore case (i.e., σ=0.14). The standard deviation value of the unsteady wind loads could be used as a quantitative parameter to evaluate the dynamic (fatigue) loads on the wind turbine components, and it is believed to be strongly dependent on the turbulence intensity levels of the oncoming atmospheric boundary layer wind. Therefore, dynamic loads on the onshore wind turbine components would be much severe considering the high ambient turbulence levels in the atmospheric boundary layer wind. As wind turbines operate in different atmospheric boundary layer wind conditions, such quantitative measurement results shed light on the importance of the ambient turbulence effects for the turbine loading.

Figure 3-6(c) gives the power spectra of the measured instantaneous thrust loads acting on the model turbine through a fast Fourier transform (FFT) analysis procedure. A well-defined dominant peak at f_0=28 Hz, corresponding to the rotational speed of the turbine rotor blades at the optimum tip speed ratio, could be identified for the turbine operating in the offshore boundary layer wind. Furthermore, other frequency peaks, representing the peaks at harmonic

multiples (i.e., $2f_0$, $3f_0$) of the turbine blade rotational frequency f_0, were also observed in the spectrum plot. However, the rotational speed of the turbine rotor blades was found to fluctuate in a wider frequency region (i.e., 23 Hz < f_0 < 30 Hz) for the onshore case so that no well-defined dominant and harmonic peaks could be seen in the corresponding power spectrum. Thus, these fluctuations, associated with the higher ambient turbulence intensity levels, in the rotational speed of the turbine rotor blades would impose greater dynamic (unsteady) loads on the wind turbine components. Moreover, it would cause disturbances on the tip and root vortices shedding from the turbine rotor blades, which were observed in the phase-locked PIV measurements to be discussed later.

c) Free-run PIV measurements results:

The free-run PIV measurements were conducted in the near-wake (X/D<2.5) of the model wind turbine in order to determine the ensemble-averaged wake flow statistics (i.e., mean flow velocity, turbulence kinetic energy and Reynolds stress) under different oncoming boundary layer wind conditions (i.e., offshore and onshore boundary layer winds). Figure 3-7 shows the ensemble-averaged normalized (with respect to the oncoming flow velocity at the turbine hub height) streamwise velocity distributions in the turbine wake for the offshore and onshore cases. Figure 3-8 gives the vertical profiles of the normalized streamwise velocity extracted from the PIV measurement results at different downstream locations of X/D=0.5, 1.0, 1.5 and 2.0, respectively. The results were plotted for both the offshore and onshore cases so as to assess the differences in the wake characteristics. As shown in Figure 3-7 and Figure 3-8, significant velocity deficits could be observed in the wake flow due to the fact that a portion of the kinetic energy carried by the oncoming atmospheric boundary layer wind was harvested by the wind turbine as the airflow streams passed through the area swept by the turbine blades. Furthermore, much higher velocity deficits could be seen in the proximity of the wind turbine due to the presence of nacelle and tower.

The results also revealed that the oncoming flow turbulence character could play a central role on the wake dynamics. It was found out that the velocity deficits observed in the turbine wake could be more persistent for the offshore case with relatively lower ambient turbulence levels. As shown in Figure 3-7(a), the iso-velocity contour lines with relatively lower streamwise velocity values (i.e., U/U_{hub} < 0.7) were found to extend further beyond the PIV

measurement window for the offshore case. As also inferred from Figure 3-8(a), very slight changes were observed on the vertical profiles of the normalized streamwise velocity at different downstream locations, implying a slower wake recovery rate for the offshore case. This phenomenon could be used to explain the so called 'deep array effect', which leads to the under-prediction of the wake losses in large offshore wind farms.
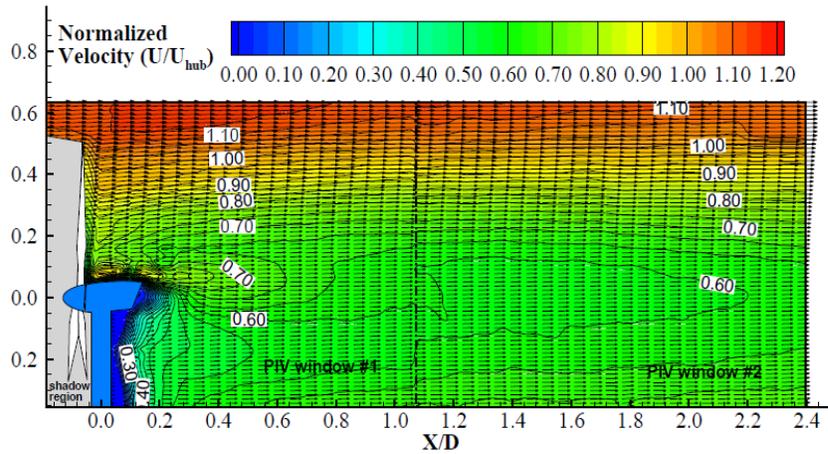
(a)
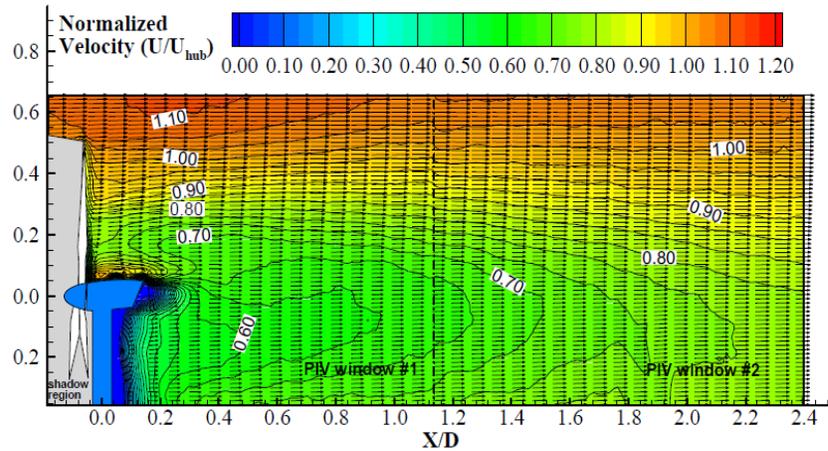
(b)

Figure 3-7 The ensemble-averaged normalized streamwise velocity distributions in the turbine wake
(a) offshore (b) onshore
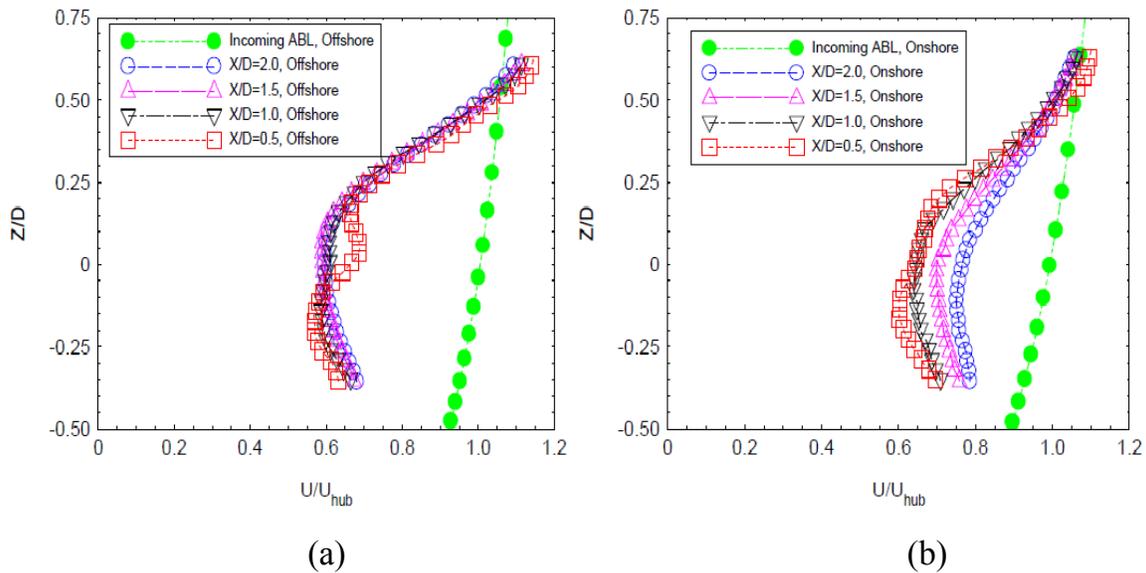
Figure 3-8 The vertical distribution of the normalized streamwise velocity in the turbine wake at different downstream locations (a) offshore (b) onshore

Moreover, the size of the region with relatively lower streamwise velocity values (i.e., $U/U_{hub} < 0.7$) were found to be much narrower for the onshore case, as shown in Figure 3-7(b). The reduced velocity deficits further downstream in the turbine wake could also be noticed from Figure 3-8(b). Therefore, the mean velocity distribution in the turbine wake was found to be strongly dependent on the oncoming flow characteristics, and the onshore case with much higher oncoming flow turbulence levels was found to reduce the velocity deficit significantly when compared to the offshore case with relatively lower turbulence levels.

Furthermore, the effect of the oncoming flow conditions on the mean flow velocity distribution in the turbine wake centerline (i.e., at the turbine hub height) can be seen clearly in Figure 3-9. In this figure, the maximum velocity deficits in two scenarios (i.e., the offshore and onshore cases) were observed at the immediate downstream of the turbine nacelle. In the region of 0.2<X/D<0.4, just after the nacelle recirculation zone, the centerline wake velocity was shown to increase sharply independent of the oncoming flow conditions. However, the wake centerline velocity distribution further downstream was quite different for the offshore and onshore cases. For the offshore case, the centerline wake velocity was found to first decrease slightly in the region of 0.4<X/D<1.5 due to the pressure gradients caused by the energy extraction, and then increase slowly further downstream (i.e., X/D>1.5) due to the turbulent mixing supressing the pressure gradient effects (Ainslie, 1988). However, the

centerline wake velocity was observed to be almost the same for the onshore case in the region of 0.4<X/D<1.0, then increase monotonically further downstream (i.e., X/D>1.0) with comparably much greater increase rate than that observed for the offshore case. Therefore, the centerline wake velocity in the onshore case was found to recover much faster than that in the offshore case, implying that the wake interference effects and the corresponding power deficits would be less severe for the downstream turbines sited in the onshore wind farms, in comparison with those sited in the offshore wind farms.
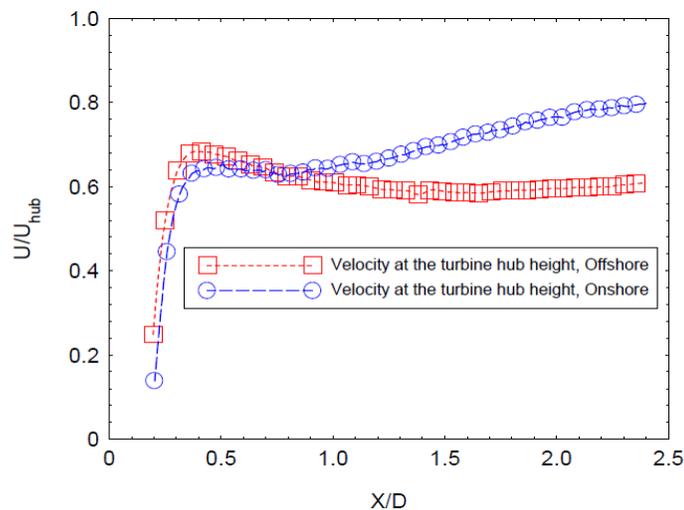
Figure 3-9 The normalized hub height streamwise velocity variation as a function of the downstream distance

Figure 3-10 gives the normalized turbulence kinetic energy ($TKE=0.5(u'^2+v'^2)/U^2_{hub}$) distributions in the turbine wake for the offshore and onshore cases, which could play a key role in the wake recovery process. As shown in Figure 3-10, although the distribution pattern of the TKE would seem quite similar for both scenarios, the absolute TKE values were found to be quantitatively very different. The absolute TKE values obtained in the onshore case were almost three times greater than those obtained in the offshore case. The regions with quite high TKE levels were found to concentrate in the wake region immediately behind the rotor, nacelle and tower of the wind turbine, which is believed to be closely related with the flow separation, unsteady shedding vortices and interactions between these wind turbine components. Furthermore, TKE levels at the upper half of the wake were found to be quite high, which is correlated well with the paths of unsteady shedding vortices in the top-tip region (Hu et al.,

2012). Previous studies also showed significantly higher TKE levels at the upper edge of the wake (Zhang et al., 2012; Porte-Agel et al., 2011; Wu et al., 2012). Moreover, TKE production at that region was found to increase and expand (wake/shear layer expansion) with increasing downstream distance in the wake.

TKE levels could be used as a parameter to indicate the extent of the turbulent mixing in a turbulent flow. Therefore, it can be deduced from these results that higher TKE levels for the onshore case would indicate much stronger mixing in the wake, leading to a faster wake recovery for the onshore case, in comparison with the offshore case. This could explain the difference, as previously observed for the offshore and onshore cases, in the wake velocity distributions.

In the present study, the added (wake-induced) TKE distributions in the turbine wake were also obtained by subtracting the TKE levels of the oncoming flow from those of the measured TKE values in the turbine wake (i.e., $\Delta TKE = TKE_{wake\ flow} - TKE_{oncoming\ flow}$). As shown in Figure 3-11, the added TKE levels were found to differ in the near (i.e., $X/D<1.0$) and far (i.e., $X/D >1.0$) wake regions for both the offshore and onshore cases. Furthermore, significant differences were observed in the TKE production at different height levels. In particular, TKE production at/below the hub height level was found to become much smaller, even negative throughout the downstream distances (i.e., $X/D > 0.5$), indicating less turbulent wake flow than the oncoming flow at that level. This is in agreement with the findings of Chamorro and Porte-Agel (2009), Zhang et al. (2012) and Wu et al. (2012). This effect was observed to be more pronounced for the onshore case with relatively high turbulence levels near the ground. In addition, a significant reduction in the TKE production for the onshore case was detected in the vicinity of the blade root section above the hub height ($Z/D \approx 0.2$). However, the TKE production at the upper half of the wake (i.e., in the vicinity of the top-tip level) was found to be much higher for the onshore case in the far wake region. The detailed explanation with further analysis on the characteristics of the TKE distributions will be given in the phase-locked PIV measurement results section since TKE production in the wake is closely related to the evolution of unsteady vortex and turbulent structures.
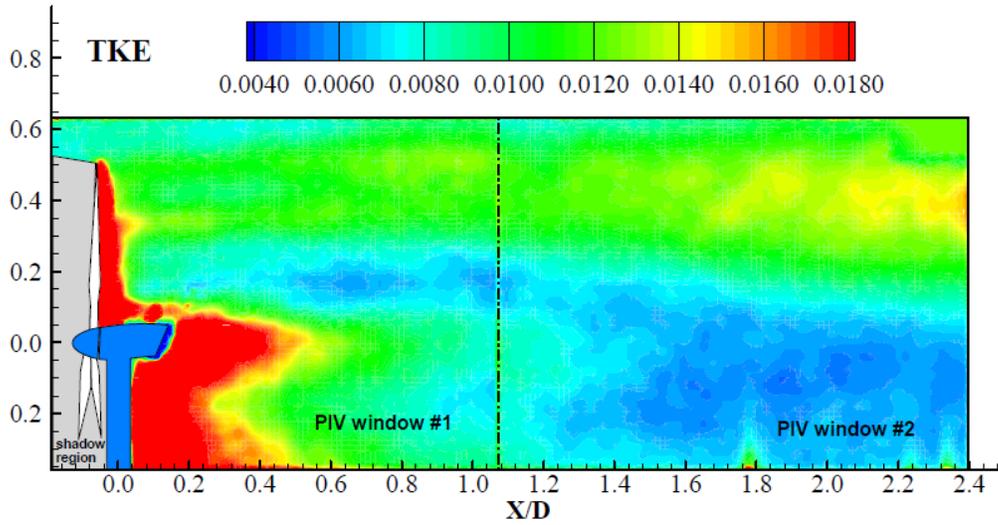
(a)
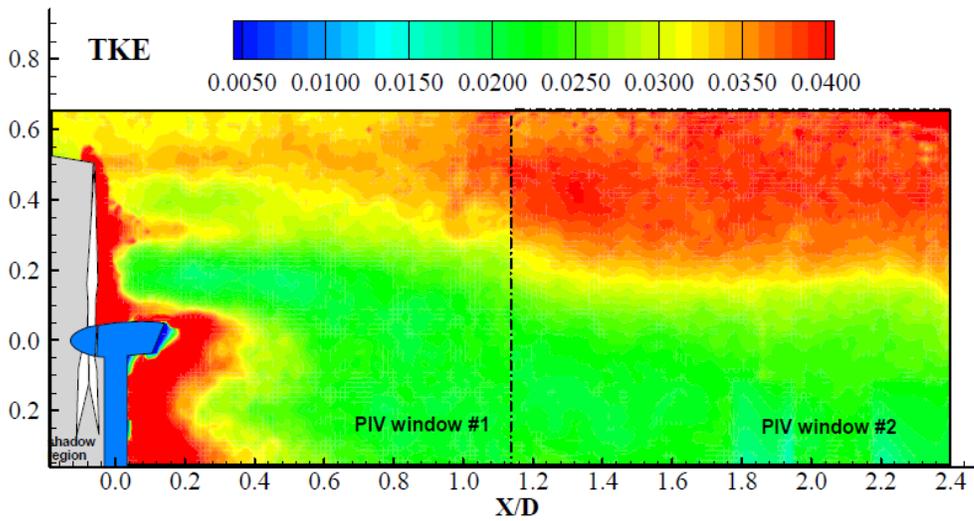
(b)

**Figure 3-10 The normalized turbulent kinetic energy (TKE) distributions in the turbine wake
(a) offshore (b) onshore**
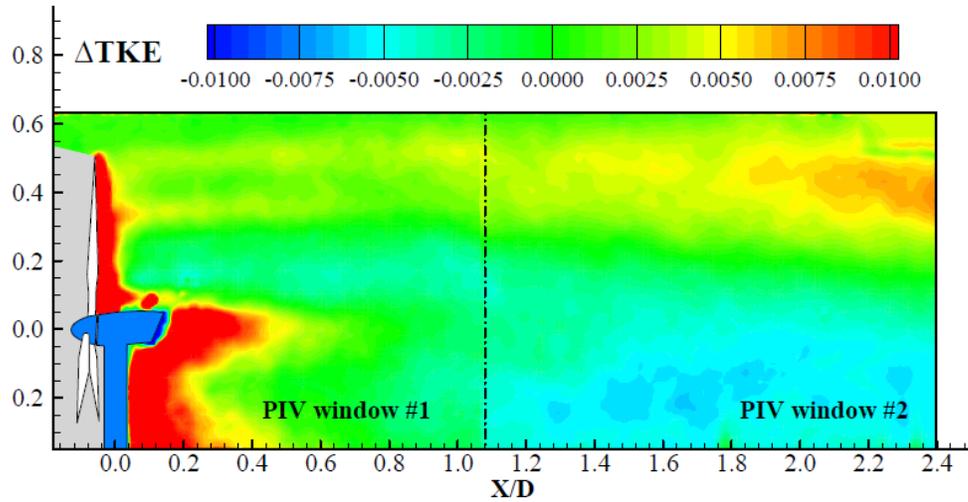
(a)
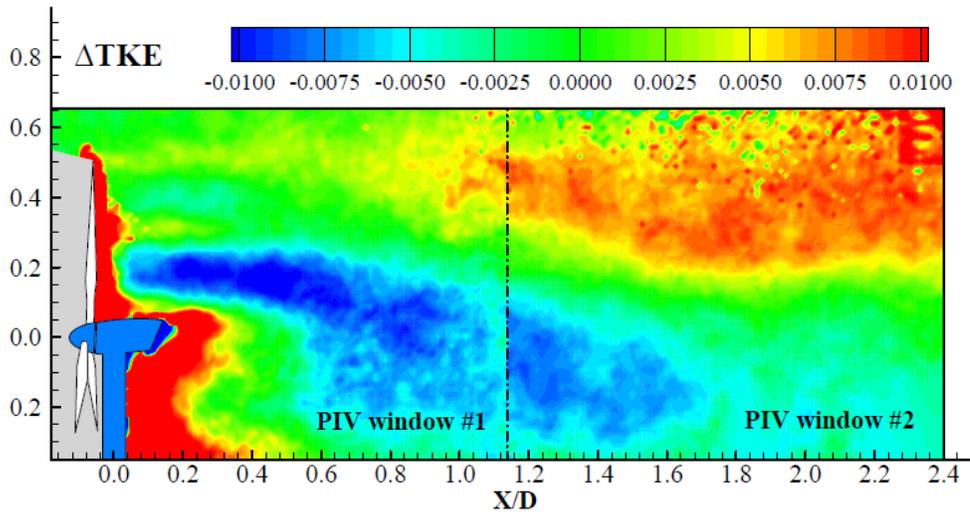
(b)

Figure 3-11 The normalized added (wake-induced) turbulent kinetic energy (ΔTKE) distributions in the turbine wake (a) offshore (b) onshore
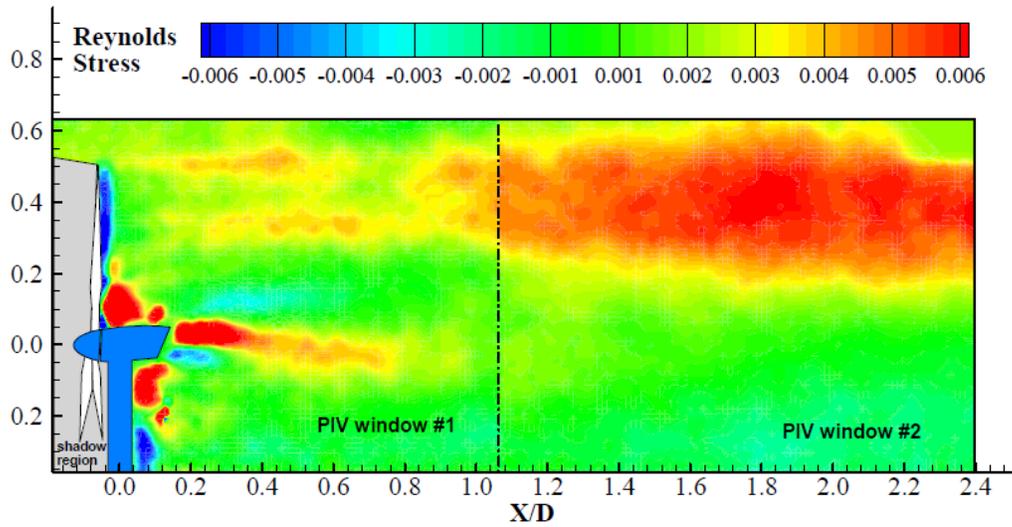
(a)
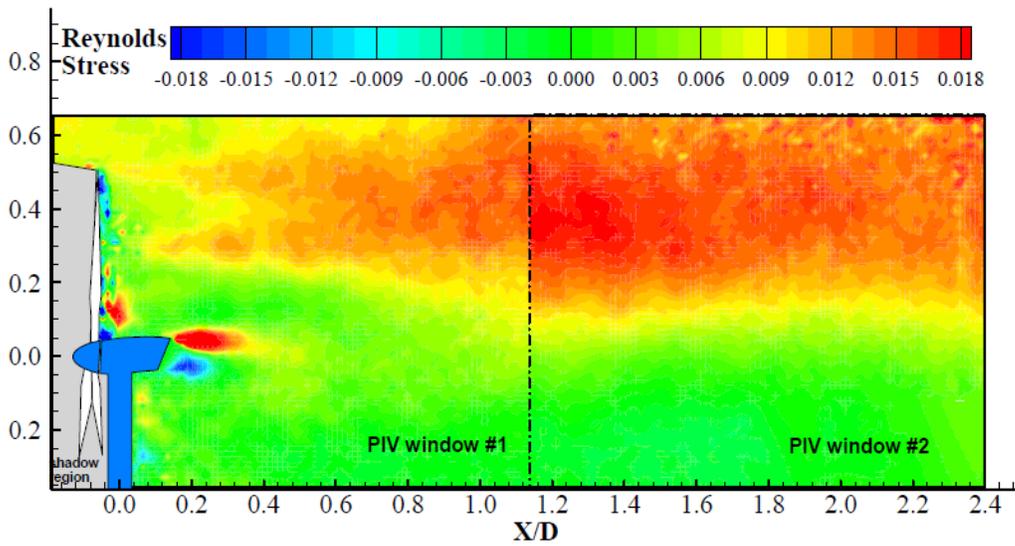
(b)

Figure 3-12 The Reynolds stress distributions in the turbine wake
(a) offshore (b) onshore

Figure 3-12 illustrates the measured Reynolds stress (in the vertical-streamwise plane) distributions in the turbine wake for the offshore and onshore cases. As mentioned by Wu et al. (2012), Calaf et al. (2010) and Cal et al. (2010), higher Reynolds stress levels at the upper edge of the wake, analogous to the TKE production, could induce stronger momentum fluxes towards the wake center, thereby playing a crucial role in vertical transport of the kinetic energy into the wake. Therefore, high-energy airflow entrained from above would re-charge the wake flow and lead to a faster wake recovery. As shown in Figure 3-12, the absolute values of the Reynolds stress observed in the wake were found to be almost three times higher for the onshore case than that of the offshore case. In addition, the uppermost region of the wake with higher Reynolds stress values was also found to expand towards the wake centerline, and as inferred from Figure 3-12, it could reach the wake centerline much faster in the onshore case, implying a faster recovery of the wake (see Figure 3-8 and Figure 3-9). Eventually, TKE and Reynolds stress distributions in the turbine wake revealed the fact that oncoming flow conditions (i.e., the distinct mean velocity and turbulence characteristics for the onshore and offshore cases) could play a key role on the evolution of the turbulent wake flow.

d) Phase-locked PIV measurement results:

In the present study, phase-locked PIV measurements were also conducted to obtain "frozen" images of the unsteady vortex structures in the turbine wake at different phase angles so that the evolution of the unsteady vortex structures in the wake could be clearly revealed. The phase angle was defined as the angle between the vertical PIV measurement plane and the position of a pre-marked turbine rotor blade. The pre-marked rotor blade was adjusted to be in the most upward position (i.e., within the vertical PIV measurement plane) at the phase angle of $\theta = 0$ deg. As the phase angle increases, the turbine would rotate out of the vertical PIV measurement plane.

Figure 3-13 shows the phase averaged normalized velocity distributions in the turbine wake at different phase angles (i.e., $\theta = 0$ deg., 30 deg., 60 deg. and 90 deg.) with the model turbine operating in two different oncoming flow conditions (i.e., the offshore and onshore cases). The existence of the wave-shaped flow structures could be observed at the top-tip height of the model turbine for the offshore case, which are associated with the formation and periodical shedding of tip vortices in the wake, as suggested in Hu et al. (2012). The wave-shaped flow

(a)   θ = 0 deg.

(b)   θ = 30 deg.

(c)   θ = 60 deg.
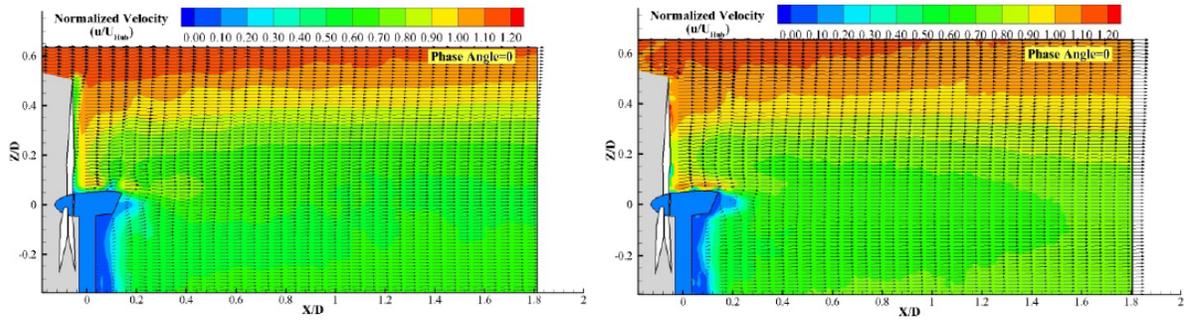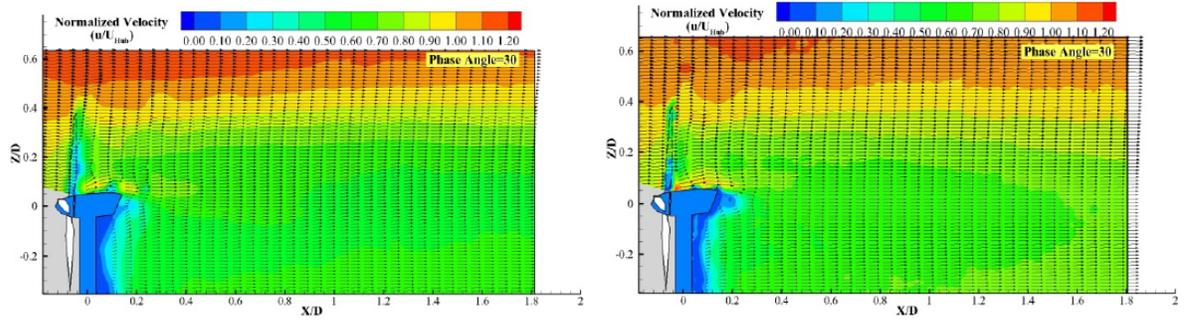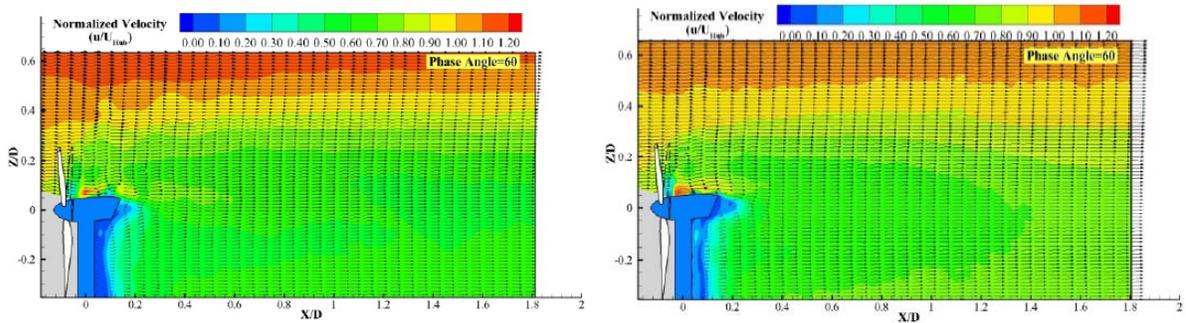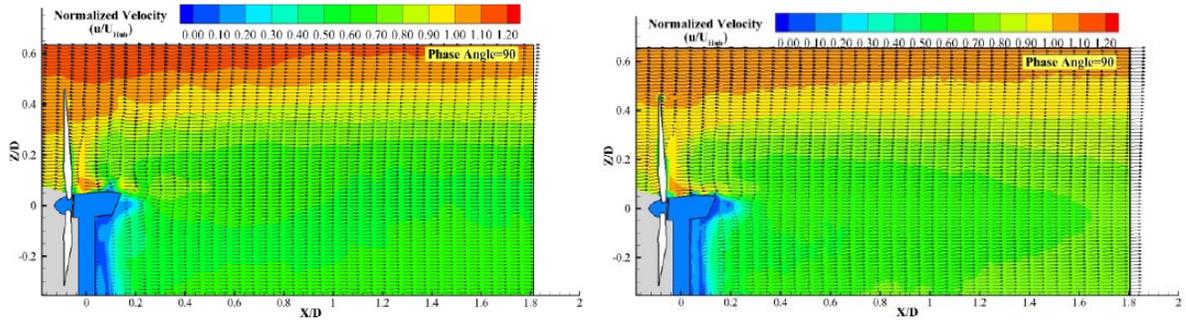
(d)   θ = 90 deg.

Figure 3-13 The phase-locked normalized velocity distributions in the turbine wake for the offshore (left) and onshore (right) cases

structures were found to propagate downstream as the phase angle increases. However, the periodicity of the wave-shaped flow structures was found to dissipate rapidly for the onshore case as they move downstream, and become almost indistinguishable in the downstream region of X/D>0.5. The rapid dissipation of these flow structures in the onshore case could be related to the higher turbulence levels in the oncoming flow.

Figure 3-14 shows the phase-locked normalized vorticity (w_z D/U$_{hub}$) distributions in the turbine wake, which were derived from the phase locked velocity distributions in the streamwise and vertical directions by using the expression $w_z = dV/dx – dU/dy$. As inferred from Figure 3-14, the wake flow behind the model turbine is a very complex flow with various vortex structures with different spatial and temporal scales. In addition to the tip and root vortices shedding from the tip and root sections of the turbine blades, unsteady vortex structures were also found on the upper and lower surfaces of the turbine nacelle along with the von-Karman vortex streets shed from the tower. Therefore, the evolution (i.e., formation, shedding and breakdown) of the unsteady vortex structures were observed to utterly dominate the wake flow behind the wind turbine.

As shown in Figure 3-14, the pre-marked turbine blade rotates out of the PIV measurement plane as the phase angle increases, and the tip vortices were found to shed from the tip of the each turbine blade forming a nicely aligned tip vortex array in the wake. Besides, an additional array of concentrated vortex structures were observed to shed from the inboard section of the turbine blade located at approximately 50% - 60% of the blade span. These structures were found to expand outwards as they move downstream and finally merge with the tip vortex structures. Similar vortex structures at 50% - 60% of the blade span were also reported by Whale et al. (2000) and Hu et al. (2012) as a result of their experimental studies on the evolution of unsteady vortex structures in the turbine wake.

The effects of the oncoming flow characteristics on the unsteady vortex structures were also illustrated in Figure 3-14 through the comparison of the phase-locked vorticity distributions for the offshore and onshore scenarios. The most significant deduction from these results would be about the dissipation/breakdown of the previously mentioned concentrated vortex structures and its dependence on the oncoming flow conditions.

(a)   θ = 0 deg.

(b)   θ = 30 deg.

(c)   θ = 60 deg.
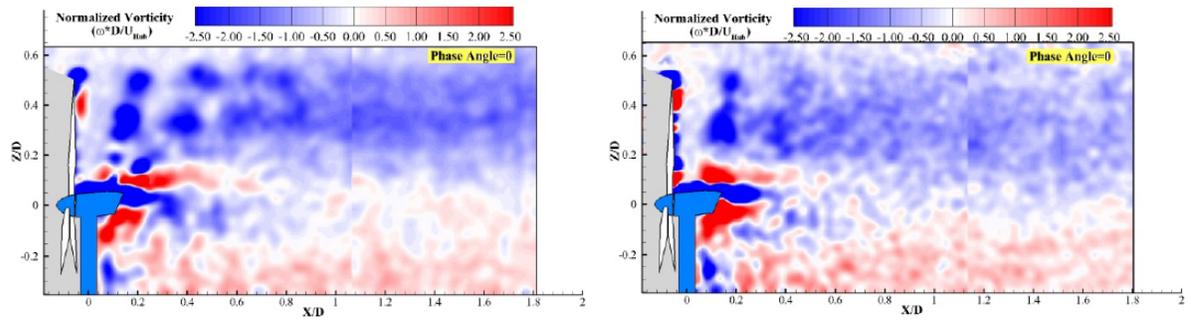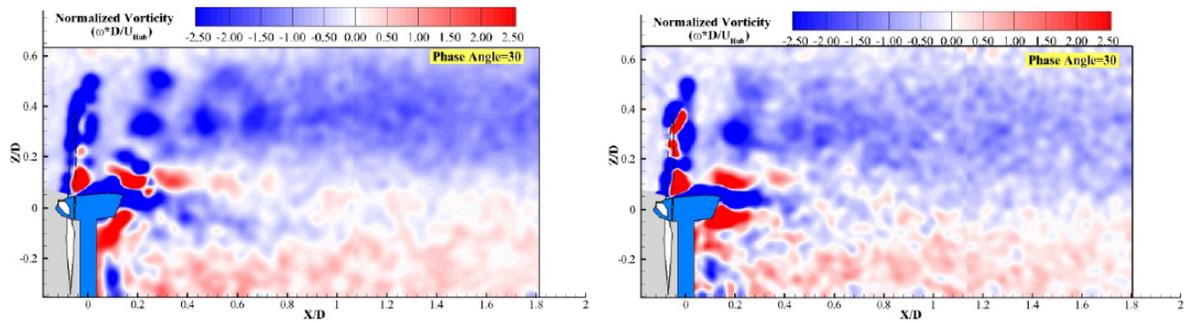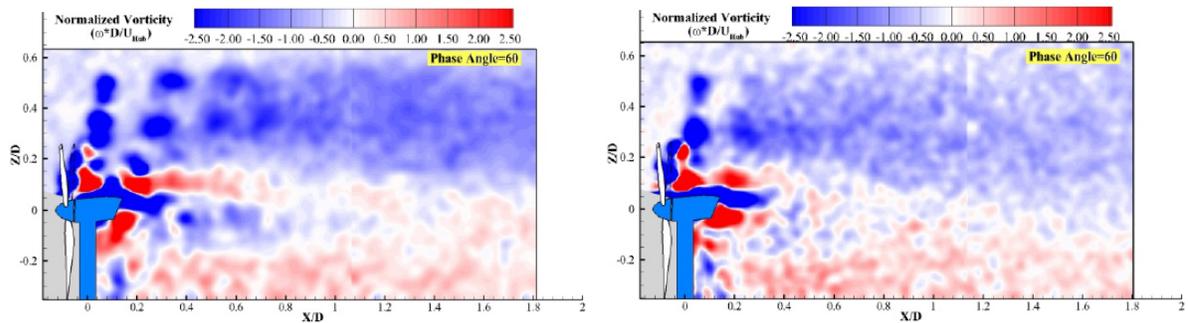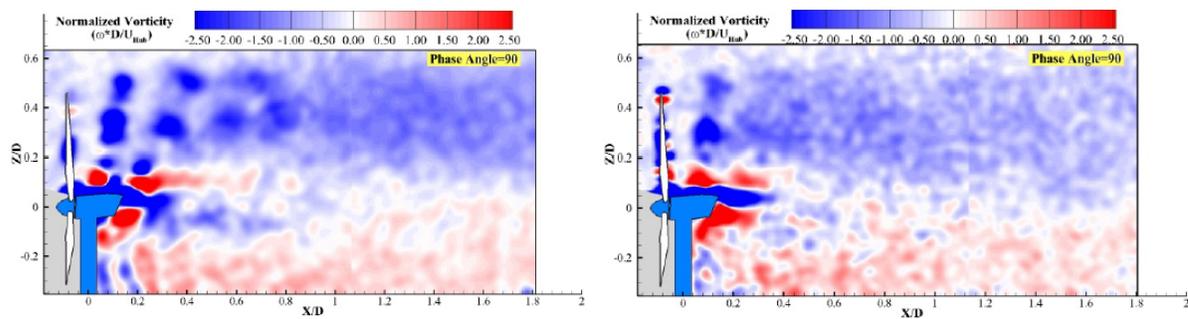
(d)   θ = 90 deg.

Figure 3-14 The phase-locked normalized vorticity distributions in the turbine wake for the offshore (left) and onshore (right) cases

As revealed from the power spectrum analysis of the dynamic thrust loads earlier, greater variations in the turbine rotational speed were observed for the onshore case, corresponding to highly turbulent conditions with respect to the offshore case. Thus, the shedding of the concentrated vortices would become highly turbulent and random, thereby inducing instabilities in the wake as they move downstream. As these wake-induced instabilities in the wake couple with the instabilities (i.e., high ambient turbulence) already exist in the flow, they would promote rapid dissipation of the vortex structures, and eventually cause vortex breakdown. Therefore, the vortex breakdown in the onshore case was found to occur much earlier (i.e., at $X/D \approx 0.4$) than the one in the offshore case (i.e., at $X/D \approx 0.8$). Furthermore, regarding to the formation of the concentrated vortices (i.e., both the tip vortices and the vortex structures at 50% - 60% of the rotor span), the formed vortices were found to be weaker and smaller in the onshore case, in comparison with those observed in the offshore case.

As previously mentioned, wake-induced TKE and Reynolds stress levels in the turbine wake were found to be much higher along the path of the shedding vortex structures, indicating the dependence of those parameters on the evolution of the vortex structures. In regards to the weaker wake vortices formed in the turbine wake for the onshore case as shown in Figure 3-14, the corresponding wake-induced TKE levels in the vicinity of the rotor were also observed to be slightly lower (see Figure 3-11) when compared with the offshore case. Medici (2005) pointed out that the formation of the concentrated tip vortices in the near wake could prevent the turbulent mixing since vortices act as a shield between the wake flow and outer high-speed flow. Thus, low levels of TKE production at the upper edge of the near wake, as shown in Figure 3-11, could be associated with the existence of the concentrated tip vortices. However, as the concentrated vortices start to dissipate and eventually breakdown, significant increase was observed in the TKE and Reynolds stress levels at the upper edge of the wake. Lignarolo et al. (2013) also noted the crucial role of vortex instability and breakdown on the TKE production. As a result, the earlier breakdown of the concentrated vortices with the corresponding higher TKE and Reynolds stress levels lead to a faster wake recovery for the onshore case, as inferred from the velocity distributions shown in Figure 3-8 and Figure 3-9, in comparison with the offshore case.

e) Power spectra of the turbulent flow velocity in the turbine wake:

In the present study, a Cobra Probe Anemometry system was also used to provide time-resolved flow velocity measurement data, particularly in the streamwise and vertical directions, at the points of interest to supplement the PIV measurement results. The fast Fourier transform (FFT) of the instantaneous streamwise and vertical flow velocities was taken in order to compare the turbulence spectra of the wake flow for the offshore and onshore cases. Thus, a comparative study based on the spectral analysis of the flow velocity in the turbine wake were carried out at the turbine top-tip height, $X/D=0.5$ downstream of the turbine, as shown in Figure 3-15. The measurement point was located along the path of the shedding tip vortices observed in the phase-locked PIV results. As inferred from Figure 3-15, significant differences were detected between the turbulence spectra of the offshore and onshore cases, which could be associated with the location of the vortex breakdown. As shown in the phase-locked PIV measurement results (see Figure 3-14), concentrated vortex breakdown for the onshore case (i.e., $X/D \approx 0.4$) were found to occur before the measurement point (i.e., $X/D=0.5$); however, it was found to occur after the measurement point for the offshore case (i.e., $X/D \approx 0.8$). Therefore, localized high-energy signatures of the shedding vortices in the offshore case could be easily identified from the spectrum plots in terms of the well-defined frequency peak corresponding to the shedding frequency ($3f_0$, where f_0 is the rotational frequency of the wind turbine) of the tip vortices and its harmonic multiples. On the contrary, it was found to be almost impossible to detect the signatures of the shedding vortices in the onshore case due to quick breakdown of the vortices before reaching to the measurement point.

Furthermore, the power spectra of the streamwise (i.e., S_u) and vertical (i.e., S_w) components of the wake velocity, as shown in Figure 3-15, were found to show similar characteristics for each case. However, as also noted by Chamorro et al. (2011), the spectrum of the vertical velocity component was found to show stronger signatures of the shedding tip vortices in comparison with the streamwise velocity spectrum. Furthermore, the features of the turbulence spectra (i.e., exhibiting the Kolmogorov -5/3 inertial subrange spectral slope) observed in the turbine wake were also reported by Chamorro et al. (2011) and Zhang et al. (2012). In addition, the spectral measurements in the wake were found to demonstrate the

same power law scaling with an inertial subrange slope of -5/3 for the offshore and onshore cases.

(a)

(b)
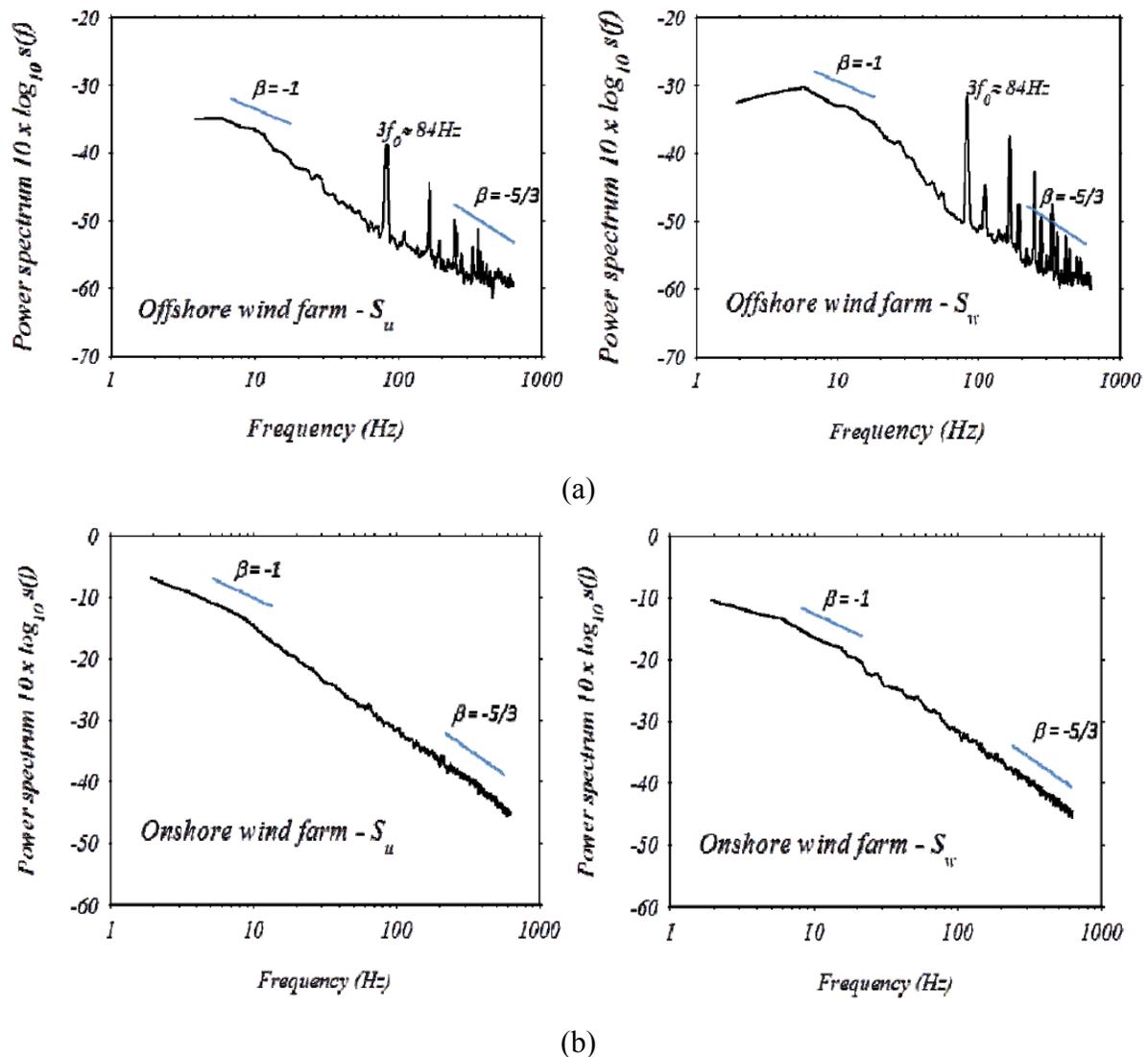
Figure 3-15 The power spectrum of the wake flow velocity at the top-tip turbine height
(a) offshore (b) onshore

3.4 Conclusion

A comparative study was conducted to investigate the turbine wake characteristics and the wind loads (i.e., the mean and dynamic) acting on a wind turbine model under two different oncoming flow conditions (i.e., the offshore and onshore cases) with distinct mean velocity and turbulence characteristics. Thus, the effect of the oncoming flow conditions on the turbine

wake was revealed through a set of flow field experiments including PIV and Cobra probe measurements along with the wind load measurements.

The significance of the rotational effects on the mean and dynamic wind loads was highlighted. Furthermore, higher levels of turbulence in the oncoming flow, as in the onshore case, were shown to cause greater fluctuations in the rotational speed of the wind turbine as well as in the wind loads acting on the wind turbine, which could impose higher dynamic loads on the wind turbine components. All these effects would be more pronounced for a turbine sited in an onshore environment, as compared to a turbine in an offshore environment.

The free-run and phase-locked PIV measurements revealed the information about the ensemble averaged flow statistics in the wake and shed light on the evolution of the unsteady vortices shedding from the wind turbine blades, nacelle and tower. The evolution of the unsteady vortices was found to be strongly dependent on the oncoming flow conditions in a way that higher levels of turbulence in the oncoming flow, as in the onshore case, were found to speed up the breakdown process of the concentrated vortex structures. Thus, this process would cause a dramatic increase in the TKE and Reynolds stress levels in the turbine wake. The higher TKE and Reynolds stress levels in the wake were found to promote vertical mixing through the transport of the kinetic energy from above, thereby re-charging the wake and facilitating the wake recovery. This effect was revealed from the velocity distributions in the turbine wake, and it was shown to be more effective for the onshore case, in comparison with the offshore case.

Moreover, the effect of the breakdown process on the strength of the tip vortices was also revealed from the power spectra of the streamwise and vertical velocity fluctuations in the near wake. The signatures of the tip vortices in the offshore case were found to be much stronger than those in the onshore case due to the slower dissipation rate of the shedding tip vortices in the offshore case.

CHAPTER 4. AN EXPERIMENTAL INVESTIGATION ON THE INTERFERENCE OF THE MULTIPLE WIND TURBINES WITH DIFFERENT LAYOUT PATTERNS IN ATMOSPHERIC BOUNDARY LAYER WINDS

4.1 Introduction

Wind turbines operate inside the atmospheric boundary layer. Thus, strong velocity and turbulence gradients inherent in the boundary layer could interact with the turbulent flow generated by clusters of wind turbines in wind farms. Understanding this interaction is of great importance for determining and optimizing the wind farm performance. However, the flow characteristics inside the wind farms are far more complicated than anticipated, involving the turbine siting (turbine separation and layout patterns), turbine size, local topography and environmental impacts as well. Intensive numerical and experimental research studies have been carried out to better understand the turbulent flow characteristics in wind farms. Corten et al. (2004) carried out a wind tunnel experiment to study the boundary layer interactions inside a wind farm with 28 wind turbines. Lebron et al. (2009) conducted Particle Image Velocimetry (PIV) measurements in the last row of a 3x3 wind farm array on different planes surrounding the wind turbine located in the center, and investigated the turbulent flow features within the wind turbine array. Furthermore, several wake models were developed to estimate the velocity deficit and turbulence levels inside a wind farm (Katic, 1986; Wessel and Lange, 2004). Moreover, Chamorro et al. (2011) studied the flow characteristics in staggered and aligned wind farm layouts in an atmospheric boundary layer flow. The focus of most of these research efforts has been on the flow characteristics inside the wind farm. However, the fundamental concern of the wind energy community is the wind turbine/farm performance. Therefore, the turbulent flow features inside wind farms should be correlated with the performances of the wind turbines so as to shed light on the relationship between wind farm dynamics and wind turbine performance.

Turbulence effects also play a central role on the wind turbine/farm performance. The studies of Sheinman and Rosen (1992) and Medici and Alfredsson (2006) have shown that the wind turbine wakes could be significantly influenced by the turbulence level of the oncoming flow. Furthermore, Chamorro and Porté-Agel (2009) studied the effects of the

boundary layer turbulence developed over surfaces with different levels of roughness on the wake structure of a single wind turbine model. Moreover, Hansen et al. (2012) found that the maximum power deficit and the wake expansion within an offshore (Horns Rev) wind farm is also a function of the ambient turbulence intensity. However, wind turbines in a wind farm could experience enhanced dynamic (fatigue) loads with an increase of up to 80% (Sanderse, 2009) due to the combined effects of ambient and wake induced turbulence. In this chapter, the main focus is on the dynamics in wind farms of variable layouts and turbine spacings, and the effect of oncoming flow turbulence on the wind turbine/farm performance and loading as well as on the flow within the wind farm.

4.2 Experimental Set-up and Procedure

a) *AABL Wind Tunnel:*

Figure 4-1 Test section of the AABL Wind Tunnel

Figure 4-1 shows a miniature wind farm (staggered) of the same sized three-bladed horizontal axis wind turbine (HAWT) models placed in a turbulent boundary layer flow developed over a surface with roughness elements such as triangular spires and chains in the large-scale Aerodynamic/Atmospheric Boundary layer (AABL) Wind Tunnel located at the Aerospace Engineering Department of Iowa State University. The AABL wind tunnel is a closed-circuit wind tunnel with a test section of 20 m long, 2.4 m wide and 2.3 m high, optically transparent side walls, and a capacity of generating a maximum wind speed of 40 m/s in the test section. The turbulent boundary layer developed in the wind tunnel is considered to be neutrally-stratified, and the growth of the boundary layer under zero pressure gradient

condition was achieved by adjusting the ceiling profile of the test section of the wind tunnel. The wind tunnel is driven by a fan and operated at 5.5 Hz, which corresponds to a free-stream velocity of 6 m/s, during the experiments.
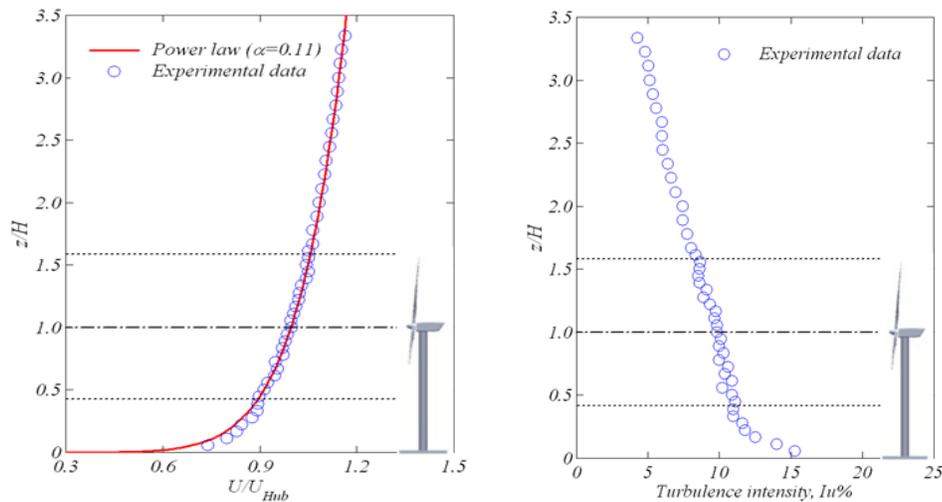
a) Boundary layer flow over smooth surface – Low turbulence inflow
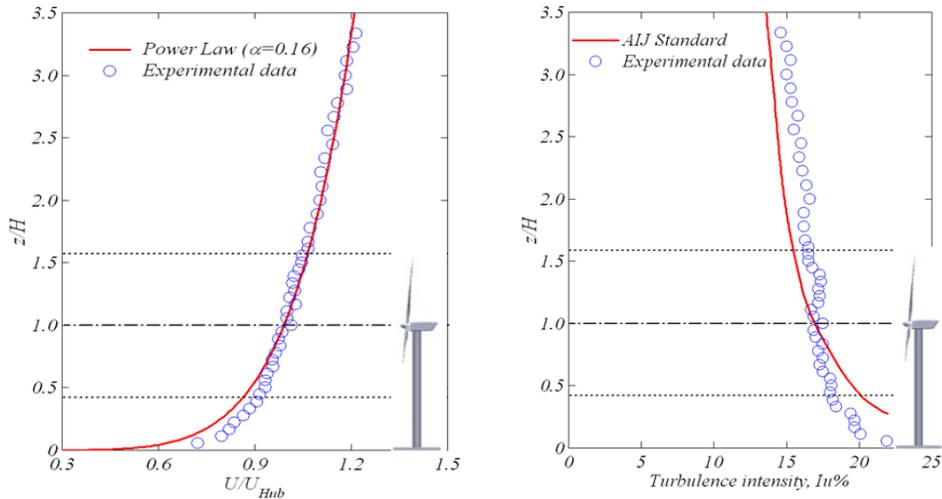
b) Boundary layer flow over rough surface – High turbulence inflow

Figure 4-2 Oncoming flow characteristics, normalized streamwise velocity (left) and turbulence intensity (right), over smooth and rough surfaces

The boundary layer developed over the smooth surface was tripped with rows of chain placed at a regular spacing on the surface of the wind tunnel floor. For the rough surface, triangular spires were set at the beginning of the test section in addition to the rows of chain.

The oncoming boundary layer flow statistics over smooth and rough surfaces are shown in Figure 4-2. The resulting boundary layer velocity profiles were then modelled by means of power law, which fitted the measured data well. According to the ASCE standard, power-law exponent 'α' for a boundary layer wind over an open terrain usually ranges from 0.1 to 0.2 depending on the terrain roughness. The measured velocity profile for the smooth boundary layer fit reasonably well with the power law fitting of $\alpha = 0.11$, which was reported as a good approximation for offshore applications under near-neutral stability conditions (Hsu et al., 1994). The corresponding turbulence intensity (9.5%) at the hub height is also in agreement with the site measurements of Hansen (2012) at Horns Rev offshore wind farm. Moreover, the power exponent of $\alpha = 0.16$ obtained from the rough case could represent the onshore boundary layer wind over open country terrain with low scrub or scattered trees based on ASCE standard (Zhou, 2002). The turbulence intensity profile for the rough boundary layer was also compared with the standard turbulence intensity profile of an atmospheric boundary layer wind over an open terrain as suggested by Architectural Institute of Japan (AIJ, 1996). Therefore, the boundary layer developed over smooth and rough surfaces during this wind tunnel investigation could be used to represent the offshore and onshore boundary layer wind characteristics, respectively.

b) The Measurement techniques:

The flow field characteristics were measured by using a Cobra Probe Anemometry system (Turbulent Flow Instrumentation) with a measuring range of 2-100 m/s, and an accuracy of 0.5%. The Cobra Probe allows for high-resolution and instantaneous measurements of vertical, lateral and streamwise velocity components, and other flow quantities such as turbulence intensity, turbulence kinetic energy (TKE) and Reynolds stresses can be derived from the instantaneous three velocity components. During the experiments, the instantaneous velocity data were sampled at 1.25 kHz for 60 seconds at each measurement location.

The power outputs from the wind turbine models were obtained by measuring the electrical voltage outputs of a small DC generator installed inside the turbine nacelle. The electrical power output of the wind turbine model can be calculated by $P=V^2/r$, where r is the electrical resistance (load) applied to the closed circuit, and V is the voltage over the electrical load. The wind turbine power coefficient is usually defined as $C_P=P/(0.5\rho U_{hub}^3\pi R^2)$. In this study, the

measured power coefficients of the wind turbine models were found to be 3%-7%, which agrees well with the data reported by Kang (2010) for small turbine models based on the electrical power output measurements. It should be noted that the power coefficients of the small wind turbine models are much smaller than those of large-scale wind turbines (i.e., 45% ~50%) mainly due to two reasons. First, as suggested by Alfredsson (1982), the maximum power coefficients would be much lower for the wind turbine models operating at low Reynolds numbers. Second, according to the study of Kang (2010), the efficiency of small DC generator would be significantly decreased by several factors such as copper losses, magnetic losses and mechanical losses, thereby causing much smaller electrical power outputs for the wind turbine models.

The steady-state (mean) and dynamic wind loads acting on the wind turbine models were measured by a high-sensitivity force transducer (JR3, model 30E12A-I40). The precision of the force transducer is ±0.25% of the full range (40N). The load cell can provide time-resolved measurements of all three components of the aerodynamic forces and the moments (torque) about each axis. The thrust coefficients (i.e., the force coefficient along stream-wise direction), bending moment coefficients (i.e., the moment coefficient along span-wise direction) and lateral force coefficients (i.e., the force coefficient along span-wise direction) of the wind turbine models were given and calculated by using the expressions of $C_T = T/(0.5\rho U_{Hub}^2 \pi R^2)$, $C_{My} = M_y/(0.5\rho U_{Hub}^2 \pi R^2 H)$ and $C_{Fy} = F_y/(0.5\rho U_{Hub}^2 \pi R^2)$, where ρ is the air density, U_{Hub} is the oncoming flow velocity at the hub height H. For each measurement, the wind load data were acquired for 60 seconds at a sampling rate of 1 kHz.

c) The Wind Turbine and Wind Farm Models:

As shown in Figure 4-3, three-bladed horizontal axis wind turbine (HAWT) models were used in this investigation. Each wind turbine model has a rotor radius of 140 mm and a hub height of 226 mm. Table 4-1 summarizes the main dimensions of the wind turbine model. With the scale ratio of 1:320, the test model would represent a commercial wind turbine in a wind farm with a rotor diameter about 90 m and a tower height about 80 m. The ratio of the blade swept area to the cross-section area in the wind tunnel was found to be less than 1.5%. Thus, blockage effects for this study would be very small, and could be neglected.
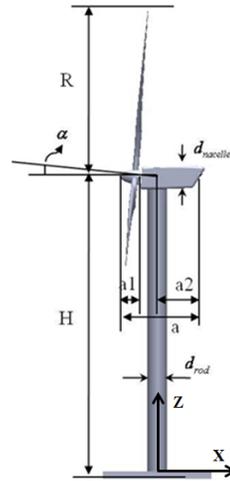
Figure 4-3 Schematic diagram of the wind turbine model

Table 4-1 The primary design parameters of the wind turbine model

Parameter	R	H	d_{rod}	$d_{nacelle}$	α	a	a1	a2
Dimension (mm)	140	226	18	18	5°	68	20	35

The wind turbine rotor blades are made of a hard plastic material by using a rapid prototyping machine. The blade sections were generated by mathematically applying a spline in tension to interpolate between the defined input stations based on the ERS-100 wind turbine blade prototype developed by TPI Composites. A constant circular cross section from the root of the blade to a distance of 5% radius of blade (R) and three NREL airfoils (S819, S820, S821) placed at various locations as inputs were used to generate the blade profile. The S821 root airfoil was used between 0.208R and 0.40R, the S819 primary airfoil was positioned at 0.70R, and the S820 tip airfoil was specified at 0.95R.

The angular velocity of the model wind turbines was adjusted by applying different electric loads (resistances) to the small DC generator installed inside the turbine nacelle. During the experiments, the angular velocity of the model wind turbines was measured by using a laser tachometer (Monarch Instrument). The angular velocity (Ω) of the models varied between 0 – 1700 rpm, and the corresponding tip speed ratio of the models (i.e., $\lambda = \Omega(2\pi/60)R/U_{Hub}$, where

U_{Hub} is the mean velocity at the hub height and R is the turbine rotor radius) was found to be varied between 0 – 4.5 for the present study.
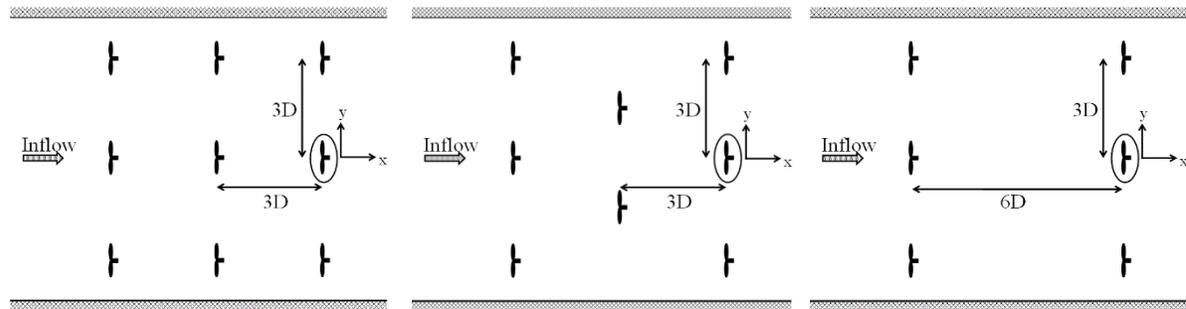
Figure 4-4 Wind farm models (a) aligned wind farm with streamwise spacing 3D; (b) staggered wind farm with streamwise spacing 3D; (c) aligned wind farm with streamwise spacing 6D

Aligned and staggered wind farm layouts were simulated in the wind tunnel, as shown in Figure 4-4. The distance between consecutive wind turbines was set to three and six rotor diameters in the streamwise direction by three rotor diameters in the spanwise direction. Thus, the effects of the turbine layout and spacing on the downstream wind turbine power output performance and loading (mean and dynamic), located in the center column of the last row as shown in the ellipses in Figure 4-4, were investigated in a wind farm. Furthermore, the overall power output performances of the aligned (4-4a) and staggered (4-4b) wind farm layouts with the same streamwise and spanwise spacing were calculated and compared. Moreover, detailed flow field measurements were conducted in the vertical and spanwise planes surrounding the downstream turbine shown in ellipses in Figure 4-4, and correlated with the downstream wind turbine power output performance and loading. The vertical measurement plane was shown as a circle in Figure 4-5, and spanwise measurements were taken at the hub height covering the span between y=-1.5D and y=1.5D. These measurements provide crucial information about the effects of turbine layout, spacing and oncoming boundary layer flow characteristics on the flow field inside a wind farm.
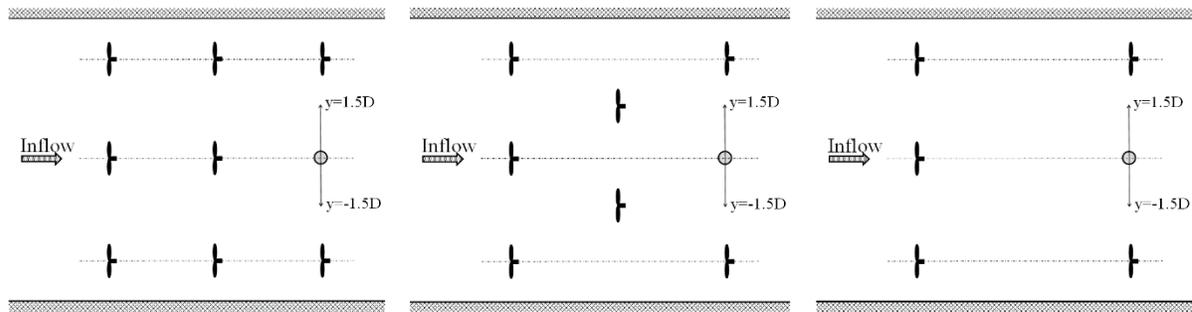
Figure 4-5 Cobra probe measurement locations (a) 3D aligned wind farm (3D); (b) 3D staggered wind farm; (c) 6D aligned wind farm

4.3 Results and Discussions

a) *Flow field measurements:*

Flow field inside a wind farm could be affected by various factors such as turbine layout, spacing and oncoming boundary layer flow characteristics. In this investigation, these factors were used as potential parameters for wind farm optimization. The particular scenarios illustrated in the present study include wind farms with aligned and staggered turbines under different oncoming flow conditions. The effectiveness of turbine spacing and staggering on the wind farm performance was further compared and discussed.

Flow field measurements (mean velocity and turbulence kinetic energy) were carried out in the vertical and spanwise planes of the selected location (see Figure 4-5) so as to shed light towards a better understanding of the flow features inside the wind farms (aligned and staggered) for different oncoming flow scenarios.

The vertical mean velocity and velocity deficit distributions for the two different oncoming flow scenarios, normalized with respect to the undisturbed turbine hub height velocity, are shown in Figure 4-6 and Figure 4-7. Staggering the turbines in the second row was found to reduce the blockage (wake) effects and allow the flow to have a longer recovery time for the downstream row, thereby reducing the velocity deficit for the downstream row in the staggered wind farm layout compared to the aligned one. Furthermore, staggering was found to impose a venturi effect on the flow inside the wind farm, which was also observed in Chamorro et al (2011). The flow through a narrower section between the staggered turbines accelerates, and this effect is noticeable when the vertical profiles of 3D staggered and 6D aligned wind farm cases are compared. The mean velocity or velocity deficit difference in these two cases (3D

staggered and 6D aligned) is not quantitatively very different, and even slightly in favor of the staggered case. Therefore, spacing between the turbines in wind farms could be reduced with the staggered configuration, causing almost insignificant or slightly favorable (due to venturi effect) flow momentum change so that the power density in wind farms could be increased.
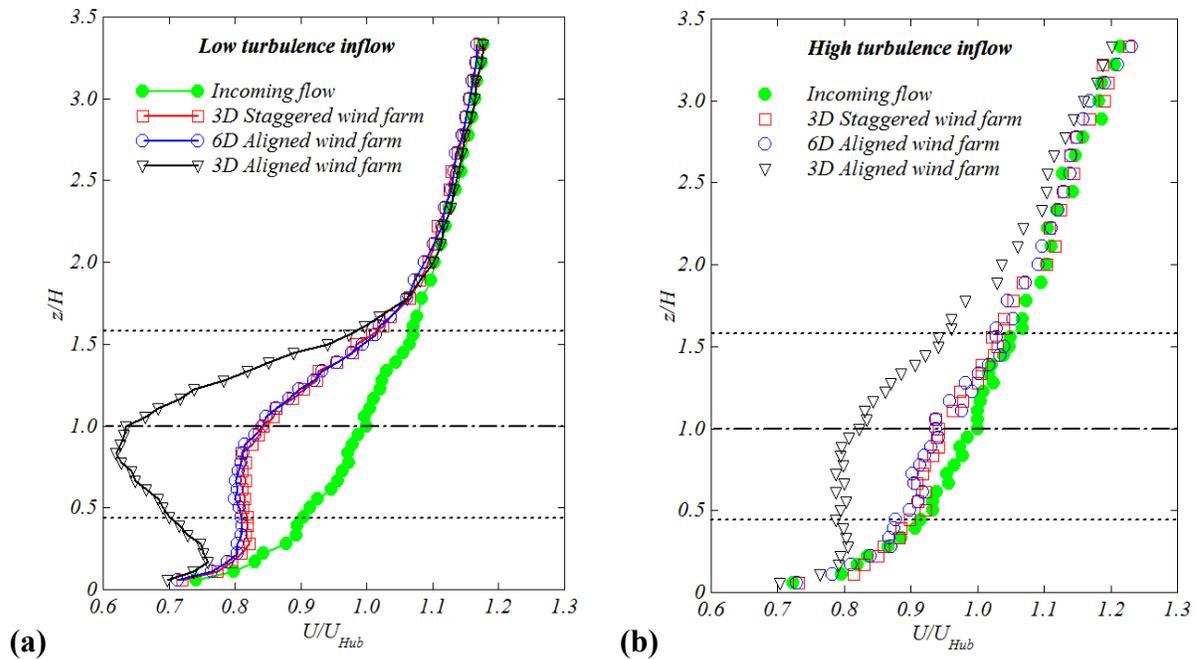
Figure 4-6 Vertical profiles of the streamwise velocity for different wind farm configurations (The two dotted lines represent the top and bottom tip height of wind turbine; the dash-dotted line represents the hub height) (a) Low turbulence inflow; (b) High turbulence inflow

The role of the oncoming boundary layer wind character on the mean velocity and velocity deficit distributions is crucial for the wake flow dynamics in a wind farm, as illustrated in Figure 4-6 and Figure 4-7. The mean velocity and velocity deficit distributions were observed to be quite different due to the ambient turbulence effects. Turbulence promotes the vertical mixing and draws high momentum air into the wake thereby resulting in a faster wake recovery. Figure 4-6 and Figure 4-7 reveal that the velocity deficit could be significantly reduced for the highly turbulent oncoming flow case. This result highlights the importance of the oncoming flow turbulence for the entrainment and vertical transport of kinetic energy fluxes in a wind farm.
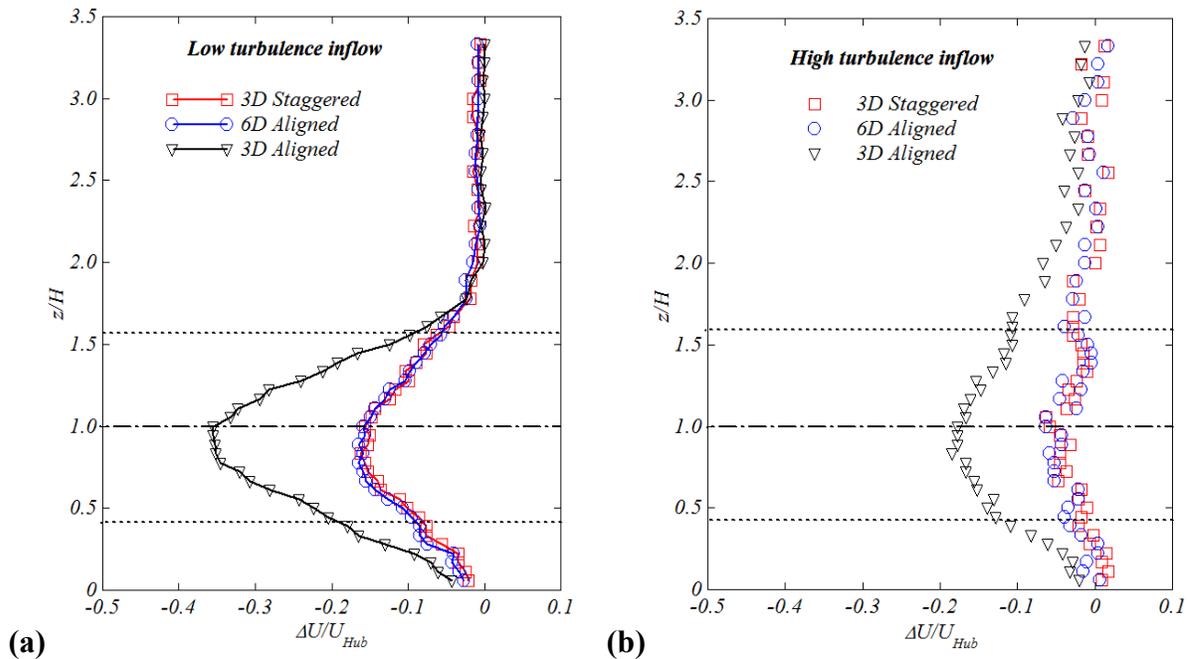
Figure 4-7 Vertical profiles of the streamwise velocity deficits for different wind farm layouts
(a) Low turbulence inflow; (b) High turbulence inflow

Furthermore, the effect of boundary layer (non-uniform) flow was found to be eliminated for the vertical profiles of the velocity deficit, as shown in Figure 4-7. Thus, they show approximately axisymmetric behavior (Chamorro and Porte-Agel, 2009) with their axes of symmetry, corresponding to the maximum velocity deficit measured, located slightly below the turbine hub-height axis due to the combined effects of nacelle and tower shadowing.

Figure 4-8 shows the spanwise (lateral) profiles of the normalized velocity at the hub height level. Apart from the previously mentioned effects of staggering and oncoming flow turbulence, vertical and lateral distributions of the turbine-induced wakes (i.e., the width of the axisymmetric region) were found to expand depending on the configuration (turbine layout and spacing) and the turbulence level of the oncoming flow. Thus, wake expansion was observed to be more pronounced, extending up to a width of 2.5H in the vertical direction and 3D in the lateral direction, in the wake of the 3D staggered case for the highly turbulent oncoming flow (see Figure 4-7b and Figure 4-8b) due to the enhanced turbulent mixing. Interestingly, higher ambient turbulence levels lead to almost uniform velocity distribution in the lateral direction throughout the wake regions between y/D= -0.5 and y/D= 0.5 for the staggered and 6D aligned layouts, as shown in Figure 4-8b.
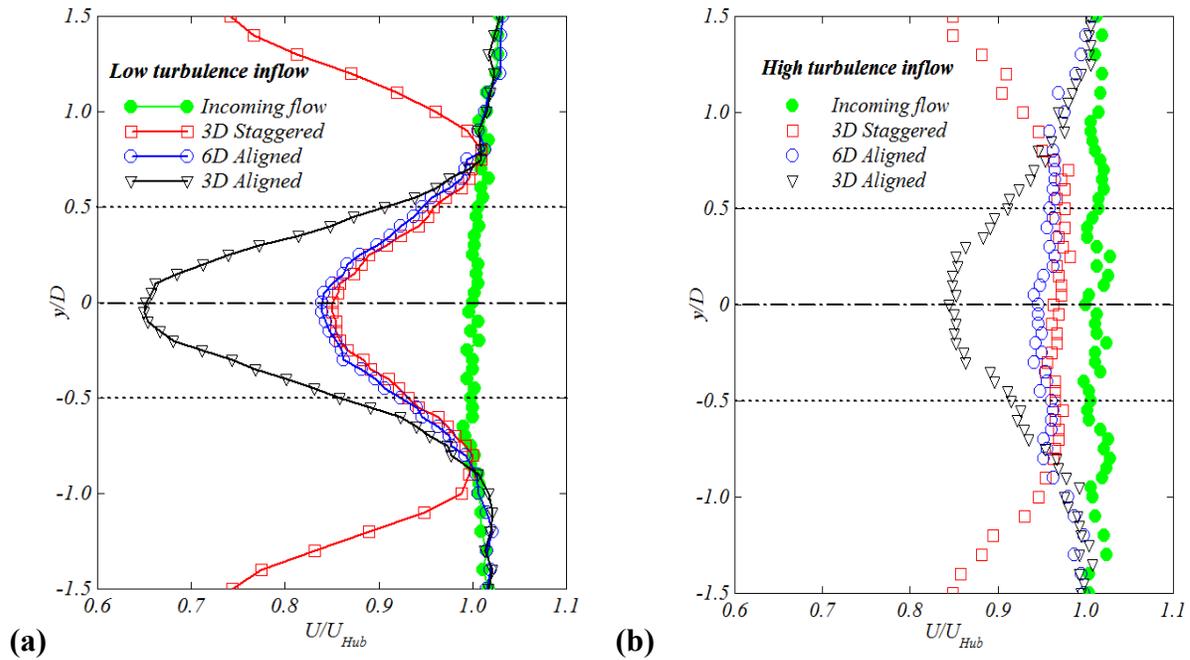
Figure 4-8 Spanwise profiles of the mean streamwise velocity for different wind farm configurations (a) Low turbulence inflow; (b) High turbulence inflow

The turbulence kinetic energy level in a wind farm is a function of the oncoming flow turbulence and wake-induced turbulence. It was previously highlighted that oncoming flow turbulence significantly affects the wake recovery rate. The velocity deficit was found to decrease as the oncoming flow turbulence level increases. Furthermore, each turbine acts as a roughness element, and induces highly turbulent flow downstream which evolves throughout the wind farm as it superimposes on each other (multiple wakes) and interacts with the oncoming (ambient) boundary layer flow.

Figure 4-9 and Figure 4-10 display the vertical and spanwise (lateral) profiles of the normalized turbulent kinetic energy ($i.e., TKE = 0.5(\overline{u'^2} + \overline{v'^2} + \overline{w'^2})/U_{hub}^2$) for the same selected downstream location of the staggered and aligned wind farm cases. The TKE distributions of the two different boundary layer types were also shown to facilitate the investigation of the turbine-induced (added) turbulence in the wake. The absolute TKE values for the highly turbulent inflow were found to be 2~3 times greater than those of the low turbulence inflow scenario.
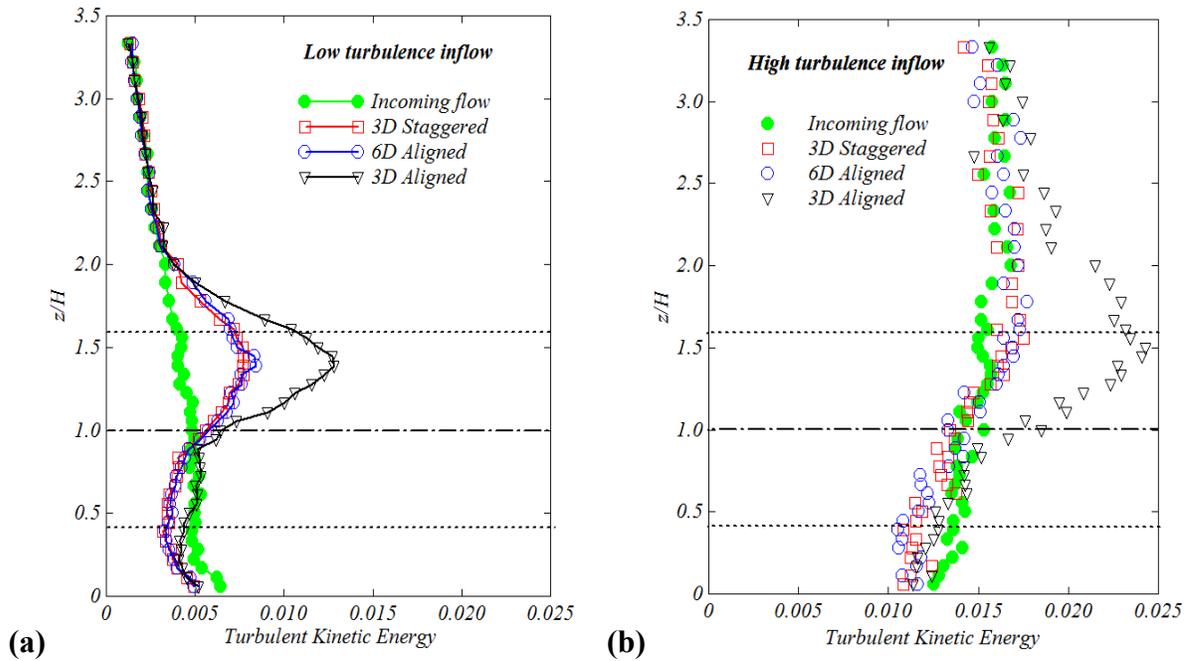
Figure 4-9 Vertical profiles of the Turbulence Kinetic Energy (TKE) for different wind farm configurations (a) Low turbulence inflow; (b) High turbulence inflow
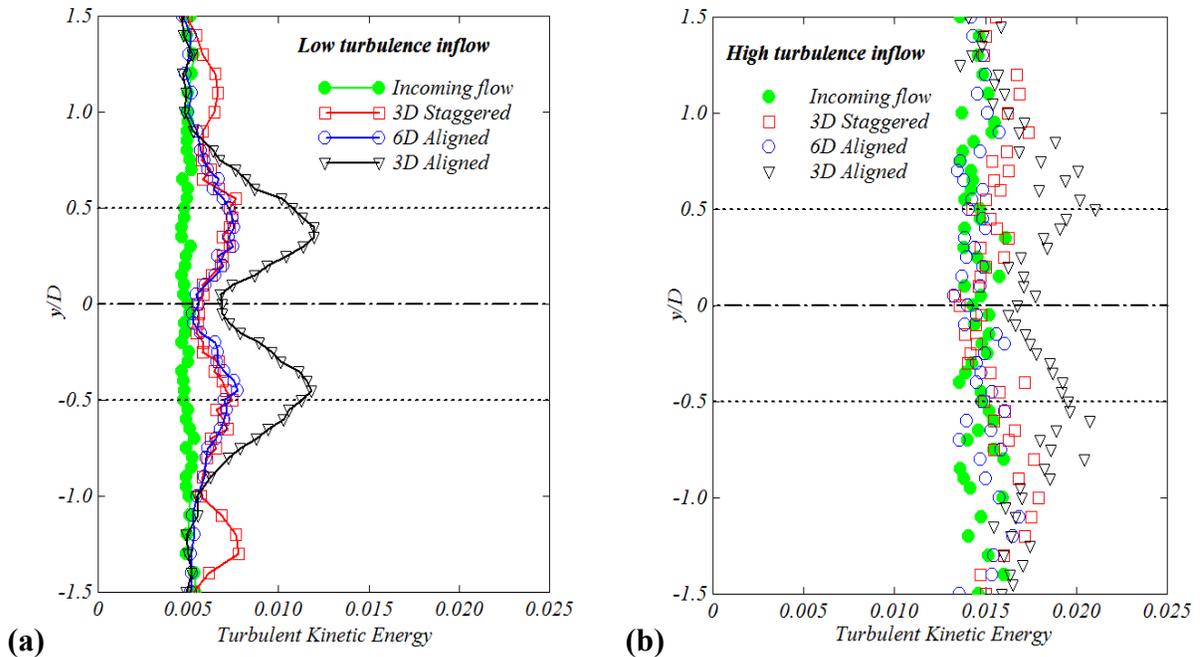
Figure 4-10 Spanwise profiles of the Turbulence Kinetic Energy (TKE) for different wind farm configurations (a) Low turbulence inflow; (b) High turbulence inflow

In Figure 4-9, there is an obvious enhancement in the magnitude of the TKE above the turbine hub-height level, and the TKE reaches the maximum near the top-tip level, which is

correlated well to the path of the unsteady tip vortices. As expected, the absolute levels of the TKE were found to be much higher for the 3D aligned layout and the TKE levels were also observed to be quite similar for the staggered and 6D aligned cases.

Furthermore, the TKE levels below the turbine hub-height level were found to become even smaller than those of the incoming flow due to the presence of the wind turbine. Similar results were also reported by Chamorro and Porte-Agel (2009), Zhang et al. (2012) and Wu et al. (2012), and Chamorro et al. (2013) associated these lower TKE levels at lower elevations (below the hub-height) with highly damped large-scale motions in the turbine wakes.

The spanwise (lateral) distributions of the TKE at the hub height level, as shown in Figure 4-10, were found to be perfectly axisymmetric for the aligned and staggered layouts unlike the vertical TKE profiles. This could be explained with the oncoming boundary layer flow characteristics with non-uniform velocity and TKE distributions along the vertical direction. Figure 4-10 also illustrates that the maximum enhancement of the TKE, associated with the strong shear and turbulence produced along the path of the shedding vortices, could appear at the near-tip regions of the rotor. However, the effect of those shedding vortices on TKE was found to be actually reduced in the wake by either staggering the turbines or doubling the spacing between the turbines (see Figure 4-10). Furthermore, TKE enhancement was also observed behind the nacelle and blade root regions; however, it was relatively lower compared to the one observed behind the near-tip blade regions, thereby suggesting a faster TKE dissipation behind the nacelle and blade root regions.

As shown in Figure 4-9 and Figure 4-10, increasing the turbine spacing or staggering the turbines could significantly reduce the TKE production in the wake, and interestingly the vertical and spanwise (lateral) profiles of TKE were observed to be quite similar for the staggered wind farm with a given spacing of 3D and the aligned wind farm with twice as much spacing (6D). The TKE distributions in the wake of those wind farm layouts were also observed to approach the incoming flow TKE distributions for the highly turbulent oncoming flow case. Moreover, the added TKE was found to be similar in both high and low turbulence inflow scenarios for the 3D aligned case. Thus, TKE production in a wind farm was found to be strongly dependent on the turbine positioning (wind farm layout) and oncoming flow (turbulence) characteristics.

b) *Mean and Dynamic Wind load measurements:*

The wind loads acting on a turbine, along with the mean and fluctuating (dynamic) components, are of great concern for the mechanical design stage of a wind turbine. (Hu et al., 2012). The most significant wind loads acting on wind turbines are usually associated with the streamwise velocity component since wind turbines align themselves with the oncoming wind. Thus, the JR3 force-moment sensor was used in the present study to measure the axial (thrust) wind loads and corresponding bending moments about the lateral axis due to the thrust loading. Table 4-2 lists the wind load measurement results in terms of the mean and standard deviation values of the thrust and bending moment coefficients, corresponding to the scenarios of aligned and staggered wind farm layouts under different oncoming boundary layer flow conditions. It is also noteworthy that these measurements were carried out on the downstream turbine, located in the center column of the last row, for each wind farm configuration. The time-averaged (mean) values of the wind loads (i.e., thrust coefficient and bending moment coefficient) were found to be significantly higher for the 3D staggered configuration in comparison to the 3D and 6D aligned configurations regardless of the oncoming flow turbulence level. The mean wind loads acting on wind turbines in a wind farm could be an indicative of the oncoming flow velocity or the velocity deficit experienced by wind turbines since they are, among other factors, function of the mean flow velocity, and proportional to the square of the mean flow velocity. Thus, these mean wind load measurement results were found to agree well with previously mentioned mean velocity and velocity deficit measurements. Therefore, significantly lower mean wind load values observed in the 3D aligned case could be related with the dramatic velocity deficit experienced by the downstream turbine (see Figure 4-7). Furthermore, the mean values of the wind loads acting on the downstream turbine for the 3D staggered layout were found to be slightly higher (up to 6%) than those acting on the downstream turbine for the 6D aligned layout. This is also in good agreement with the velocity measurement results.

Table 4-2 The mean and dynamic wind loads acting on the downstream turbine located in the center column of the last row in the wind farm

Mean and Dynamic Wind Loads	Low turbulence inflow			High turbulence inflow		
	3D aligned	3D staggered	6D aligned	3D aligned	3D staggered	6D aligned
Mean thrust coefficient, C_T	0.233	0.321	0.320	0.312	0.388	0.367
Standard deviation of thrust coefficient, σC_T	0.222	0.145	0.145	0.277	0.201	0.190
Mean bending moment coefficient, C_{My}	0.256	0.364	0.357	0.348	0.433	0.412
Standard deviation of bending moment coefficient, σC_{My}	0.230	0.133	0.133	0.275	0.199	0.194

The effect of oncoming flow turbulence level on the standard deviation of the wind loads was quantitatively presented in Table 4-2. In the present study, standard deviation of the wind loads was used as a potential parameter to consider and evaluate the fluctuating (dynamic) loads acting on the downstream turbine. These dynamic loads could significantly reduce the fatigue life of the wind turbine components (i.e., rotor blades and drive-train), and they were found to be strongly dependent on the oncoming flow turbulence and wake-induced turbulence in a wind farm. As shown in Table 4-2, larger fluctuations from the mean values of the wind loads corresponding to greater standard deviation values were observed in highly turbulent inflow conditions. This suggests that the ambient turbulence intensity should be taken into account for the optimum mechanical design of the wind turbines operating in different atmospheric boundary layer winds. Furthermore, wake-induced turbulence also plays an important role on the dynamic loading of the wind turbines in a wind farm. The greater standard deviation values of the dynamic wind loads were observed in the 3D aligned case due to the higher TKE production in the wake (see Figure 4-9). Moreover, the adverse effects of the added turbulence on the dynamic loading were found to mitigate by either staggering the wind turbines or increasing the turbine spacing in a wind farm. The standard deviation values for 3D staggered and 6D aligned layouts, as shown in Table 4-2, were found to be quantitatively very similar analogous to previously shown (Figure 4-9) TKE distributions.

Figure 4-11 shows the time histories of the instantaneous thrust force coefficients (left) acting on the downstream turbine in 3D staggered and aligned wind farms along with their corresponding frequency (right) spectra obtained through a fast Fourier transform (FFT)

analysis procedure. As revealed from the time histories given in Figure 4-11, the thrust loads in a highly turbulent inflow were found to be highly unsteady, and the amplitudes of fluctuations could be significantly higher compared with their mean values. Furthermore, staggering was found to reduce the amplitude of these fluctuations for the downstream turbine. However, as mentioned before, the downstream turbine could experience much higher time averaged (mean) thrust loads in staggered case due to the reduced velocity deficit when compared to those in aligned case with similar spacing (3D).
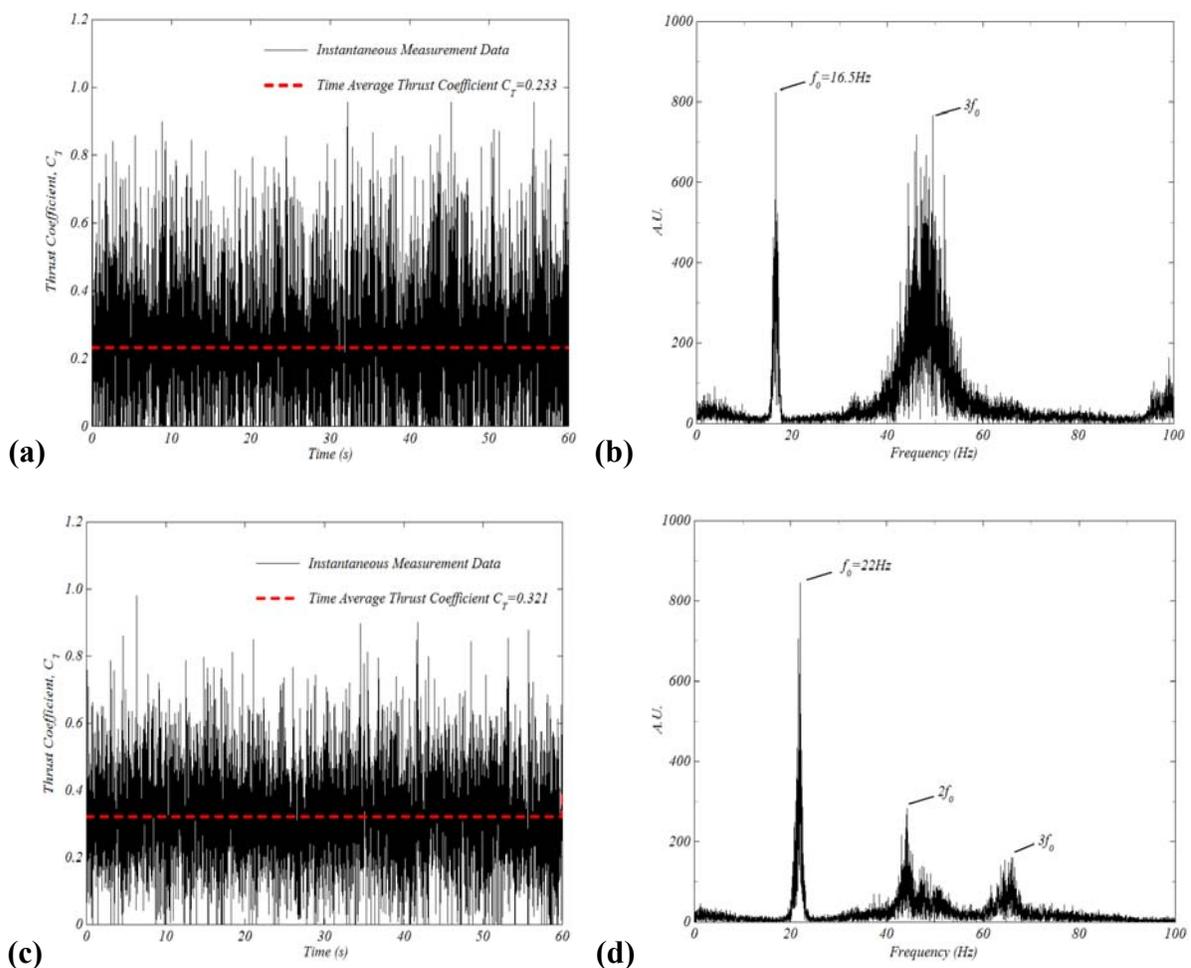
As shown in Figure 4-11 (right), a dominant frequency peak corresponding to the rotational frequency of the wind turbine rotor ($f=f_0$) could be identified in each spectrum plot. These rotational frequency values obtained from the FFT analysis of the instantaneous thrust

forces acting on the downstream turbine were found to agree well with those measured by using an optical tachometer. Other peaks ($f=2f_0$, $f=3f_0$), representing the harmonic frequencies of the turbine rotational frequency f_0, were also observed in the corresponding power spectrum. Furthermore, the rotational frequency of the downstream turbine located in 3D staggered and aligned wind farm layouts was found to fluctuate in a wide frequency region for the highly turbulent inflow case. Thus, a group of peaks were identified in the spectrum, making it hard to detect the dominant frequency peaks in the corresponding power spectrum. Moreover, these fluctuations in the rotational frequency of the wind turbine rotor would also contribute to unsteady (dynamic) wind loads acting on the turbine components.
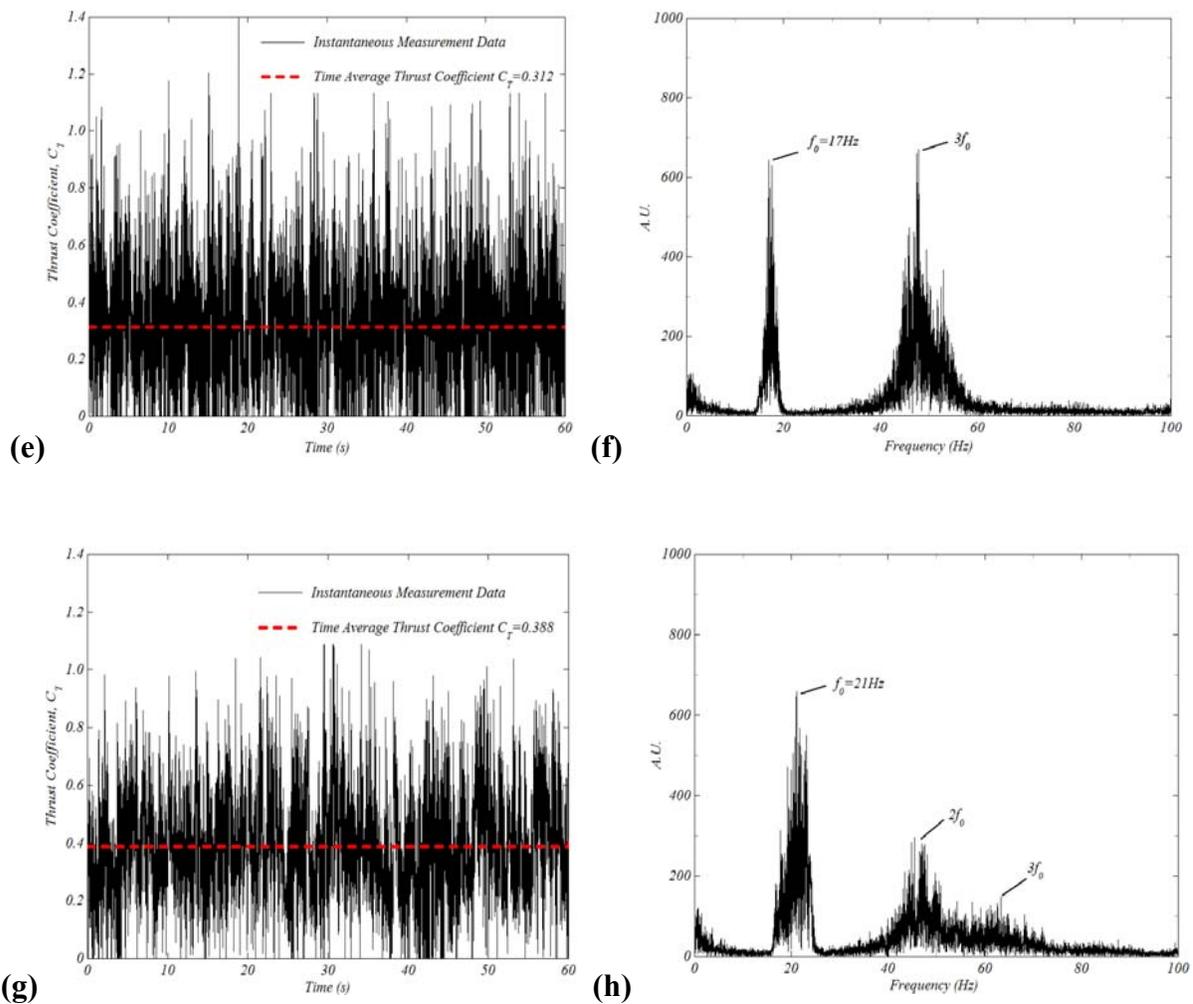
Figure 4-11 The time history of measured thrust loads (left) acting on the downstream turbine located in the center column of the last row in the wind farm along with the corresponding power spectrum (right) (a), (b) 3D aligned, low turbulence inflow; (c), (d) 3D staggered, low turbulence inflow; (e), (f) 3D aligned, high turbulence inflow; (g), (h) 3D staggered, high turbulence inflow

The effect of the wind farm layout (staggered and aligned configurations with 3D turbine spacing) on the rotational frequency of the downstream turbine was also presented in Figure 4-11. The rotational frequency of the downstream turbine was found to be much higher for the staggered configuration due to the significant reduction in the wake velocity deficit. Chamorro et al. (2011) highlighted the indirect relationship between the power output performance of a wind turbine and its rotational frequency, and compared the power output performance of the different wind farm layouts (staggered and aligned) by using a first order equation based on the change in the rotational frequency of the wind turbines through the rows of the wind farm. Therefore, the rotational frequency of the downstream turbine could also be used as an indicator to provide further insight about the power output performance and efficiency of the different wind farm layouts.

Table 4-3 The mean and dynamic lateral wind loads acting on the downstream turbine located in the center column of the last row in the wind farm

Mean and Dynamic Wind Loads	Low turbulence inflow			High turbulence inflow		
	3D aligned	3D staggered	6D aligned	3D aligned	3D staggered	6D aligned
Mean lateral force coefficient, C_{Fy}	0.009	0.017	0.015	0.012	0.011	0.008
Standard deviation of lateral force coefficient, σC_{Fy}	0.104	0.104	0.101	0.153	0.155	0.144

The measured mean values of the lateral force coefficient were found to be negligibly small (close to zero) for all cases, as listed in Table 4-3, when compared to those of the thrust force coefficient. This is due to the fact that the flow in the wind tunnel is controlled and 1-D (uni-directional) in the streamwise direction (no lateral velocity component). The existence of the wind turbines would induce three-dimensionality to the wake flow; however, these effects are pronounced in the near wake (1D~2D) so that they could hardly have any effects at 3D and 6D. Furthermore, the standard deviation values associated with the fluctuations in the lateral force were found to be quantitatively different than those in the thrust force. Although the effect of the incoming flow turbulence on the thrust and lateral wind load fluctuations was observed to be similar, the standard deviation values were found to be significantly lower for the lateral loading on the downstream turbine. Moreover, the fluctuations in the lateral force acting on the downstream turbine were observed to be almost similar for the 3D aligned and

staggered cases, thus showing that the fluctuations in the lateral force could be as crucial as those in the thrust force for the staggered wind farm layout. Therefore, the quantitative measurements on the wind load fluctuations in the streamwise (thrust) and lateral directions highlight the fact that they are strongly dependent on the oncoming flow turbulence and wind farm layout.

c) *Power output performance measurements:*

As mentioned before, the power output measurements were carried out by measuring the voltage outputs of the small DC generators installed in the nacelles of the wind turbines. Figure 4-12 shows the electrical power output performance of an unobstructed (wake-free) wind turbine as a function of the applied loads (resistances). The maximum electrical power output reading was observed at an optimum electrical loading range of 28Ω - 29Ω. The tip speed ratio (TSR) of the wind turbine was also found to change with the different loads applied. Thus, the tip speed ratio (TSR) at the optimum electrical loading range was 4.5 for the unobstructed wind turbine model.
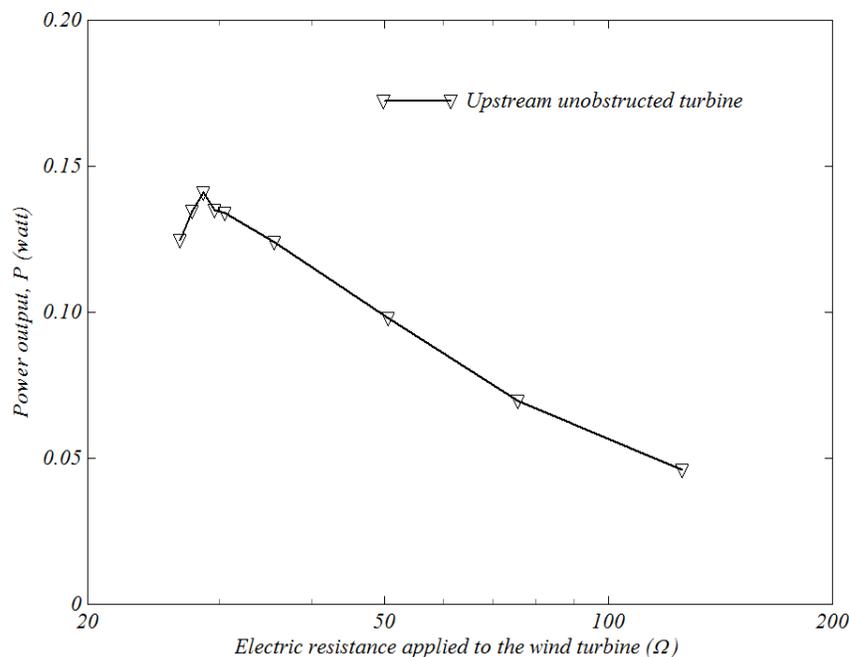
Figure 4-12 The measured power output performance of the upstream wind turbine (unobstructed) as a function of the applied electrical loads (resistances)

It is a well known fact that power losses are more pronounced for the turbines located in the downstream rows of the wind farm due to the multiple wake interaction effects. These wake effects will induce power deficits ranging from 5% up to 40% depending on several factors (Sanderse, 2009). However, the effects of the oncoming flow conditions (e.g., turbulence), and wind turbine configuration (e.g., aligned and staggered) and spacing on the wake-induced power losses are primarily the focus of present study.

Figure 4-13 shows the normalized power production from the very downstream turbine (3rd row) located in the center column of the different wind farm configurations under different oncoming flow conditions. The selected (downstream) turbine is more vulnerable to the multiple wake interference effects thereby providing more insight about the wake-induced power losses. The power outputs from the downstream turbine were also normalized with respect to its power output under undisturbed (wake-free) oncoming flow conditions in order to assess the wind turbine power deficits.
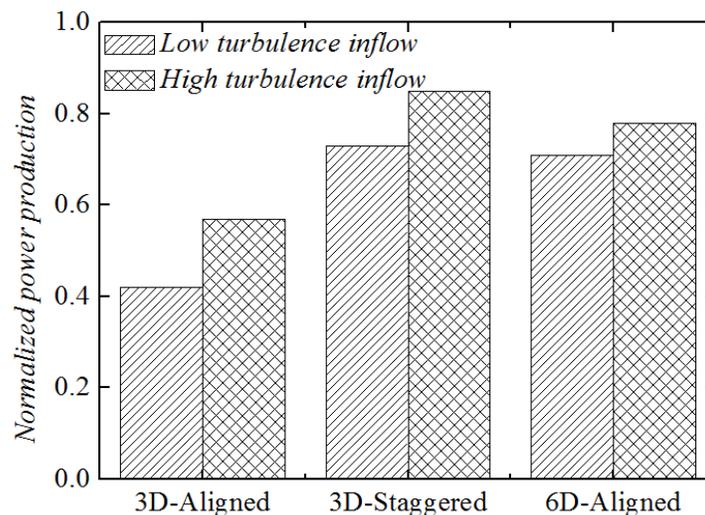
Figure 4-13 Normalized power output (P/P$_{unobstructed}$) of the downstream turbine located in the center column of the last row in the wind farm

As expected, the power deficit observed for the downstream turbine in staggered layout was found to be much lower compared to that in aligned layout with similar (3D) spacing (see Figure 4-13). The most significant contributing factor to the lower power deficit is the less dramatic velocity deficit observed in the staggered case. Thus, power output measurement

results were found to be in good agreement with the wake (velocity) measurements. Another contributing factor is the venturi effect associated with the acceleration of the flow through the narrower section between staggered turbines. This effect could be clearly seen when the downstream turbine power deficits for the 3D staggered and 6D aligned cases are compared. As shown in Figure 4-13, the power output performance of the downstream turbine was found to be still higher for the staggered case in comparison to that of aligned case with 6D (twice as much) spacing. Therefore, staggering could be as efficient as, even sometimes more efficient than increasing the turbine spacing in terms of its effect on the wind turbine/farm performance.

The power output performance of the downstream turbine in staggered and aligned wind farm layouts, as shown in Figure 4-13, was found to substantially differ depending on the oncoming flow turbulence level. As previously mentioned, highly turbulent ambient flow would trigger strong turbulent mixing and promote the vertical transport of kinetic energy thereby entraining the high-speed airflow above the wind farm. Thus, turbulence could play a central role in the wake flow recovery, and dramatic velocity deficits in the wake could be significantly reduced for the highly turbulent inflow scenario. Therefore, power deficits for the downstream turbulence were observed to be much less at highly turbulent incoming flow condition (see Figure 4-13).

Furthermore, the detailed performance analysis on a single (downstream) turbine was further extended to a wind farm efficiency investigation for the aligned and staggered wind farm layouts with the same streamwise (3D) and spanwise (3D) spacing. The wind farm efficiency was calculated by using the equation given below (eqn.1), where Cp_{Total} is the total power production from all the wind turbines in the wind farm, $Cp_{individual,i}$ is the power production from each individual wind turbine exposed to the undisturbed oncoming flow, and n is the number of wind turbines in wind farm.

$$\eta = \frac{Cp_{Total}}{\sum Cp_{individual}} = \frac{\sum_{i=1}^{n} Cp_i}{\sum_{i=1}^{n} Cp_{individual,i}} \quad (1)$$

As inferred from Figure 4-14, the staggered wind farm was found to be more efficient than the aligned one with similar spacing. The difference in the wind farm efficiency between these two configurations was on the order of 20%. Thus, staggering the wind turbines could increase

the power density of the wind farm and reduce the cost of energy in a wind farm thereby increasing the performance and profitability of the wind farm. Furthermore, wind farm efficiency was also found to be affected from the oncoming flow turbulence level. Higher turbulence level in the ambient flow was observed to enhance the wind turbine/farm efficiency, and this effect was found to be more pronounced in the staggered wind farm configuration indicating an efficient momentum/energy transfer inside the wind farm.
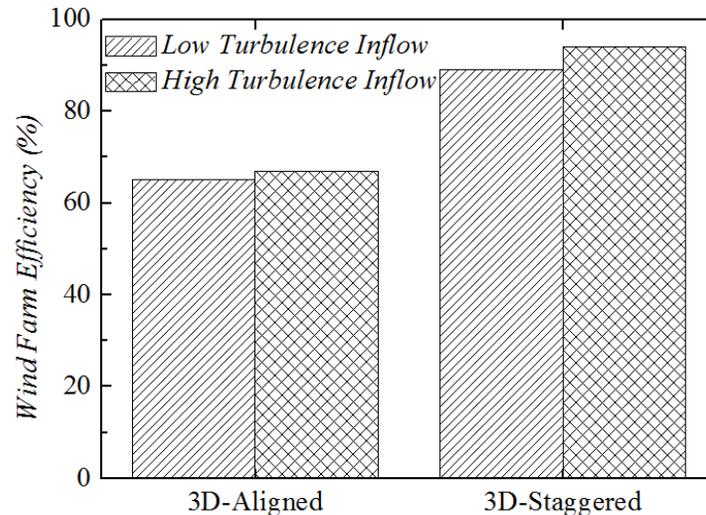
Figure 4-14 Wind farm efficieny comparison between aligned and staggered wind farm

4.4 Conclusion

A comprehensive wind tunnel investigation was carried out to study the flow characteristics inside the aligned and staggered wind farm configurations under different oncoming flow turbulence conditions. The detailed flow field measurements were correlated with the wind turbine/farm power output performance and wind loads (mean and dynamic) acting on the downstream wind turbine.

The results show that the oncoming flow turbulence, and turbine layout and spacing could significantly affect the flow dynamics inside the wind farm and the corresponding wind turbine/farm performance. The higher oncoming flow turbulence level was found to increase the wind turbine/farm efficiency through strong turbulent mixing process (ensuring a faster wake recovery); however, it was also found out to be the cause of the dynamic loading on the wind turbine components. Furthermore, the advantages of the staggered wind farm layout over

the aligned one with similar (3D) and double (6D) spacing were revealed. Staggering the turbines was found to not only mitigate the wake-induced effects but also impose a venturi effect thereby improving the power output performance of the wind turbine/farm. This study also suggests that staggering could be more effective on the wind turbine/farm performance than spacing the turbines farther apart.

The wind farm optimization is a complex problem with a lot of variables involved apart from the oncoming flow character, and turbine layout and spacing. However, the results from this investigation shed light on some aspects of the wind farm optimization, and they could be used for validating numerical models and simulations as well.

CHAPTER 5. AN EXPERIMENTAL STUDY ON THE YAW OPTIMIZATION USING TWO TURBINES IN TANDEM ARRANGEMENT

5.1 Introduction

Today, 80% of the energy in the world comes from the fossil fuels. Along with the environmental concerns about their consumption (CO_2 emissions), they are unsustainable resources, and one day we will run out of fossil fuel reserves. Thus, renewable energy sources will play an important role in solving the world's future energy crisis. Together with hydro and solar power, wind energy is becoming one of the most promising renewable energy sources with the potential to respond the world's rising energy demand.

Wind is one of the fastest-growing renewable energy resources. Today, wind is providing more than 4% of total U.S. electricity supply. However, U.S. wind industry has shown a great development over the past five years. It has added more than 35% of all new generating capacity which is more than nuclear and coal combined. Eventually, wind energy became the leading source of U.S. electricity generating capacity in 2012, providing 42% of all generating capacity (American Wind Energy Association, AWEA). The current wind energy capacity installed in the U.S. is slightly more than 60 GWs which represents more than 20% of installed wind power in the world. According to the report of U.S. Department of Energy, wind energy could provide 20% of U.S. electricity by 2030 with a total of 300 GWs of cumulative wind capacity. This goal can only be achieved by developing wind turbine technology along multiple dimensions over the next twenty years.

As large numbers of wind turbines are installed in wind farms, it raises concerns about the overall efficiency of wind farms due to the fact that downstream turbines operating in large wind arrays will suffer from the wake effects induced by the upstream ones. These effects will not only cause power degradation up to 40% for downstream turbines (Barthelmie et al., 2003; Corten et al., 2004) but also enhances the dynamic (fatigue) loading on the wind turbine blades which significantly reduces the life-time of a wind turbine (Sanderse, 2009). Thus, understanding the flow field characteristics through wind farms and how they change with the oncoming flow conditions, topology, terrain roughness, and upstream turbine operating conditions are necessary for wind farm optimization.

Site selection (topography) is very crucial for maximizing the energy yield from the wind turbines since even a smaller increase in the wind speed will result in a larger gain in power or vice versa. As the wind market continues to grow, wind turbines are placed on various types of terrains with complex topological characteristics. The wind flow over complex terrains such as hills, ridges and escarpments and how it interacts with the wind turbines is an area of great interest. Tian et al. (2013) investigated the flow characteristics over a 2D-Ridge model in the wind tunnel and reported that the flow will experience higher wind speeds (speed-up effect) and reduced turbulence levels on the top of the Ridge. However, the flow over a hilly terrain is also dependent on the slope of the hill, and largest speed-ups can be observed at moderate slopes (Arya, 1988). It has been reported that separation occurs at steeper slopes (18° - 20°) and it could entirely change the flow field over the terrain (Kaimal and Finnigan, 1994). The turbines located on the separation side would suffer from reduced mean flow wind speeds and enhanced turbulence levels. Therefore, complexity of the terrain should be taken into account when siting the wind turbines.

Wake interference effects in large arrays of wind turbines are of great importance for the wind farm power generation. Power losses due to these effects will go up to 23% depending on the spacing and alignment of wind turbines (Adaramola & Krogstad, 2011; Barthelmie, et al., 2009; Dahlberg & Thor, 2009; Beyer et al., 1994). Hence, there have been extensive studies on how to arrange wind turbines – spacing and layout – in such an organized pattern so as to minimize the wake interference effects.

Wind turbines in large wind farms are generally spaced with an optimum spacing (7D) in order to harness as much energy from the wind as possible without interfering the wake of upstream turbines. Meneveau and Meyers (2012) suggested that optimal average spacing is considerably higher (15D) than currently used in wind farm implementations. Wind tunnel investigations on the wind turbine wakes also showed that even at 20D spacing, wake effects are still persistent (Chamorro & Porte-Agel, 2010). However, putting the turbines far apart in a wind farm is not economically and spatially feasible.

Besides, numerous studies have been carried out on the wind farm layout (i.e., staggered turbine layout vs. aligned turbine layout) optimization to maximize the wind farm power production. It was found that, compared to the aligned counterpart, staggered wind farm layout

could improve the total power production performance for a given wind farm. Chamorro et al. (2011) suggested that the difference in total power production between a staggered wind farm and an aligned wind farm with the same oncoming flow is on the order of 10% when the turbines are spaced 5D and 4D in the streamwise and spanwise directions, respectively. Similar results were also reported by Tian et al. (2012), who revealed that 12% power increase can be achieved when the staggered layout was adopted with spacing of 3D in both streamwise and spanwise directions for an onshore wind farm with a relatively high turbulence level in the oncoming ABL wind. Moreover, Tian et al. (2012) also reported that the wake velocity deficit would recover much faster with a higher turbulence level in the oncoming flow (i.e., for the cases in typical onshore wind farms), compared with the oncoming flow with relatively low turbulence level (i.e., for the cases in typical offshore wind farms).

Adaramola & Krogstad (2011) suggested that the power output from downstream turbines can be significantly improved by operating the upstream turbines slightly outside the optimum settings or yawing the upstream turbines. As a result, the total power production of the turbines could be increased up to 12% by yawing the upstream turbine. They also claimed that operating the upstream turbine at an appropriate yaw angle and using relatively small spacing between the turbines, the efficiency of the wind farm would be comparable to that with non-yawed upstream turbine and much greater spacing between the turbines. Therefore, operating the upstream turbine at a suitable yaw angle will not only enhance the wind array efficiency, but also reduce the turbine spacing required for a given wind farm.

This chapter demonstrates a comprehensive experimental study which was performed in a large-scale Aerodynamics/Atmospheric Boundary Layer (AABL) Wind Tunnel located at the Aerospace Engineering Department of Iowa State University. The performances of two wind turbine models in tandem arrangement with 2D spacing were tested on different upstream wind turbine yaw conditions to confirm the effectiveness of using yaw angle optimization method and further investigate the dependence of this method on the oncoming wind turbulence level. The turbulent wind flow conditions in the wind tunnel were adjusted by using roughness elements (i.e., spires and chains) to simulate the atmospheric onshore (i.e., open terrain II) and offshore (i.e., open terrain I) wind conditions. The turbine rotational speeds and power outputs, the wind loads (i.e., both the aerodynamic forces and bending moments) acting on the wind

turbines, and the wake flow characteristics (i.e., X/D=2D) behind the upstream wind turbine were measured and compared quantitatively for different oncoming wind conditions.

5.2 Experimental Set-up and Procedure

a) AABL Wind Tunnel:

The experimental study was conducted in the Aerodynamic/Atmospheric Boundary Layer (AABL) Wind Tunnel located at the Aerospace Engineering Department of Iowa State University. The AABL wind tunnel is a closed-circuit wind tunnel with a test section of 20 m long, 2.4 m wide and 2.3 m high, optically transparent side walls, and a capacity of generating a maximum wind speed of 40 m/s in the test section. Roughness elements such as spike structures, chains and/or array of wood blocks were placed on the wind tunnel floor upstream of the test section in order to generate a turbulent boundary layer flow similar to the atmospheric boundary layer (ABL) wind seen in onshore and offshore wind farms. The atmospheric boundary layer simulated in the wind tunnel is considered to be neutrally-stratified due to the fact that there is no external heating/cooling process affecting the thermal buoyancy of the oncoming flow. The boundary layer growth of the simulated ABL wind under zero pressure gradient condition was achieved by adjusting the ceiling profile of the test section of the wind tunnel. The wind tunnel is driven by a fan and operated at 5.5 Hz, which corresponds to a free-stream velocity of 6 m/s, during the experiments.

The oncoming flow conditions in the wind tunnel were adjusted by using roughness elements (i.e., spires and chains) in order to simulate the atmospheric onshore (i.e., open terrain II) and offshore (i.e., open terrain I) boundary layer wind conditions. Power law, the most frequently used model in the wind industry, was used to define the simulated boundary layer wind velocity profiles, i.e., $U(z) = U_{Z_G} \left(Z / Z_G \right)^{\alpha}$, where U_{Z_G} is the wind velocity at a reference height of Z_G . The measured boundary layer wind velocity profiles are shown in Figure 5-1, where hub height, Z_{hub} , is used as a reference height and U_{hub} is the wind velocity at the hub height. The horizontal axis represents the non-dimensional averaged wind velocity U/U_{hub} with U_{hub} being the reference velocity at the hub height of the wind turbine, and the vertical axis of the figure is the non-dimensional height Z/Z_{hub}.

According to the ASCE standard, power-law exponent α for a boundary layer wind over an open terrain usually ranges from 0.1 to 0.2. The value of the power-law exponent is determined by the terrain roughness, i.e., $\alpha = 1/8.4$ according to the ISO standard and $\alpha = 1/8$ according to the GL (Germanischer Lloyd) offshore rules (reported by Argyriadis), both can be used for offshore applications. The measured velocity profile for open terrain I, as shown in Figure 5-1(a), fit very well with the suggested ISO and GL offshore wind profiles. Hsu et al. (1994) also reported that for offshore applications, $\alpha = 0.10$-0.11 is a good approximation under near-neutral stability conditions. However, $\alpha = 0.14$ or $1/7$ is suggested for onshore engineering applications. Moreover, IEC standard for onshore wind turbines uses a power-law exponent of $\alpha = 0.20$. Figure 5-1(b) shows the measured velocity profile for open terrain II which is represented reasonably well with the curve fitting of $\alpha = 0.14$. Therefore, the oncoming velocity profile of the simulated boundary layer wind for open terrain I and open terrain II is very similar to those seen in offshore and onshore wind applications, respectively.
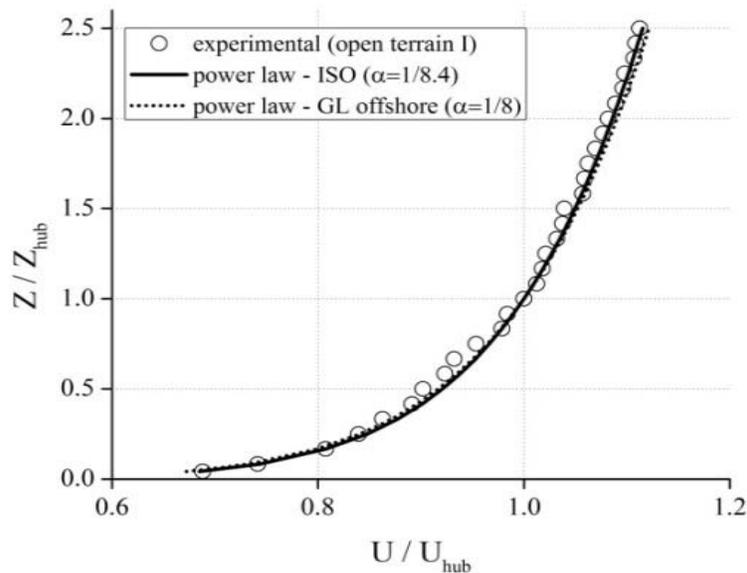
(a) Open terrain I – offshore boundary layer wind
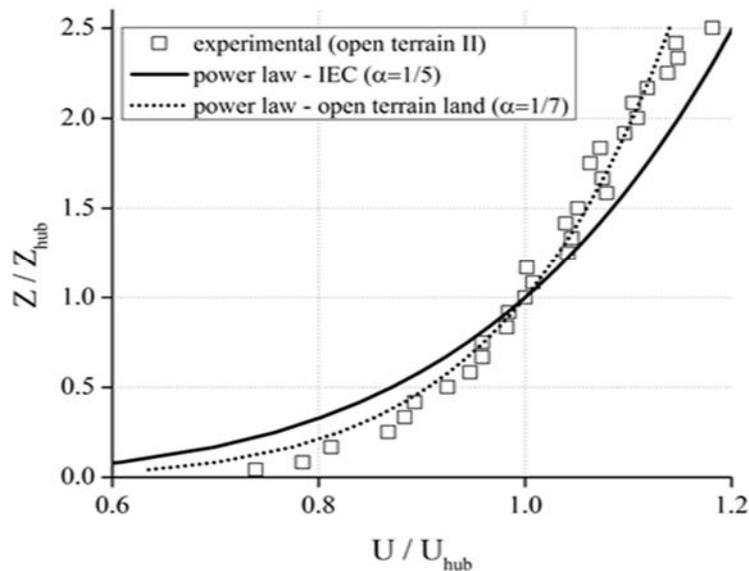
(b) Open terrain II – onshore boundary layer wind

Figure 5-1 Measured mean flow velocity profiles

It is known that there are vast differences between onshore and offshore boundary layer wind characteristics. Mean wind speeds observed offshore are often considerably higher than those observed onshore. On the other hand, turbulence or gustiness of the offshore wind is significantly lower than onshore wind. Figure 5-2 shows the measured streamwise turbulence intensity of different boundary layer flows as a function of the normalized height (Z/Z_{hub}). Mechanical turbulence generated by the roughness elements on the wind tunnel floor determines the overall turbulence level in the wind tunnel since it is operating under nearly-neutral condition.

The GL-regulations for offshore wind turbines define a constant turbulence intensity of 12% at the hub height which was found to be very conservative compared to the field measurements. Typical hub height turbulence intensity for offshore wind turbines is around 8%, indicated by *Wei Tong* in '*Wind Power Generation and Wind Turbine Design*', which is in good agreement with the measured hub height turbulence intensity value of 9% for open terrain I, as shown in Figure 5-2. Therefore, boundary layer wind turbulence profile for open terrain I fit reasonably well with the offshore wind turbulence characteristics.

Unlike offshore wind turbines, onshore wind turbines could experience higher turbulence levels depending on the atmospheric thermal stability and terrain roughness. Wharton et al. (2012) defined turbulence threshold levels for every atmospheric stability condition from strongly stable to strongly unstable (convective). They indicated a hub height turbulence threshold level ranging from 10% to 13% for neutral stability conditions. However, the measured hub height turbulence intensity value of 17% for open terrain II, as shown in Figure 5-2, is due to the mechanical turbulence caused by the combined effects of roughness elements on the wind tunnel floor. Therefore, boundary layer wind characteristics in open terrain II is analogous to those observed on land.

Figures 5-3 illustrates the histograms of the measured hub height wind velocity for open terrain I and open terrain II fitted by Weibull distribution curve. While the horizontal axis of the histograms represents a non-dimensional, u/U_{mean} which is the ratio of instantaneous wind velocity to the mean wind velocity, the vertical axis is showing the number of occurrences for every u/U_{mean} with a bin size of 0.05. The shape of the Weibull distribution curve depends on the oncoming boundary layer wind turbulence, and the breadth of the distribution tends to be wider as the wind turbulence increases. Therefore, the Weibull distribution curve for open terrain II is wider compared to that for open terrain I due to the higher boundary layer wind turbulence which results in greater variations in the wind velocity.
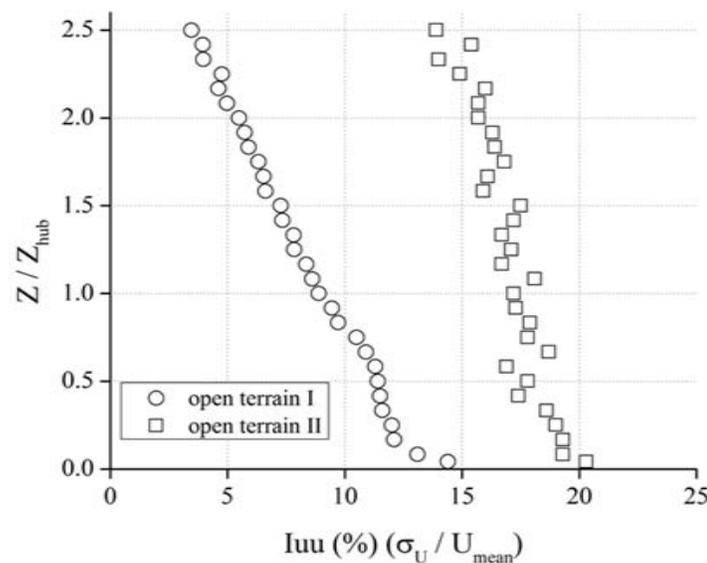
Figure 5-2 Measured turbulence profiles
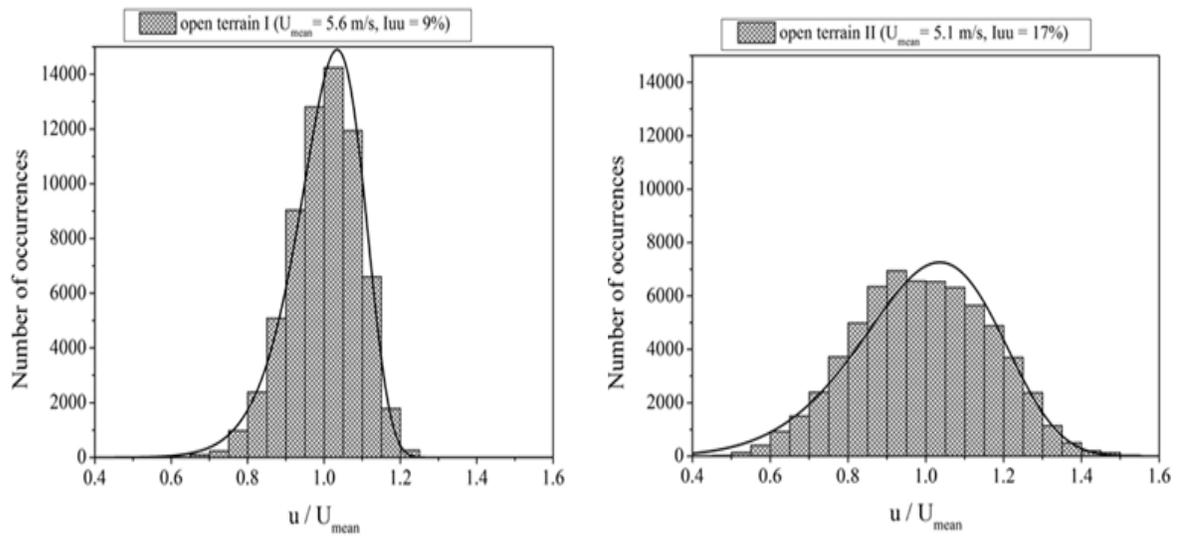
Figure 5-3 Histograms of the measured hub height wind velocity

b) The Wind Turbine Models used in the present study:

Figure 5-4 The wind turbine models in tandem arrangement and blade cross-section

The wind turbine models used for the present study represent the most widely used upwind type three-bladed horizontal axis wind turbines (HAWT) found in onshore and offshore wind farms. Figure 5-4 illustrates two wind turbine models installed on the wind tunnel floor in tandem arrangement (left) along with the typical cross section profiles of the turbine rotor blades (right). An upstream turbine is placed on a turn-table so that orientation of the wind turbine model with respect to the oncoming wind (yaw misalignment) could be adjusted. All the wind turbine models used in the present study have the same rotor radius of 191 mm and hub height of 305 mm. It should be noted that the blockage ratio of the wind turbine models

(i.e., the ratio of the turbine blade swept area to the cross-section area of the wind tunnel) was found to be about 2%, thus, the blockage effect of the wind turbine models in the test section is negligible.

The wind turbine rotor blades are made of a hard plastic material by using a rapid prototyping machine. The blades have the same airfoil cross sections and platform profiles as ERS-100 prototype turbine blades developed by TPI Composites, Inc. They have a constant circular cross section from the blade root to 5% blade radius (R), and three NREL airfoil profiles (S819, S820, S821) are used at different spanwise locations along the rotor blade. The S821 airfoil profile is used between 0.208R and 0.40R, the S819 primary airfoil is positioned at 0.70R, and the S820 airfoil profile is specified at 0.95R. A spline function is used to interpolate the prescribed cross section profiles to generate the three dimensional model of the rotor blade using SolidWorks software. The rotor blades were then mounted on the turbine hub with a pitch angle of $10.0°$.

c) *The Measurement techniques used in wind tunnel testing:*

The wind turbine power output measurements were achieved by measuring the voltage outputs of the small DC generators installed in the nacelles of the wind turbines at a constant electrical loading of 6Ω. During the experiments, the voltage outputs of each DC generator were acquired through an A/D board plugged into a host computer at a data sampling rate of 1 kHz for three minutes. Furthermore, a Monarch Instrument Tachometer was also used to measure the rotation speed of the wind turbine blades. The tip speed ratio (TSR) of the model wind turbine (i.e., $TSR=(\Omega R)/U_{hub}$, where Ω is the angular speed of rotation in rad/s, R is the radius of the rotor blades, and U_{hub} is the speed of the oncoming wind at the hub height) was ranged between 0 and 3.5.

Aluminum rods were used as the turbine towers to support the turbine nacelles and the rotor blades. Through holes in the wind tunnel floor, the aluminum rods were connected to high-sensitivity force-moment sensors (JR3, model 30E12A-I40) to measure the wind loads (aerodynamic forces and bending moments) acting on the wind turbine models. During the experiments, the wind load data were acquired for 120 seconds at a sampling rate of 1 kHz for each tested case.

The turbulent wake flow characteristics in the plane of symmetry of the wind turbines were measured by using a Cobra Probe Anemometry system (TFI Series 100 of Turbulent Flow Instrumentation Pty LtD). The Cobra Probe Anemometry system is capable of measuring all three components of instantaneous flow velocity vector at a prescribed point at a sampling rate of up to 2 kHz. Other flow quantities such as the turbulence intensity, turbulence kinetic energy, Reynolds stresses and other higher order terms can also be derived based on the instantaneous measurement results. During the experiments, the Cobra Probe Anemometry system was mounted on a rigid steel frame and controlled by a motorized traverse system at the prescribed downstream locations. At each measurement point, the instantaneous flow velocity data were acquired for 60 seconds at a data sampling rate of 1.25 kHz.

5.3 Results and Discussions

As shown in Figure 5-5, two wind turbine models were set to operate in tandem arrangement with X/D=2 spacing. Upstream turbine was placed on a turn-table in order to adjust the alignment of upstream turbine with respect to the oncoming ABL wind. It was given a yaw misalignment up to 50° with an increment of 10° to assess the effects of upstream turbine yaw misalignment on the overall power production from the system (two wind turbine models) as well as on the individual upstream and downstream turbine power productions. Besides, the effects of upstream turbine yaw misalignment on the upstream turbine wind loading and near-wake turbulent flow structures were investigated in this chapter. Moreover, dependency of all those measurements on the oncoming ABL wind turbulence was revealed by simulating offshore and onshore ABL wind conditions (i.e., open terrain I and open terrain II, respectively) in the wind tunnel.
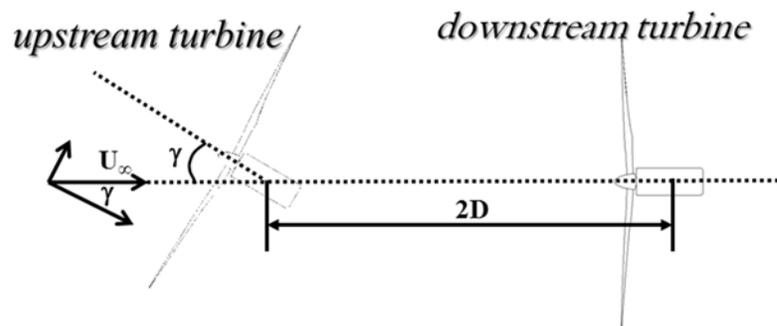
Figure 5-5 Two wind turbine models in tandem arrangement (X/D=2) with yawed upstream turbine

a) *The effect of yawing (yaw error) on the upstream turbine performance:*

The effect of yawing on the upstream turbine power output performance was investigated by aligning the upstream turbine at different orientations (yaw angles) with respect to the oncoming ABL wind. When a turbine has a non-zero yaw angle, as shown in Figure 5-6, the velocity component of the oncoming ABL wind normal to the rotor plane is reduced by the cosine of the yaw angle, which significantly decreases the power available from the oncoming wind as it is a function of the cube of the wind speed. Therefore, power production from a yawed wind turbine could be associated with the $\cos^3$ of the yaw angle. Fingersh et al. (2001) have confirmed the $\cos^3$ approximation with the real data collected from NREL's Unsteady Aerodynamics experiment. The field data collected from a utility scale wind turbine has also shown a good agreement with $\cos^3$ approximation for small yaw angles up to 20° (Mamidipudi et al., 2011). On the contrary, Pedersen et al. (2002) correlated the power variation with $\cos^2$ of the yaw angle by considering the combined effect of projected swept area and wind flow component normal to the rotor plane. Moreover, Johnson (2004) pointed out that wind velocity component parallel to the rotor does also have an effect on the rotor performance and $\cos^3$ approximation is not perfectly accurate. However, it is assumed to be negligibly small since the effect of wind velocity component parallel to the rotor is opposite on the upper and lower half of the rotor regardless of the direction of rotation, and tend to cancel out each other.
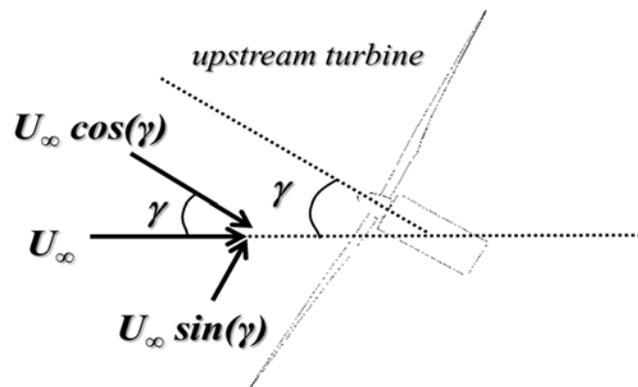
Figure 5-6 Upstream HAWT model with yaw misalignment γ (top view)

Figure 5-7 plots the reduction in the wind turbine power generation for varying upstream turbine yaw angle up to 50° with an increment of 10° for different terrains (i.e., open terrain I and open terrain II) simulated in the wind tunnel. It has been found out that $\cos^3$ approximation

is the best fit for the power variation with the yaw angle. However, the assumption of $\cos^2$ relationship could be optimistic at greater yaw angles ($\gamma >20°$).
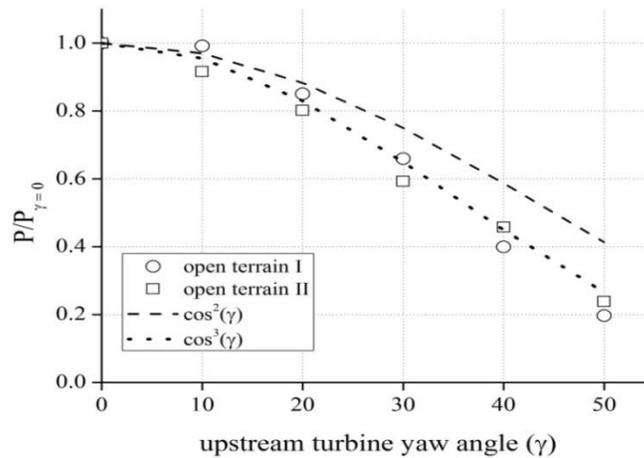
Figure 5-7 Relative power output reduction from the upstream wind turbine with varying upstream turbine yaw angle for open terrain I and II

Furthermore, no significant difference was observed between open terrain I and open terrain II, as shown in Figure 5-7. Thus, it was concluded that oncoming flow characteristics do not play a crucial role on the power variation with the yaw angle, and the power losses could go up to 80% at a yaw angle of $\gamma=50°$ regardless of the terrain characteristics.

Figure 5-8 shows the change in the tip speed ratio (TSR) of the turbine (normalized with the tip speed ratio of non-yawed turbine) as a function of the yaw angle. It was found out that the tip speed ratio varies with $\cos^2$ of the yaw angle. Tip speed ratio of the wind turbine was varied between 3.5 (i.e., in case of a zero yaw angle, $\gamma=0°$) and 1.7 (i.e., in case of a maximum yaw angle, $\gamma=50°$). It was also observed in Figure 5-8 that oncoming flow characteristics do not have a substantial influence on the tip speed variation with the yaw angle similar to the power variation case.
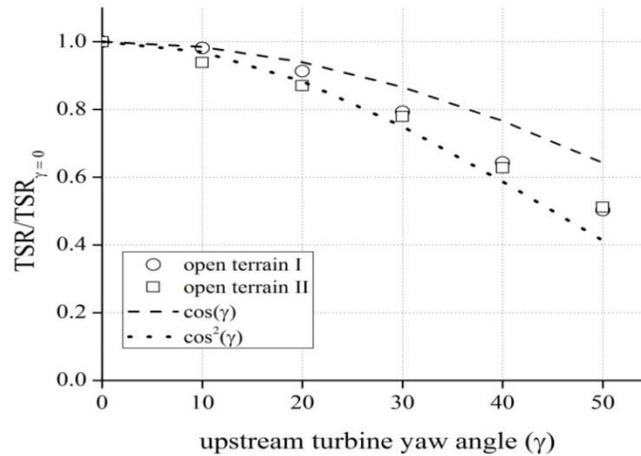
Figure 5-8 Relative Tip Speed Ratio (TSR) reduction from the upstream wind turbine with varying upstream turbine yaw angle for open terrain I and II

Wind loading characteristics of the upstream wind turbine were also investigated for different yaw angles of the upstream turbine. Thrust loading on a turbine is dependent on the oncoming wind velocity and it is proportional to the square of the wind velocity. As yaw angle increases, wind velocity component normal to the rotor plane is reduced by the cosine of the yaw angle, and the variation in wind thrust loading (normalized with the wind thrust loading of non-yawed turbine) was found out to be nearly proportional to the $\cos^2$ of the yaw angle, as shown in Figure 5-9. However, for greater yaw angles (γ>30), $\cos^2$ approximation tends to give more conservative results in comparison to the wind tunnel measurements. On the contrary, cos approximation would be optimistic for wind thrust loading variation with the turbine yaw angle. Moreover, wind thrust loading variation with the turbine yaw angle was also found out to be independent of the oncoming flow characteristics.
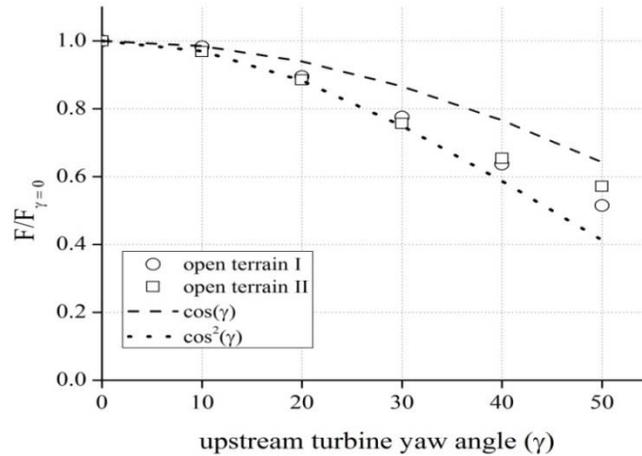
Figure 5-9 Relative wind (thrust) loading reduction from the upstream wind turbine with varying upstream turbine yaw angle for open terrain I and II

b) Near wake characteristics behind the yawed upstream turbine:

Near wake flow field measurements were conducted in order to reveal the turbulent wake flow structures, including the traces of helical tip vortices and the size of the velocity deficit. The effects of the oncoming flow characteristics and upstream turbine yaw misalignment on the near wake flow structure were also investigated during the flow field measurements.

(a) Open terrain I   **(b) Open terrain II**
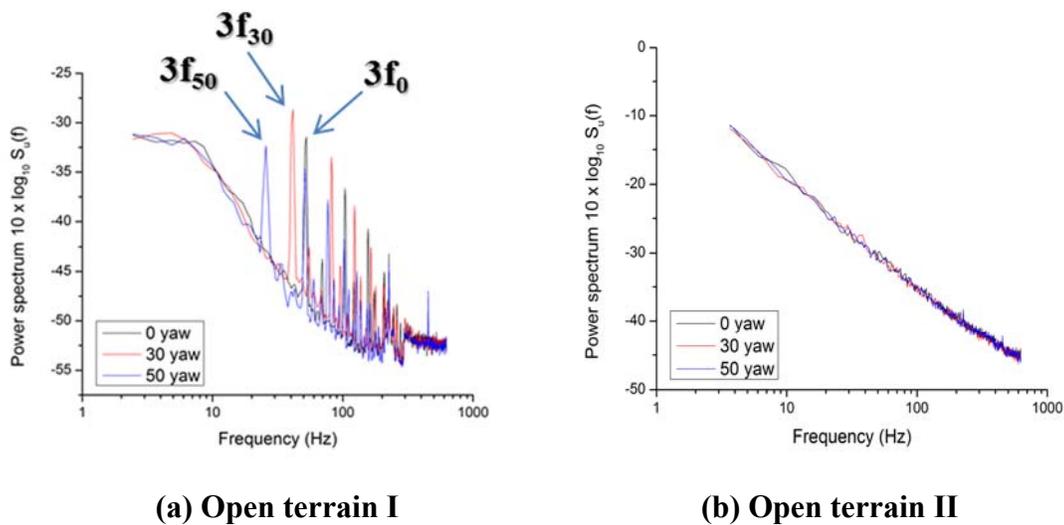
Figure 5-10 Power spectrum of the streamwise velocity at the top-tip level of the upstream wind turbine model at X/D=0.2 for different yaw angles of upstream turbine

Figure 5-10 exhibits the power spectra of the streamwise velocity at the top tip height, X/D=0.2 downstream of the upstream turbine. The primary shedding frequency of the helical tip vortices (3f), which is associated with the rotational frequency of the rotor (f, where subscripts 0, 30 and 50 denotes the yaw angles of the upstream turbine), was clearly observed in open terrain I due to the relatively low levels of turbulence generated in that terrain. Moreover, the peak frequency values, corresponding to the primary shedding frequency of tip vortices, in the power spectra shifts left as the yaw angle of the upstream turbine increases for open terrain I, thereby indicating a decrease in the rotational frequency of the rotor and in the shedding frequency of the vortices as well. Therefore, the power output performance of the upstream turbine decreases with increasing yaw angle as mentioned before, and the strength of tip vortices decreases with the yaw angle as well, mitigating the wake effects behind the yawed turbine.

As also shown in Figure 5-10, no frequency peaks were detected in the power spectra for open terrain II due to the quick break down of the tip vortices. The shedding tip vortices could dissipate quickly under the influence of relatively high turbulence level in open terrain II. The enhanced turbulent mixing rate also diminishes the effect of yaw angle on the power spectra, making it almost impossible to identify the shedding frequency of tip vortices.

(a) Open terrain I   **(b) Open terrain II**
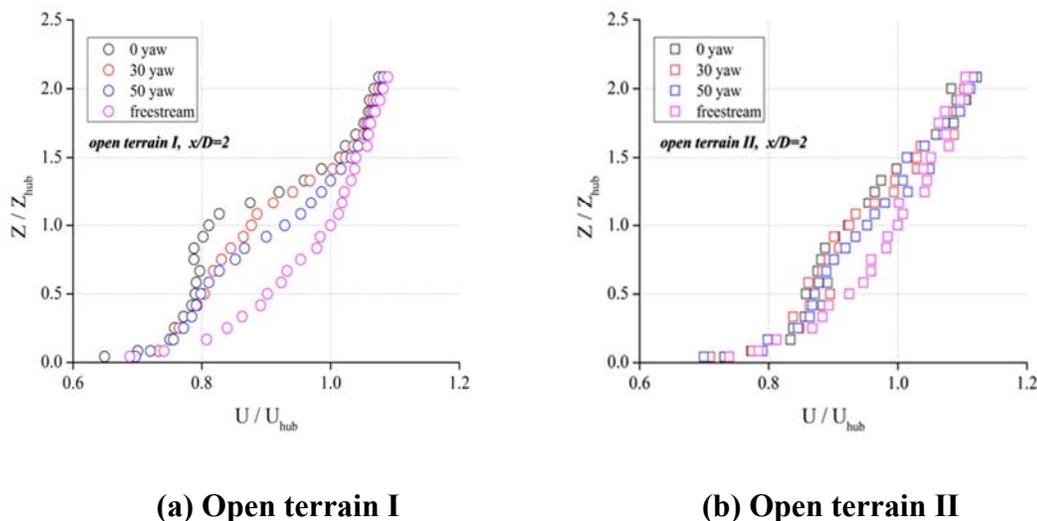
Figure 5-11 Measured mean flow streamwise velocity profiles at X/D=2.0 for different yaw angles of upstream turbine

Figure 5-11 shows the vertical profiles of the measured mean flow streamwise velocities, X/D=2 downstream of the upstream turbine at various yaw angles of the upstream turbine for open terrain I and open terrain II. As the yaw angle of the upstream turbine increases, velocity deficit in the wake was found to mitigate due to the decrease in the power output performance of the upstream turbine and the wake deflection. The reduction in the wake deficit with the yaw angle is more pronounced for open terrain I since low turbulence level in open terrain I do not contribute much to the wake recovery. However, relatively higher turbulence level in open terrain II triggers the turbulent mixing mechanism in the wake so that wake recovers much faster. Thus, changing the yaw angle of the upstream turbine in open terrain II does not provide as higher wake deficit reduction as in open terrain I.

c) *The effect of yawing on the overall power output performance:*

Changing the operating conditions of the upstream turbine by adjusting the yaw angle of the upstream turbine can be used to increase the overall efficiency of wind farms (Adaramola & Krogstad, 2011). However, this can be achieved only by operating the upstream turbine at an appropriate yaw angle so that the power gained from downstream turbines could be greater than the power loss from yawed upstream turbines.

Figure 5-12 illustrates that by increasing the yaw angle of the upstream turbine, there is a corresponding increase in the performance of the downstream turbine at X/D=2. This is due to the fact that downstream turbine is no longer under the direct effect of the upstream turbine wake so that downstream turbine experiences comparably higher velocities and generate more power. It can also be inferred from Figure 5-12 that oncoming flow character is also an important factor on the downstream turbine power generation. For a non-yawed upstream turbine ($\gamma=0°$), downstream turbine generates around 15% more energy at open terrain II in comparison to its energy generation at open terrain I due to the contribution of higher turbulence on the wake recovery. Furthermore, even at an upstream yaw angle of $\gamma=50°$, the downstream turbine power loss is still around 15% for the open terrain I case. This could be explained with the shadowing effect from the upstream turbine and the low turbulence level in open terrain I.
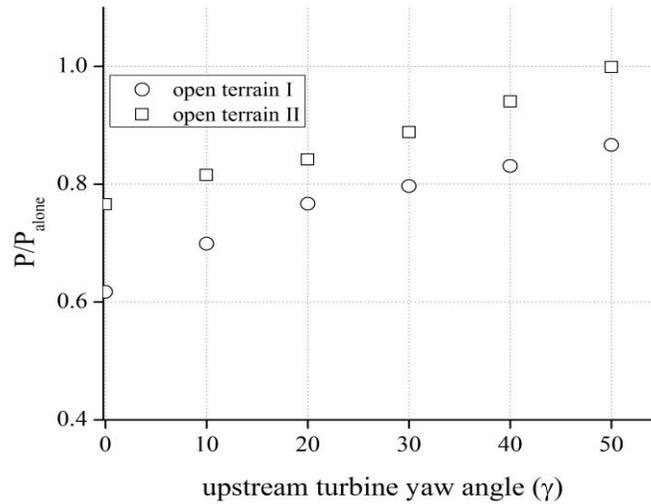
Figure 5-12 Relative power output from the downstream turbine at X/D=2 with varying upstream turbine yaw angle for open terrain I and II

Wind farm efficiency (from two turbines in tandem arrangement with X/D=2 spacing) was calculated at different yaw angles of upstream turbine for open terrain I and open terrain II cases. The wind farm efficiency was calculated by the ratio of total power output from the upstream and downstream turbines in the wind farm to the sum of their individual power outputs without any wake losses.

It can be inferred from Figure 5-13 that oncoming flow characteristics could have a major effect on the yaw angle optimization. It was found out that wake recovers faster with higher level of oncoming flow turbulence, as in open terrain II case, thereby increasing the overall wind farm efficiency. However, interestingly upstream turbine yaw angle optimization in open terrain II was found to degrade the wind farm efficiency.

Figure 5-13 also shows that for relatively lower level of oncoming flow turbulence, as in open terrain I case, wind farm efficiency can be improved up to 6% by operating the upstream turbine at an appropriate yaw angle of $\gamma=10°$. This enhancement in the efficiency could be much less in larger wind farms with clusters of wind turbines; however, as stated by Barthelmie & Jensen (2010), even 1% increase in the overall power output of a 100 MW wind farm is equivalent to approximately $0.5 million increase in annual revenue. Moreover, wind turbines

will be installed with relatively small separation distances, thereby reducing the space requirement (Adaramola & Krogstad, 2011) and increasing the wind farm power density.

This chapter suggests that upstream turbine yaw optimization can be used efficiently for offshore (considerably lower turbulence level compared to the onshore) wind farm applications. This also allows for smaller spacing between wind turbines in offshore wind farms where wake effects persist for longer distances.
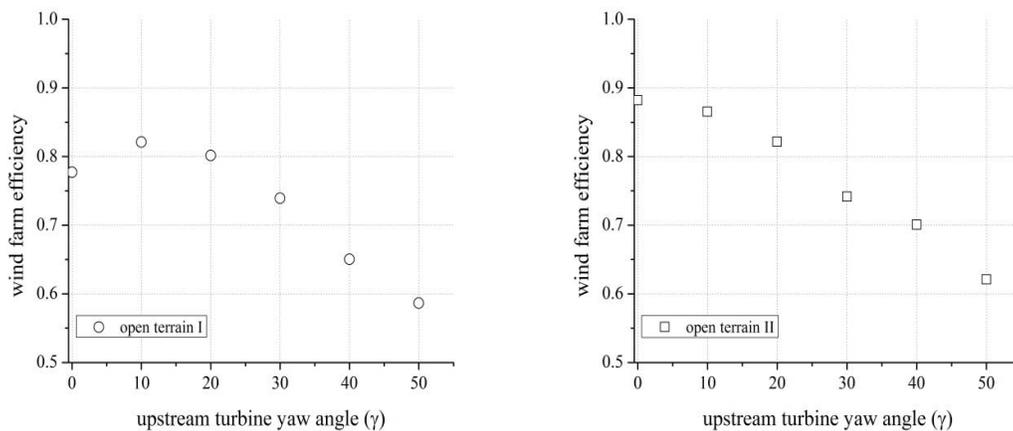
Figure 5-13 Wind farm efficiency (two turbines in tandem arrangement with X/D=2 spacing) with varying upstream turbine yaw angle for open terrain I and II

5.4 Conclusion

The experimental results showed that by operating the upstream turbine at an appropriate yaw angle, the performance of the downstream turbine can be improved since yawing the upstream turbine deflects the upstream turbine wake sideways so that downstream turbine experiences considerably higher wind speeds and no longer suffers from the severe effects of the upstream wake. Although increasing the yaw angle of the upstream turbine increases the power output performance of the downstream turbine, a corresponding decrease occurs in the performance of the upstream turbine. Thus, upstream turbine should operate at an appropriate yaw angle in order to increase the overall power output from two turbines.

In this study, the effectiveness of yaw angle control for wind farm optimization was quantified and it was found to be strongly dependent on the turbulence intensity levels of the oncoming wind. The wind farm efficiency in open terrain I (i.e., simulating offshore conditions with low turbulence level) could be improved up to 5% at an upstream turbine yaw angle of

$α=10˚$ with 2D spacing between the turbines. However, although higher turbulence levels in open terrain II (i.e., simulating onshore conditions) increases the overall wind farm efficiency, yawing the upstream turbine was found to have a negative impact on the overall efficiency of the wind farm.

Future research plan involves simulating a wind farm with more rows of wind turbines and investigate how the strategy of operating the upstream turbines in the first row at an appropriate yaw angle (e.g. at $α=10˚$) will affect the performance of the turbines in the downstream rows and wind farm efficiency as well.

CHAPTER 6. EXPERIMENTAL INVESTIGATION ON THE AEROMECHANICS AND NEAR WAKE CHARACTERISTICS OF DUAL-ROTOR WIND TURBINES (DRWTs)

6.1 Introduction

Wind energy, as a promising inexhaustible energy source, has been playing a crucial role in the worldwide energy production throughout the recent years. Efficient use of wind energy will provide eco-friendly solutions for energy production thereby alleviating dependence on hydrocarbons and reducing CO_2 emissions. Although only approximately 4% of U.S. electricity is derived from the wind itself, installed wind power capacity is growing rapidly. According to the U.S. Department of Energy (DOE), wind could feasibly provide 20% of the U.S. electricity by 2030. This goal can be achieved by increasing the installed wind capacity onshore and offshore. This necessitates the installation of wind turbines in large arrays (farms).

Today, Horizontal Axis Wind Turbines (HAWTs) are the predominant turbine design, due to its simplicity, reliability and durability, used in modern wind farms, and the majority of them are single-rotor wind turbines (SRWT). Although SRWTs come in a variety of sizes depending on the type of application (+90 meters in diameter for commercial turbines, installed onshore or offshore, with a capacity ranging from 1.5 - 3.5 MW), the maximum energy conversion efficiency for a conventional SRWT does not go beyond the Betz limit which is around 59%. However, in practice, today's best aerodynamically designed modern SRWT systems can extract up to (only) 50% of the energy available in the wind. Thus, almost 50% (half) of the energy available in the wind escapes without being harnessed. Therefore, dual-rotor wind turbine (DRWT) concept has been suggested to increase the overall power production from the system.

DRWT systems have two rotors installed in a back-to-back configuration. Thus, the second (downwind) rotor can exploit the unharnessed energy in the near wake of the upwind rotor, thereby increasing the energy harnessing capability of the system. As two rotors are installed very close to each other, counter-rotating concept (rotors rotate at opposite directions) is implemented for DRWT systems due to the fact that downwind rotor could benefit from the disturbed flow (with significant tangential velocity component, swirl) in the upwind rotor wake. Therefore, the downwind rotor could harvest the additional kinetic energy associated

with the swirl component in the wake flow. This concept is also widely used in marine (propellers) and aerospace (helicopter rotors) applications in order to increase the efficiency.

There have been a number of numerical and experimental studies, showing significant increase in the energy yield of DRWT systems in comparison to that of SRWT systems. A prototype of 6 kW DRWT was built in California and completed field testing in 2002 (Appa, 2002). The results indicated that DRWT system could extract 30% more power from the same wind stream, compared with a conventional SRWT design. Another study of the field measurements on a 30 kW prototype DRWT also showed that the power increase of the DRWT system reached about 21% over a conventional SRWT system at a rated wind speed of 10.6 m/s (Jung et al., 2005). More recently, a wind tunnel study with a small-scale DRWT system was conducted by Habash et.al. (2011), and they found out that the DRWT system could produce up to 60% more energy than a SRWT system of the same type and was capable to reduce cut-in speed while maintaining turbine performance. Furthermore, Shen et al. (2007) carried out a numerical study on the performance of DRWTs, and the results indicated that DRWT systems could produce an increase around 43.5% in the Annual Energy Production (AEP) at higher wind speeds when compared to the SRWT systems. It was also noted that the effect of spacing between the rotors on the power and wind loading fluctuations was significantly larger than its effect on the mean power and thrust coefficient.

This chapter presents a comprehensive experimental study which was carried out in a large-scale Aerodynamics/Atmospheric Boundary Layer (AABL) Wind Tunnel located at the Aerospace Engineering Department of Iowa State University. The purpose of this study was to assess the effects of adding an extra (downwind) rotor with counter-rotating (rotors rotate at opposite directions) and co-rotating (rotors rotate at same direction) concepts on the power production performance of the individual rotors of the system, overall DRWT system performance and the wind loads (both static and dynamic) acting on the system as well, and these results were compared to those of a traditional SRWT system.

This chapter further discusses the near wake turbulent flow structure characteristics of DRWT systems in order to illustrate their differences from conventional SRWT systems. Therefore, wind-tunnel experiments were carried out using intrusive (point-wise) and non-

intrusive (PIV) measurement techniques in order to characterize the near wake turbulent flow structures in a neutral boundary layer flow.

6.2 Experimental Set-up and Procedure

a) AABL Wind Tunnel:

Figure 6-1 The test section of the AABL wind tunnel

The present experimental study was performed in the Aerodynamic/Atmospheric Boundary Layer (AABL) Wind Tunnel located at the Aerospace Engineering Department of Iowa State University. The AABL wind tunnel, as shown in Figure 6-1, is a closed-circuit wind tunnel with a test section of 20 m long, 2.4 m wide and 2.3 m high, optically transparent side walls, and a capacity of generating a maximum wind speed of 45 m/s in the test section. Spike structures, chains and/or arrays of wood blocks were placed on the wind tunnel floor upstream of the test section in order to generate a turbulent boundary layer flow analogous to a typical atmospheric boundary layer (ABL) wind seen in wind farms. The boundary layer growth of the simulated ABL wind under zero pressure gradient condition was achieved by adjusting the ceiling profile of the test section of the wind tunnel.
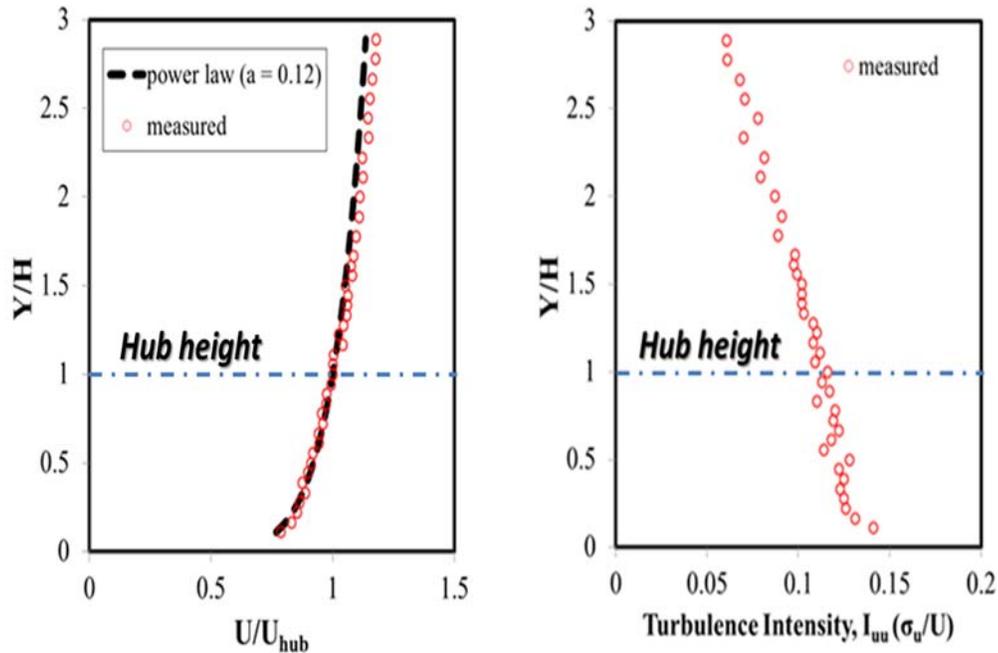
Figure 6-2 Atmospheric boundary layer wind profiles

The oncoming boundary layer wind velocity profile was fitted by using power law equation, i.e., $U(y) = U_{YG}{}^{*} (Y/Y_G)^a$, where U_{YG} is the wind speed at a reference (hub) height of Y_G, and the value of power law exponent 'a' is associated with the terrain roughness. Figure 6-2 shows the measured streamwise mean velocity (normalized with the hub height velocity, U_{hub}) and turbulence intensity (the ratio of standard deviation in velocity fluctuations, σ_u, to the mean flow velocity, U) profiles of the oncoming flow in the test section for the present study. As shown in Figure 6-2, the power law exponent of the curve fitting to the measurement data was found to be a = 0.12, corresponding to the offshore boundary layer wind profile according to the ISO offshore standard (a=1/8.4), with the measured hub height turbulence intensity around 0.12. GL (Germanischer Lloyd) regulations define a turbulence intensity of 0.12 at the hub height of offshore wind turbines; however, it was found out to be very conservative compared to field measurements. Typical hub height turbulence intensity for offshore wind turbines is around 0.08, indicated by Tong (2002) in 'Wind Power Generation and Wind Turbine Design'.

b) Wind Turbine Models:

The dual-rotor wind turbine (DRWT) models used for the present study was modified from conventional three-bladed horizontal axis wind turbine models by adding a second set of blades downwind. Figure 6-3 shows a schematic of the DRWT model along with a 3-D printed (blades, nacelle and hub) model installed on the floor of the test section. All the wind turbine models used in the present study have the same rotor radius of 140 mm and hub height of 226 mm. With the scale ratio of 1:350, the DRWT models would represent large-scale conventional 2 MW horizontal axis single rotor wind turbines (SRWTs) modified to have a second rotor installed 63.5 mm (corresponding *1/4.4* of the rotor diameter) behind the upwind rotor with a back-to-back configuration. It should be noted that the blockage ratio of the wind turbine models (i.e., the ratio of the turbine blade swept area to the cross-section area of the AABL tunnel) was found to be less than 2%. Thus, the blockage effects of the wind turbine models in the test section would be almost negligible for the present study.
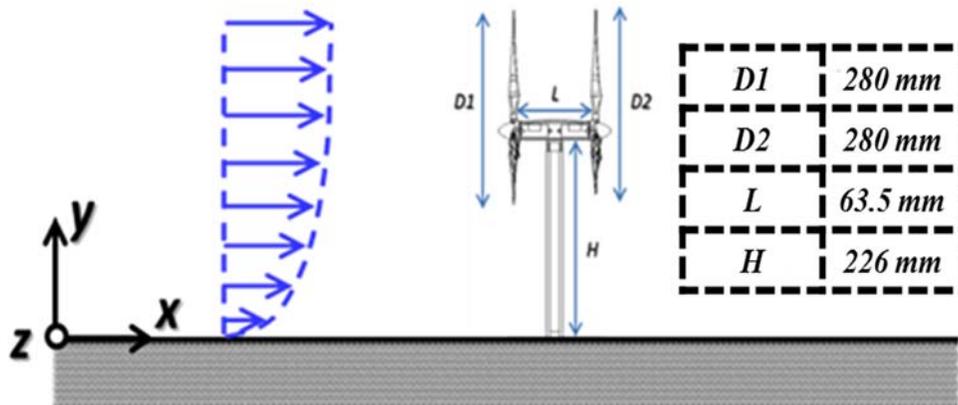
Figure 6-3 The tested DRWT system, schematics and design parameters

The rotor blades of the model wind turbines used in the present study are made of a hard plastic material by using a rapid prototyping machine. The rotor blades have the same airfoil cross sections and platform profiles as ERS-100 prototype turbine blades developed by TPI Composites, Inc. The rotor blade has a constant circular cross section from the blade root to 5% blade radius (R), and three NREL airfoil profiles (S819, S820, S821) are used at different spanwise locations along the rotor blade. The S821 airfoil profile is used between 0.208R and 0.40R, the S819 primary airfoil is positioned at 0.70R, and the S820 airfoil profile is specified

at 0.95R. The downwind rotor blades of DRWT in counter-rotating configuration were modified accordingly using SolidWorks software. In the present study, the rotor blades were mounted on the turbine hub with a pitch angle of 3.0 degrees. Two DC electricity generators (Kysan, FF-050S-07330) were installed (back-to-back configuration) inside the nacelle of the DRWT model, which would produce electricity as driven by the rotating blades. Furthermore, hollow aluminum rods were used for the turbine towers through which the wires associated with the power measurement system travel.

During the experiments, wind tunnel operated at a constant frequency of 5.5 Hz, which provided a freestream velocity of 5.9 m/s. The corresponding chord Reynolds number (i.e., based on the averaged chord length of the rotor blades and the wind speed at the hub height) was found to be significantly lower ($Re_c < 7000$) than those of the large-scale wind turbines in wind farms, causing much lower power coefficient values for the models tested in the wind tunnel. In addition, electrical power output performance of model turbines could be significantly reduced due to copper, magnetic and mechanical losses (Kang and Meneveau, 2010). On the contrary, Whale et al. (2000) surprisingly observed similar wake characteristics for a wide range of Reynolds number although the boundary layer over the blades and the shed vorticity is known to be highly sensitive to Reynolds number. This could be explained with an inviscid wake generated behind a wind turbine even at smaller scales. Moreover, different tip speed ratios (TSR) were achieved by operating the rotor at different speeds in a constant freestream.

c) Measurement Systems:

The turbine power output measurements were achieved by measuring the voltage outputs of the small DC generators installed in the nacelles of the wind turbines and the corresponding electrical loadings applied to the electric circuits. During the experiments, the voltage outputs of each DC generator were acquired through an A/D board plugged into a host computer at a data sampling rate of 1 kHz for two minutes. The normalized power output of the model wind turbines (i.e., normalized by the maximum power output of the upwind or downwind rotor for SRWT and DRWT systems) were used in the present study for better comparison reasons.

For the wind turbine models used in the present study, aluminum rods were used as the turbine towers to support the turbine nacelles and the rotor blades. Through holes in the wind

tunnel floor, the aluminum rods were connected to high-sensitivity force-moment sensors (JR3, model 30E12A-I40) to measure the wind loads (aerodynamic forces and bending moments) acting on the wind turbine models. The precision of the force-moment sensor cell for force measurements is ±0.25% of the full range (40N). The axial (thrust) loads acting on the tested wind turbine models had a range of 0.3N to 0.5N during the experiments. While the force-moment sensor mounted at the bottom of each turbine tower can provide time-resolved measurements of all three components of the aerodynamic forces and the moment (torque) about each axis, only the measured thrust coefficient, C_{Fx}, and bending moment coefficient, C_{Mz}, are given in the present study. The axial thrust and associated bending moment coefficients were defined by using the expressions $F_x / (0.5\rho U^2\pi R^2)$ and $M_z / (0.5\rho U^2\pi R^2 H)$ respectively, where ρ is the air density; U is the mean flow velocity at the hub height H. The wind load data were acquired for five minutes at a sampling rate of 1,000 Hz for each tested case. A Monarch Instrument Tachometer was also used to measure the rotation speed of the wind turbine blades.

d) Measurement Techniques:

PIV measurements: Particle Image Velocimetry (PIV) technique was used to obtain detailed flow field measurements in the near wake (X/D<2.5) of DRWT and SRWT systems in order to assess the turbulent near wake flow structure characteristics. Figure 6-4 shows the PIV experimental set-up installed in the AABL wind tunnel. The seeded particles (oil droplets from smoke generator) in the airflow were illuminated by a double-pulsed Nd:YAG laser on a Y/D=0 plane. The thickness of the laser sheet in the measurement regions was about 1.5 mm, and two CCD cameras were used to capture the PIV images on the two measurement regions with an overlapping region of 13 mm length. The CCD cameras and the double-pulsed Nd:YAG laser were connected to a host computer via a digital delay generator so that the timing between laser illumination and image acquisition was adjusted.
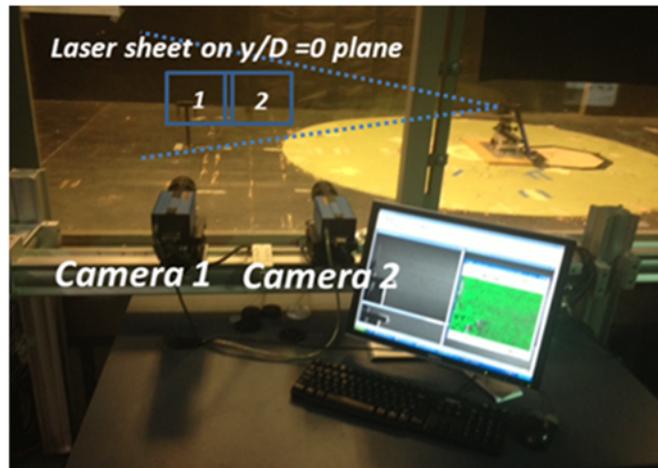
Figure 6-4 Experimental set-up for PIV system

After image acquisition, instantaneous PIV velocity vectors were obtained by frame to frame cross-correlation. An interrogation window of 32*32 pixels was employed for each successive frame patterns of PIV images with an effective overlap of 50%. Then, the ensemble averaged flow quantities such as normalized velocity (U/U_{hub}), normalized Reynolds stress (R_{uv}/U^2_{hub}), where $R_{uv} = - u'v'$, and normalized Turbulence Kinetic Energy (TKE/U^2_{hub}), where $TKE=0.5(u'^2+v'^2)$, were obtained from approximately 1000 frames of instantaneous PIV measurements.

In the present study, both "free-run" and "phase-locked" PIV measurements were performed during the experiments. Free-run PIV measurements were conducted in order to determine the ensemble averaged flow characteristics (mean Velocity, Reynolds stress and TKE) in the near wake of the wind turbine models. However, phase-locked PIV measurements were conducted to investigate the evolution of unsteady vortex structures in the near wake. For phase-locked measurements, a digital tachometer was used to detect the position of a pre-marked blade so that tachometer generated pulsed signal was used to trigger the PIV system via a digital delay generator. Therefore, different rotation phase angles of pre-marked rotor blade can be achieved by changing the time delay between the input signal from the tachometer and the signal output from the digital delay generator. For each pre-selected phase angle, 345 frames of instantaneous PIV measurements were used to calculate the phase-averaged velocity, vorticity (w_z) and swirling strength (λ_{ci}) distributions.

Point-wise measurements with a cobra probe: A Cobra Probe Anemometry system was used to measure all three components of instantaneous flow velocity at different measurement points with the help of a motorized traverse system. Other flow quantities such as the turbulence intensity, Reynolds stresses and other higher order terms can also be derived based on the instantaneous measurement results. At each measurement point, data were acquired for 30 seconds at a data sampling rate of 2.5 kHz.

e) Experimental Procedure:
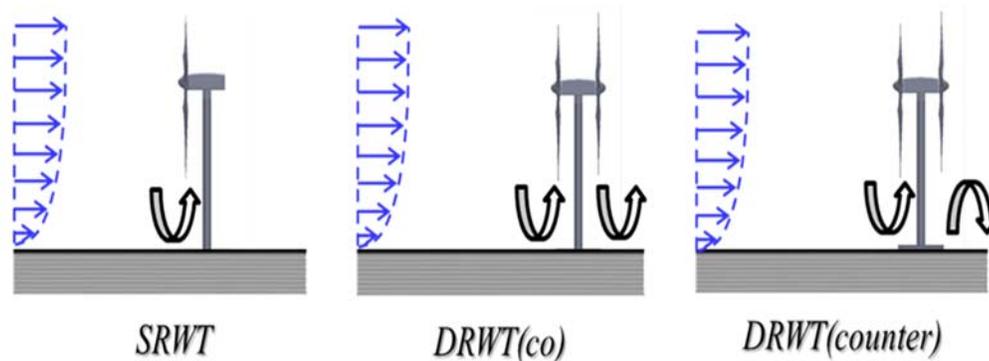
Figure 6-5 Tested wind turbine (SRWT and DRWTs) models

In the present study, three different wind turbine model configurations (SRWT, DRWT with co- and counter- rotating concept, see Figure 6-5) were investigated and compared in terms of their power output performances, static and dynamic wind loads acting on them, and the near wake $(X/D<2.5)$ turbulent flow structure characteristics. Furthermore, the effects of rotor-rotor interactions on the individual rotor power output performances as well as on the overall power output performances of both (co- and counter-rotating) DRWT systems were studied in detail.

6.3 Results and Discussions

a) Power output performance measurements:

As described before, DRWT systems can extract more energy from the oncoming wind due to the addition of a second (downwind) rotor when compared to the SRWT systems. During the experiments, DRWT systems were set to operate in co- and counter-rotating configurations depending on the rotational direction of the downwind rotor. The experimental

results associated with both DRWT systems were then compared to those of SRWT system. In the comparison of the power output performances, power output readings were normalized with the maximum power output, which corresponds to an (optimum) electric loading range of 28Ω - 29Ω. Figure 6-6 shows the change in the normalized (by the maximum power output of the SRWT system) power outputs of SRWT and DRWT systems under different electric loading conditions.
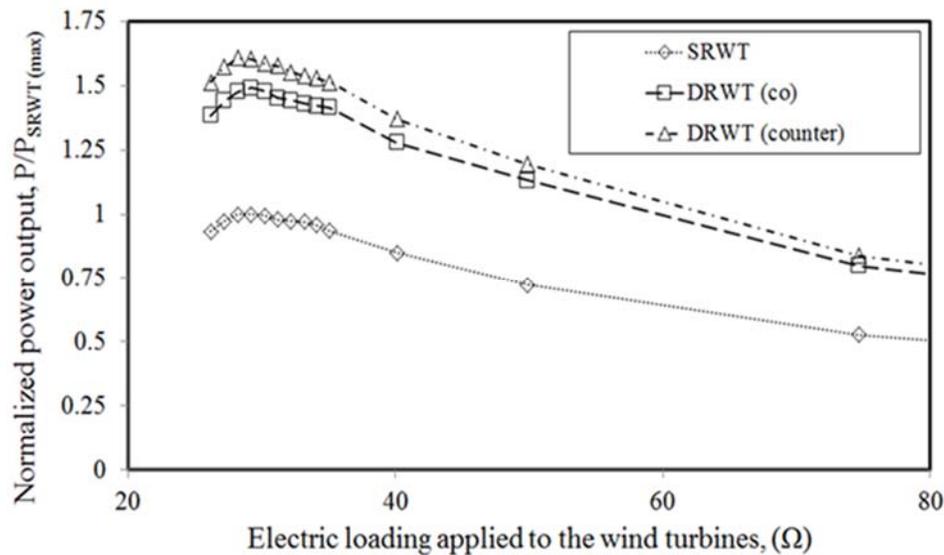
Figure 6-6 Measured overall power outputs (normalized with the maximum power output of the SRWT system) of SRWT and co- and counter- DRWT systems as a function of the applied electric loads

As shown in Figure 6-6, within the entire electrical loading range, DRWT systems were found to generate at least 47% more power than the SRWT system regardless of the rotational direction of the downwind rotor. When downwind rotor rotation direction is taken into account, DRWT system with counter-rotating configuration could generate up to 60% more power; however, DRWT system with co-rotating configuration could only generate up to 48% more power for an optimum electric loading value of 28.2Ω. Furthermore, the effects of the rotational direction of downwind (back) rotor on the power output performance of downwind (back) rotor and on that of overall DRWT system were also investigated. Thus, the ratios of power outputs ($P_{counter-rotating}/P_{co-rotating}$) were calculated for DRWT systems under varying electrical loads, as shown in Figure 6-7. It reveals the advantage of counter-rotating

configuration over co-rotating configuration for DRWT systems. While the maximum gain from the counter-rotating case could be as high as 23% for the downwind rotor itself, the overall DRWT system was found to generate up to 9% more power than the co-rotating case.
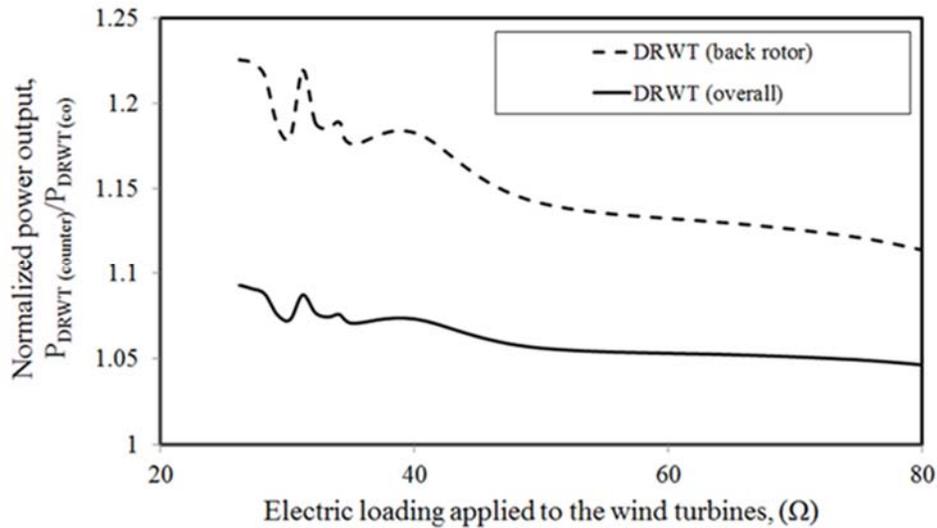
Figure 6-7 The ratios of the downwind (back) rotor and overall power outputs of counter-rotating DRWT system to those of co-rotating DRWT system as a function of the applied electric loads
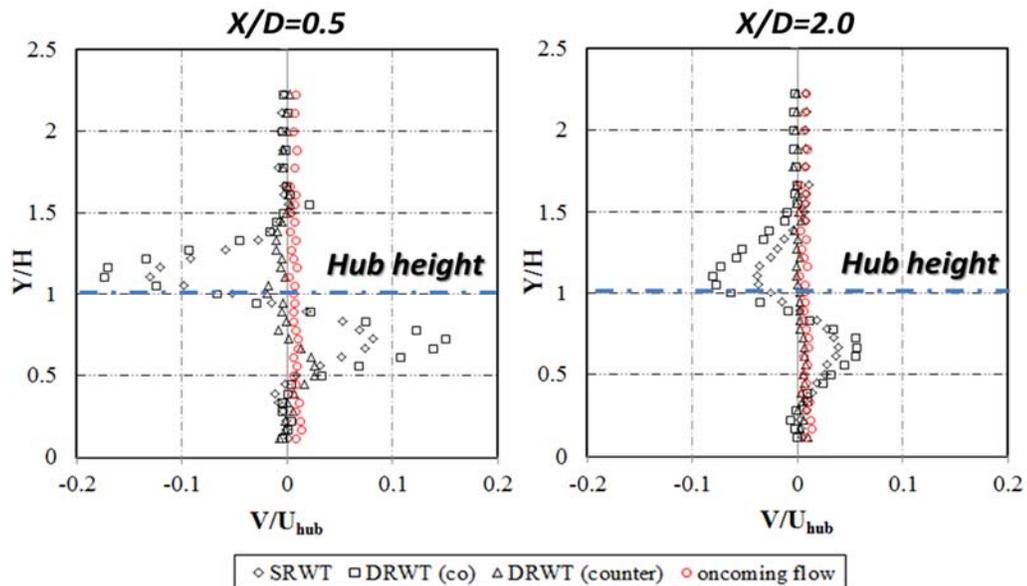
Figure 6-8 The measured (cobra probe) azimuthal (swirl) velocity profiles in the wake flows of SRWT and DRWT systems at X/D=0.5 and X/D=2.0

The counter-rotating concept suggested for DRWT systems is analogous to the contra-rotating propellers used for marine and aerospace applications. The idea behind that concept is to take advantage of the significant swirl velocity (tangential or azimuthal) component generated in the wake of a rotating component (rotor). Thus, a second rotor installed in the near wake of an upwind one could harness the energy available in the swirl (tangential) flow when rotors rotate at opposite directions. This is due to the fact that the wake induced by the upwind rotor rotates in the same direction as the downwind rotor, thereby providing additional torque associated with the kinetic energy of the swirl flow. Figure 6-8 illustrates the measured azimuthal (swirl) velocity profiles in the wake flows of SRWT and DRWT systems at different near wake locations. The magnitude of the swirl velocity component was found to be amplified in the wake flow of co-rotating DRWT system; however, it was observed to be very small (similar to the oncoming flow) for the wake flow of counter-rotating DRWT system. This significant difference in the evolution characteristics of the swirl velocity reveals the fact that counter-rotating DRWT systems could harness the additional kinetic energy associated with the swirl velocity component in the wake. It was also observed that wake induced swirl velocity component tends to vanish for SRWT and co-rotating DRWT systems as the downstream distance increases.
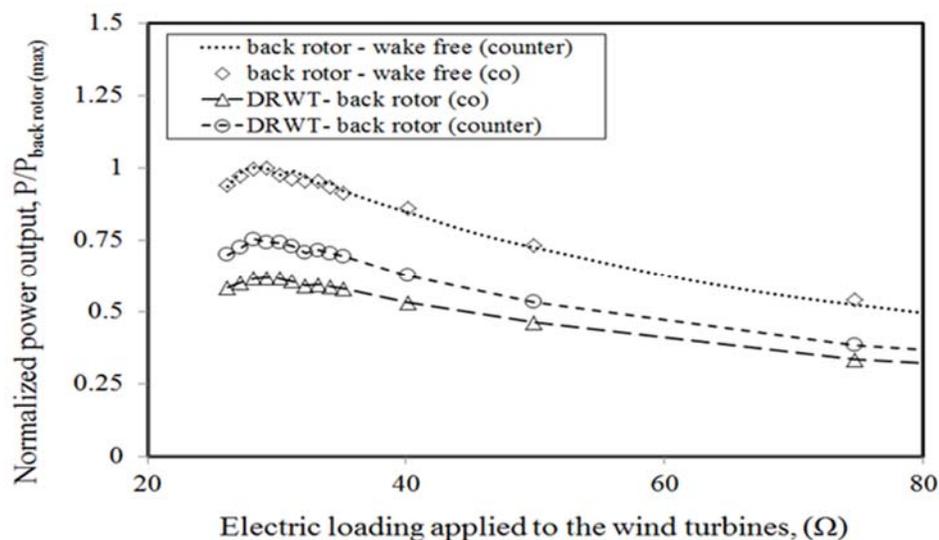
Figure 6-9 Measured power outputs of downwind (back) rotor (normalized with its wake free - maximum power output) for co- and counter- DRWT systems as a function of the applied electric loads

The measurement results highlighted the advantage of DRWT systems over SRWT systems. This advantage was found to be enhanced with the counter-rotating configuration. However, although DRWT systems operate with two rotors, the gain over SRWT systems in terms of power generation is not unity (unity corresponds to the twice as much energy generation compared to the SRWT system). The maximum power gain does not even go beyond 63%. Significant power losses (up to 40%) were observed due to the rotor-rotor interactions in DRWT systems. These rotor-rotor interactions are dominant for DRWT systems due to very close spacing of the rotors. The fact that downwind (back) rotor is located in the near wake of the upwind one makes it vulnerable to severe power losses associated with the higher velocity deficits in the wake flow. Figure 6-9 shows the effect of upwind rotor on the power output performance of the downwind rotor for co- and counter-rotating DRWT systems. Power output readings were normalized with the peak power output condition (i.e., the optimum electric loading being 28.2Ω) of the downwind rotor. The power production from the downwind rotor itself (in the absence of the upwind rotor - wake free) was found out to be almost independent of the rotational direction of the downwind rotor. This provides for an accurate comparison for the upwind rotor effects on the co- and counter-rotating downwind rotor. As shown in Figure 6-9, power losses for downwind rotor could be as high as 40% for the co-rotating case at the peak power output condition; however, for the counter-rotating downwind rotor, power losses is around 25% at the same conditions.

The presence of the downwind rotor in the near wake of the upwind one was also found to affect the power output performance of the upwind rotor; however, this effect was not as significant as the effect of the upwind rotor on the downwind one, as shown in Figure 6-10. It reveals the fact that upwind (front) rotor power losses are almost independent of the rotational direction of the downwind rotor, and it is around 11% at the peak power output condition.

Therefore, in the light of measurement results, power losses due to rotor-rotor interactions are strongly dominated by the effect of upwind rotor on the downwind one. Moreover, these losses for a DRWT system was found to be mitigated for the counter-rotating case which is consistent with the previous overall power output performance results.
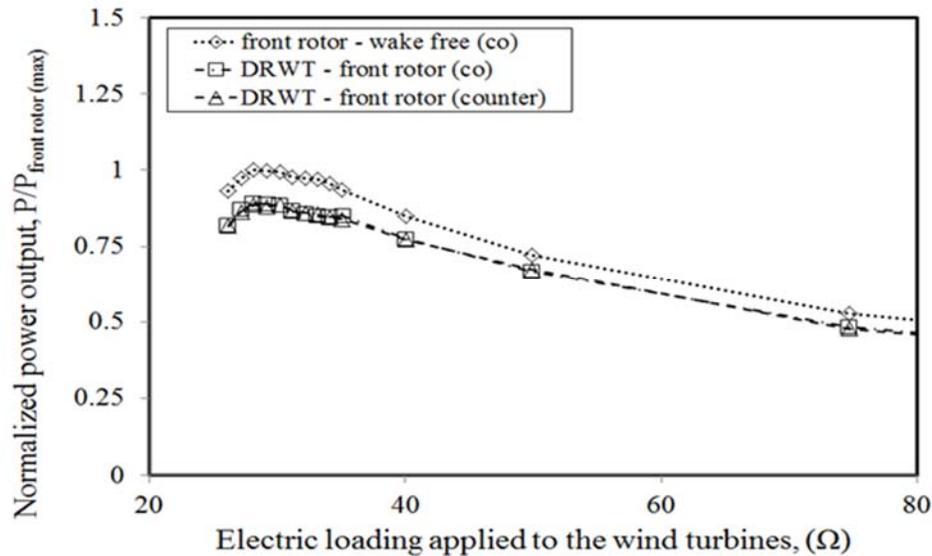
Figure 6-10 Measured power outputs of upwind (front) rotor (normalized with its wake free - maximum power output) for co- and counter- DRWT systems as a function of the applied electric loads

b) Wind loading measurements:

Wind loads on a wind turbine are crucial in term of the lifetime of the system, and it is also indicative of power output performance of the system due to the fact that both strongly depend on the oncoming boundary layer flow velocity. The most essential wind loads, static or dynamic, acting on a turbine system is associated with the streamwise mean and fluctuating velocity components of the flow. Thus, present study investigates the axial wind loads acting on the turbine systems and corresponding bending moment due to these axial loads for SRWT and co- and counter-rotating DRWT systems.

As shown in Table 6-1(a), mean (static) wind loads (axial and bending moment) acting on SRWT and DRWT systems are in agreement with the measured power output readings. Addition of a second (downwind) rotor increases the wind loads as well as the power output performance for DRWT systems, and the mean wind loads acting on DRWT systems were found to be at least 55 % more than those acting on SRWT systems. Thus, these additional wind loads necessitates much stronger tower and foundation structures, causing higher initial capital costs for DRWT systems. It is also important to note that a DRWT system has only one tower which also has to stand under additional dead loads (weight) of second (downwind) rotor, hub and related extra components in a comparatively bigger nacelle.

Table 6-1 The wind loads acting on SRWT and DRWTs

Systems	Thrust (axial) loading coefficient (C_{Fx})	Bending Moment coefficient (C_{Mz})
SRWT	0.45	0.52
DRWT (co)	0.70	0.82
DRWT (counter)	0.71	0.83

(a) Static wind loads

Systems	$\sigma(C_{Fx})$	$\sigma(C_{Mz})$
SRWT	0.17	0.16
DRWT (co)	0.20	0.19
DRWT (counter)	0.21	0.20

(b) Dynamic wind loads

Furthermore, the mean wind loads acting on co- and counter-rotating DRWT systems slightly differ from each other, and the wind loads acting on a counter-rotating DRWT system found out to be slightly higher than those acting on a co-rotating system, parallel to the power output performance results. Although mean wind loads are generally taken into account for the mechanical design of wind turbines, the effects of unsteady flow due to wind shear, atmospheric and wake induced turbulence and associated dynamic (fluctuating) wind loads acting on wind turbine systems are paid more and more attention in recent years for an enhanced fatigue lifetime of the wind turbines operating in turbulent ABL winds.

Based on the time sequences of the instantaneous wind loads acting on the SRWT and DRWT systems, as shown in Table 6-1(b), the fluctuation amplitudes of the instantaneous wind loads (the standard deviations of the thrust and bending moment coefficients) acting on DRWT systems were found to be greater (in the range of 17% - 25%) than those acting on SRWT systems. Since the downwind rotor is under the direct influence of upwind rotor wake, downwind rotor could be expected to experience much higher fatigue (dynamic) wind loads, resulting a reduced fatigue lifetime for the downwind rotor in a DRWT system. Moreover, the effect of co- and counter-rotation of a DRWT system on dynamic wind loads was observed to be slightly different as in the case of mean wind loads, and the fluctuation amplitudes of the instantaneous wind loads acting on a counter-rotating DRWT system found out to be slightly higher than those acting on a co-rotating system, as shown in Table 6-1.

c) Near wake PIV measurements – Ensemble averaged results:

The near-wake flow field (X/D<2.5) was measured by using a high-resolution PIV system for SRWT and DRWT systems. The measurement field was separated into two regions with an overlap of 13 mm length and two CCD cameras were used to acquire PIV images from the measurement plane. As mentioned before, ensemble averaged flow quantities such as normalized mean streamwise velocity along with the normalized velocity deficit, normalized Reynolds stress and added turbulence kinetic energy were obtained from 1000 frames of instantaneous PIV measurements.

(a) SRWT

(b) DRWT (co)

(c) DRWT (counter)
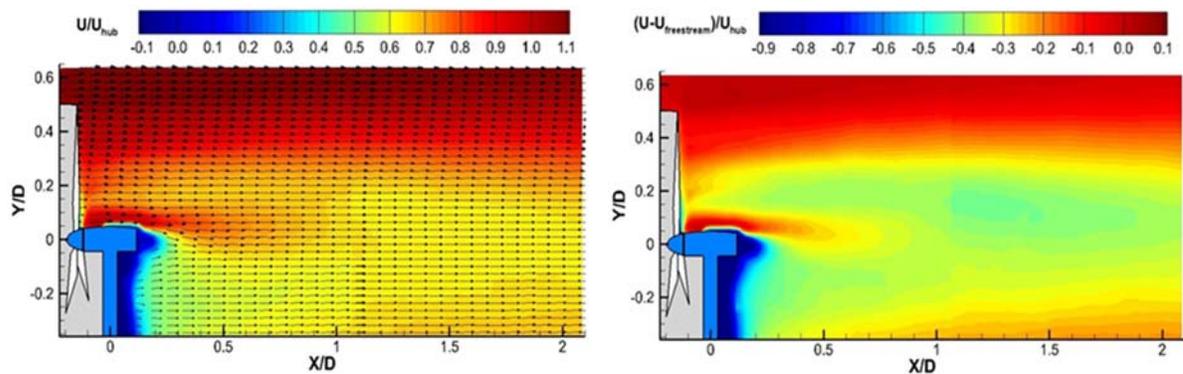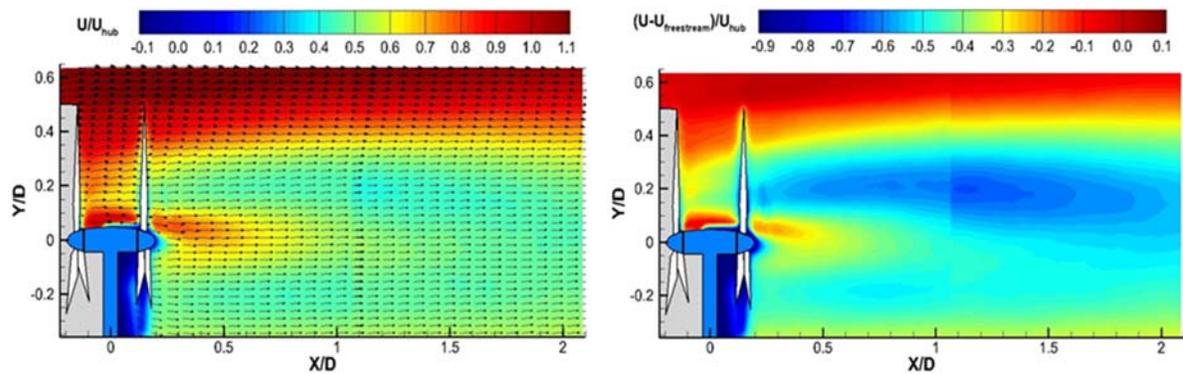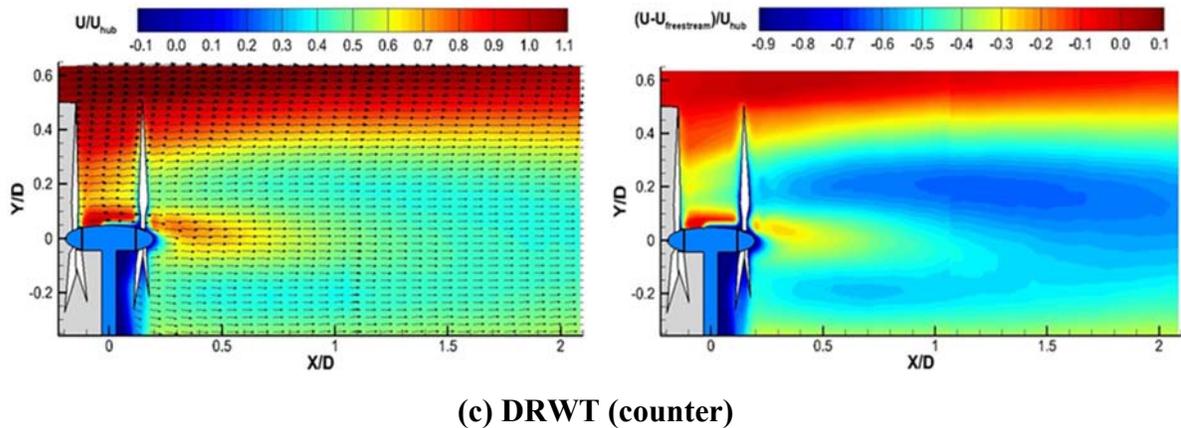
Figure 6-11 The contours of the ensemble-averaged normalized streamwise mean velocity (left), U/U_{hub}, and normalized streamwise mean velocity deficit (right), $\Delta U/U_{hub}$, in the near wake region of SRWT and DRWT systems

Figure 6-11 shows contours of the ensemble-averaged normalized streamwise mean velocity (left), U/U_{hub}, and normalized streamwise mean velocity deficit (right), $\Delta U/U_{hub}$, in the near wake region of different wind turbine configurations obtained from wind-tunnel experiments using PIV technique.

Vertical profiles of the measured ensemble-averaged normalized streamwise mean velocity (top) and normalized streamwise mean velocity deficit (bottom) were also extracted for the quantitative comparison of the PIV results at selected downwind locations (X/D=0.5, X/D=1.0 and X/D=2.0) including the oncoming BL flow profile, as shown in Figure 6-12.

From the measurements, there is clear evidence on the velocity deficit in the wake region, caused by the energy extraction from the wind turbine. As expected, the velocity deficit is largest in the wake of DRWT systems, which can be attributed to the existence of an additional downwind rotor. Thus, DRWT systems harness more energy from the oncoming BL flow, thereby producing a wake region with much larger momentum deficits. Furthermore, the distribution of the mean velocity profile in the near-wake of DRWT systems was found out to be affected from the rotational direction of the downwind (back) rotor, leaving slightly higher velocity deficits in the wake of counter-rotating DRWT system due to the fact that counter-rotating DRWT system was found to harvest more energy (up to 10%) from the same oncoming boundary layer flow in comparison to the co-rotating DRWT system. This is associated with

the significant swirl (azimuthal velocity) contribution from the upwind rotor wake, which provides additional torque for the counter-rotating downwind rotor.
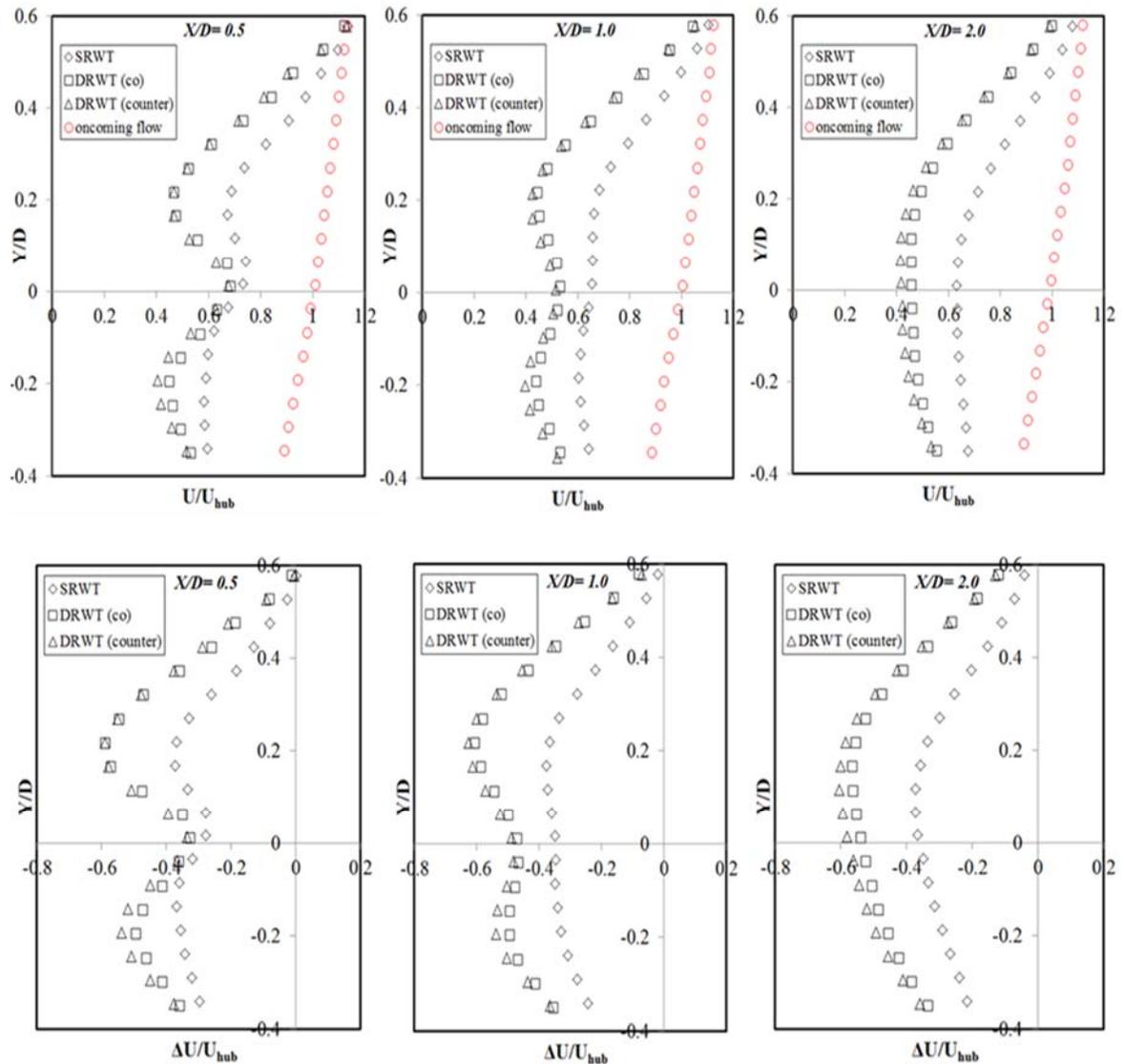
Figure 6-12 The extracted vertical profiles of the PIV measured ensemble-averaged normalized streamwise mean velocity (top) and normalized streamwise mean velocity deficit (bottom) at selected downwind locations (X/D=0.5, X/D=1.0 and X/D=2.0) of SRWT and DRWT systems

The near wake turbulent flow was found to show highly non-axisymmetric characteristics. In particular, the flow in the vicinity of the rotor (X/D<1.0) was observed to be more complicated and could be affected by rotor characteristics such as, rotor size, configuration and rotor-nacelle-hub interactions. Therefore, the presence of a turbine rotor with its non-rotating components, with no contribution to the energy generation, could significantly affect

the flow just behind the turbine. The flow just behind the nacelle and tower is completely blocked and the flow is either stopped or reversed. The PIV results also showed a region with comparatively high streamwise velocity between hub height and blade root sections, extending up to X/D=0.5 or beyond. This is due to the fact that the inner (root) section the blade (closest to the hub) is almost unproductive (no energy generation) and tends to operate as a propeller. However, a sudden drop in the mean streamwise velocity (more pronounced in DRWT systems) was observed starting from the mid-sections of the rotor due to higher energy-harvesting rates on those segments of the rotor. As the downstream distance increases, the strong non-axisymmetric character of the flow is quickly reduced due to strong turbulent mixing caused by the strong shear. Thus, with increasing downstream distance, low momentum zone moves towards the center of the wake and the flow tends to become nearly axisymmetric in the far wake (X/D>2). Furthermore, the non-uniformity of the oncoming flow and the presence of the ground were also found to introduce non-axisymmetry to the mean flow velocity distribution in the wake, as mentioned by Chamorro and Porte-Agel (2009). Thus, they facilitated far wake modeling by using velocity deficit for boundary layer flow so that the distribution becomes axisymmetric and self-similar.

Non-uniform character of the oncoming boundary layer flow also influences the turbulent wake flow structure significantly. For a uniform flow, mean shear distribution in the turbine wake could be axisymmetric with strong shear layer (associated with TKE production) at the levels of bottom-tip and top-tip. However, for an oncoming boundary layer flow with non-uniform mean flow velocity distribution, previous experimental and numerical studies showed that maximum TKE production would occur at the top-tip level as a result of strong shear-produced turbulence and turbulence (momentum) fluxes (Hu et al., 2012; Zhang et al., 2012; Porte-Agel et al., 2011; Wu et al., 2012).

TKE production from adjacent wind turbines, especially in large clusters of turbines which are spaced within the optimum range of streamwise and spanwise distances in wind farms, should be taken into account in terms of the dynamic (fluctuating) wind loads acting on the downstream turbines. In addition, turbulence decay rate was found to be slower than the mean streamwise velocity recovery rate (Vermeer et al., 2003). Thus, it is highly desirable to characterize the turbulence characteristics of the wake flow behind wind turbines in order to

provide better conditions and longer fatigue lifetime for turbines in large arrays. Moreover, turbulent fluxes produced due to wake induced turbulence were found to play an important role on the entrainment of energy from the flow above the wind farm (Meyers and Meneveau, 2013). The present study was performed under the same oncoming flow turbulence conditions in order to reveal the effect of SRWT and DRWT systems on the near wake turbulent flow structures.

(a) SRWT

(b) DRWT (co)

(c)   DRWT (counter)
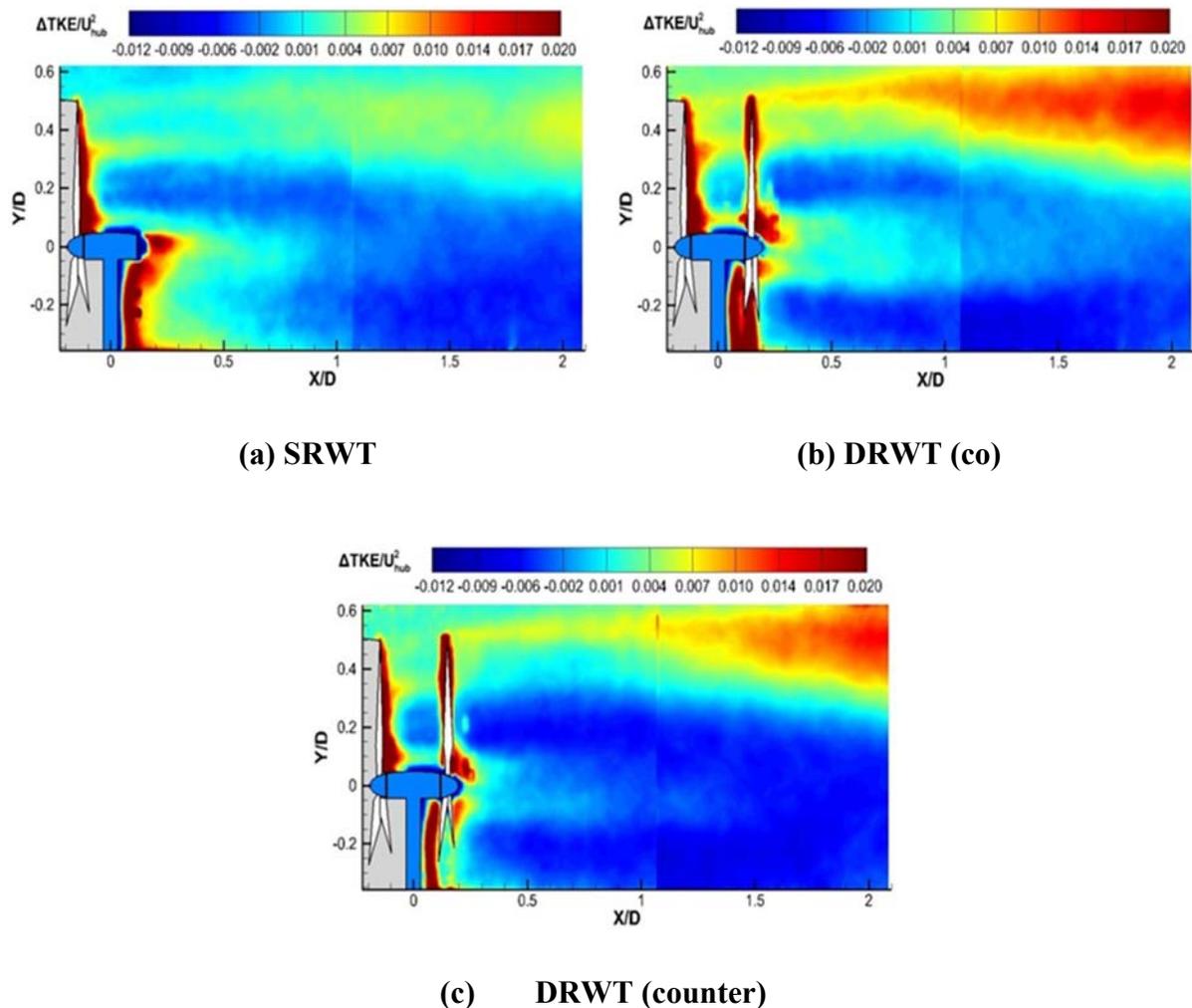
Figure 6-13 The contours of the ensemble-averaged normalized TKE production (subtracted from the oncoming flow TKE), $\Delta TKE/U^2_{hub}$, in the near wake region of SRWT and DRWT systems

Figure 6-13 shows the contours of the ensemble-averaged normalized TKE production (subtracted from the oncoming flow TKE), $\Delta TKE/U^2_{hub}$, in the near wake region of different wind turbine configurations obtained from wind-tunnel experiments using PIV technique. An

obvious enhancement of TKE production was observed at the top-tip level (upper half of the wake) due to the strong shear and momentum flux (towards the wake region). As explained before, it is the result of non-uniform boundary layer flow and the presence of ground. TKE production at the upper half of the wake was found to increase and expand (shear layer expansion) with increasing downstream distance in the near wake. Moreover, higher TKE production levels in the regions (behind the nacelle, tower and rotor section) are believed to be closely related with the flow separation, unsteady vortices and interactions between rotor and non-rotating components of wind turbine.
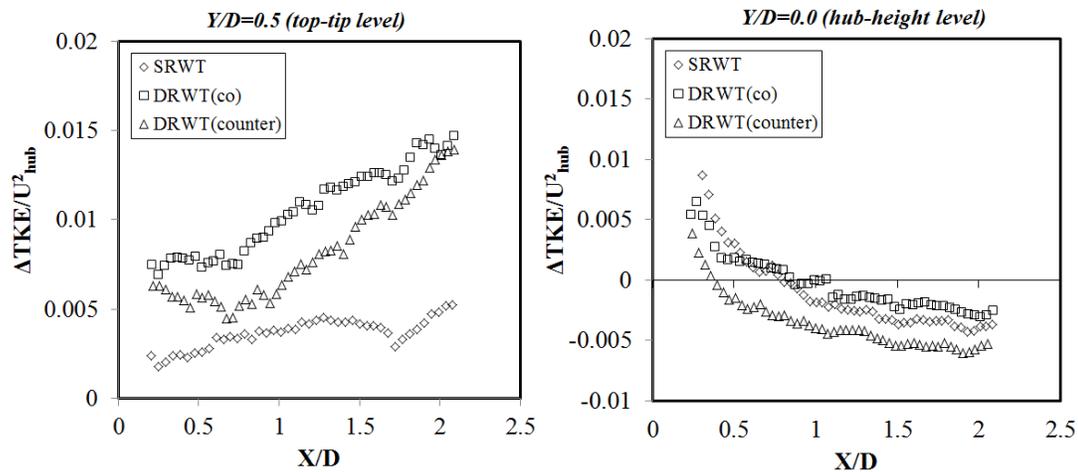
Figure 6-14 The PIV measured ensemble-averaged normalized TKE production at the top-tip (Y/D=0.5) and hub-height (Y/D=0.0) levels extracted throughout the near wake of SRWT and DRWT systems.

The measured ensemble-averaged normalized TKE production were also extracted for the quantitative comparison of the PIV results at the top-tip (Y/D=0.5) and hub-height (Y/D=0.0) levels throughout the near wake of SRWT and DRWT systems, as shown in Figure 16. It is evident from Figure 6-14 that DRWT systems produce higher levels of turbulence kinetic energy at the top-tip level compared to the SRWT systems. Furthermore, the onset of wake instabilities was observed to be different depending on the system. It is clear that for DRWT systems, the wake instabilities at the top-tip level were introduced earlier than those for SRWT systems. It was also observed that TKE production due to these wake instabilities starts at around X/D=0.75 for co-rotating DRWT system and at around X/D=1 for counter-rotating DRWT system and increases throughout the near wake region. According to Wu et al. (2012),

maximum TKE production can be attained approximately from X/D=2 to X/D=5 depending on the oncoming flow turbulence characteristics.

Lignarolo et al. (2013) noted that vortex instability and its breakdown plays an important role on TKE production, and found out that near wake-tip vortices act as a shield preventing the turbulent mixing and TKE production as well (Medici, 2005). From Figure 6-13 and Figure 6-14, it is also clear that TKE production levels before X/D=0.50, where strong tip-vortices were observed, are comparatively lower. Moreover, there is an obvious change in the TKE production trend at hub height level with respect to the top-tip level. In particular, at the hub height level, TKE production becomes much smaller throughout the downstream distances and even negative, indicating that the wake flow is actually less turbulent than the oncoming boundary layer flow at that level. This behavior is in parallel to the findings of Chamorro and Porte-Agel (2009), Zhang et al. (2012) and Wu et al. (2012). Turbulent kinetic energy production at the hub height level of the near wake was also observed to be comparatively lower for counter-rotating DRWT system when compared to the SRWT and co-rotating DRWT system.

Figure 6-15 shows the power spectra of the streamwise velocity fluctuations at the hub height and top tip levels in the near wake (X/D=0.5 and X/D=2.0) of SRWT and DRWT systems. It illustrates the turbulent kinetic energy content of the wake flow over a wide range of frequency scales. For an undisturbed oncoming flow, the spectra exhibit a decrease in the low frequency range from the hub height level to the top tip level, as also observed by Chamorro et al. (2012). As shown in Figure 6-15, an enhancement in the turbulent kinetic energy contribution over the full frequency range was observed at the top-tip levels of SRWT and DRWT systems at X/D=0.5 and at X/D=2.0, and shows an increasing trend with downstream distances from X/D=0.5 to X/D=2.0 due to the increased TKE production with shear layer expansion. In particular, near the top tip level of the rotor (X/D=0.5), the corresponding frequencies at the peaks in the power spectra of SRWT and DRWT systems were believed to be the vortex shedding frequencies (3f) associated with the wind turbine rotor frequency (f).
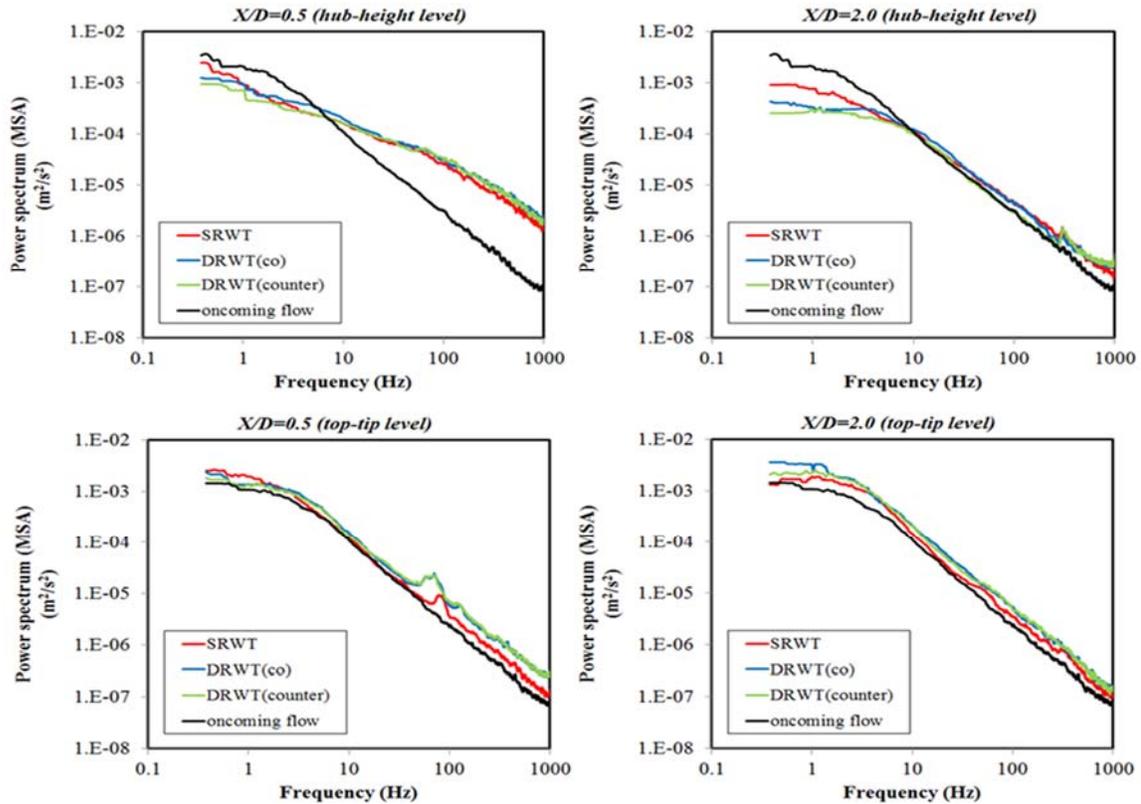
Figure 6-15 Power spectra (Mean Squared Amplitude - MSA) of streamwise velocity fluctuations at the top-tip (Y/D=0.5) and hub-height (Y/D=0.0) levels obtained at selected downwind locations (X/D=0.5 and X/D=2.0) of SRWT and DRWT systems

Furthermore, for the hub height level, the spectra exhibit a decrease in the low frequency range and an increase in the intermediate-high frequency range, as compared to the oncoming flow. As X/D increases from 0.5 to 2, the decrease in the turbulent kinetic energy content of the wake flow for the low frequency range was observed to dominate the spectra, and the enhanced turbulent energy content in the intermediate-high frequency range diminishes. At X/D=2, the significant decrease in the TKE production at the hub height level was found to be related with the lower TKE content in the low frequency range; however, higher energetic content of the wake flow at the top tip level could be associated with a wide range of frequency scales. In general, the results obtained from the power spectra analysis were found to be in good agreement with the TKE results extracted from the PIV measurements.

The inertial subrange of the energy spectra, as shown in Figure 6-15, was found to follow the Kolmogorov's -5/3 slope except the spectra X/D=0.5 downstream of the SRWT and DRWT systems at the hub-height level. The slope of the inertial subrange at that region was

found to be flatter due to the low values of intermittency in weak turbulence regimes (Szilagyi et al., 1996). However, the spectral slope of -5/3 was observed to recover for the inertial subrange as the turbulent flow develops X/D=2.0 downstream of the SRWT and DRWT systems at the hub-height level.

(a) SRWT

(b) DRWT (co)

(c) DRWT (counter)
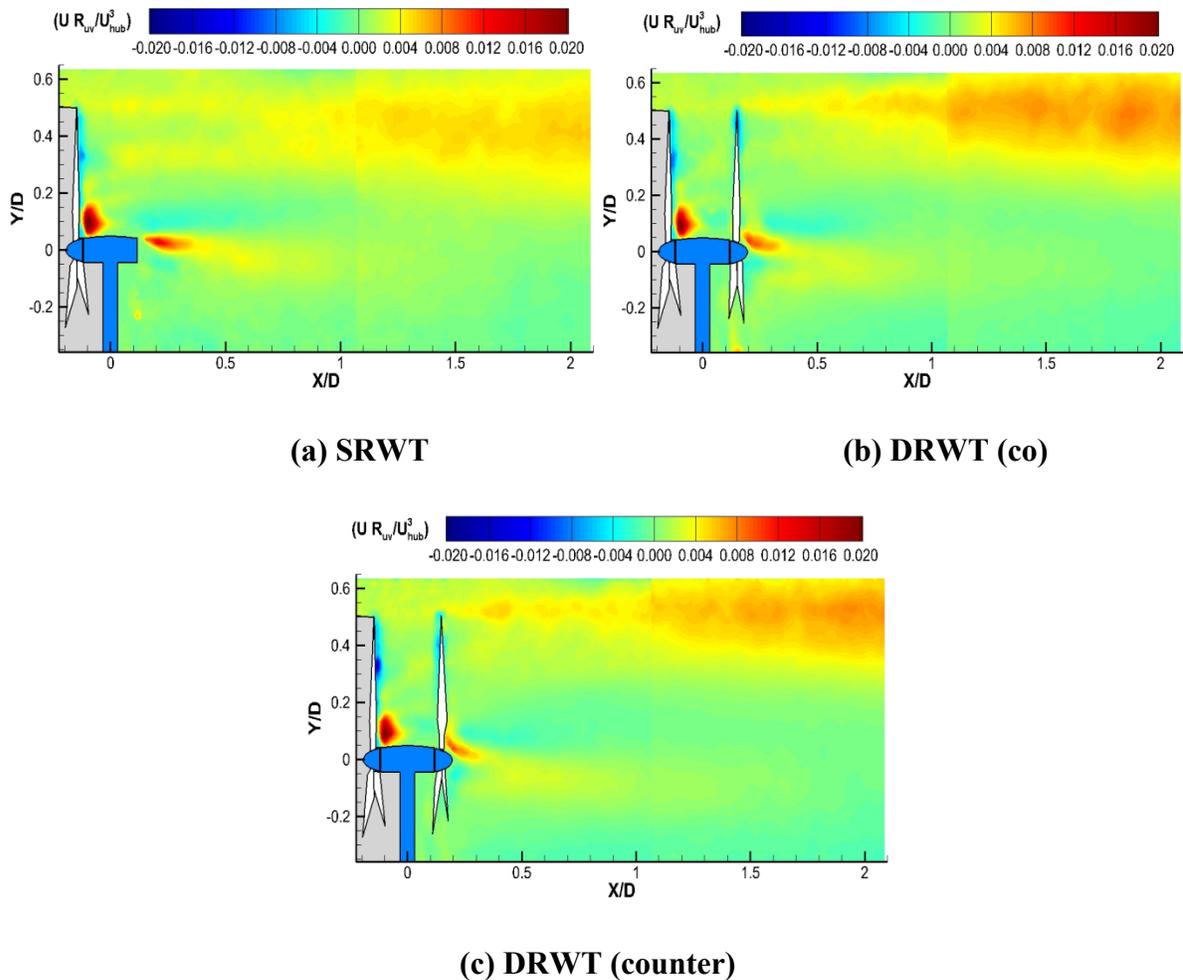
Figure 6-16 The contours of the ensemble-averaged normalized vertical kinetic energy flux, $U\ R_{uv}/U^3_{hub}$ where R_{uv} is the Reynolds shear stress in the vertical streamwise plane, in the near wake region of SRWT and DRWT systems

Figure 6-16 displays the contours of the ensemble-averaged normalized vertical kinetic energy flux, $U\ R_{uv}/U^3_{hub}$, in the vertical streamwise plane, in the near wake region of different wind turbine configurations obtained from wind tunnel experiments using PIV technique. It was seen that higher (positive) levels of kinetic energy flux occur at the top tip level analogous to the TKE production, and it increases at the top tip level with increasing downwind distance

in the near wake. It should also be noted that positive flux region expands along with the shear layer at the top-tip level throughout the wake. Higher (positive) flux areas were also observed behind the nacelle and root sections of the rotors. Another interesting finding is the existence of negative flux areas located in the wake between bottom tip and hub height.

The vertical kinetic energy flux in the wind turbine wake leads to faster wake recovery due to the fact that it entrains high momentum boundary layer flow into the wake, producing a radial momentum flux towards the wake center, as mentioned by Wu et al. (2012), Calaf et al. (2010) and Cal et al. (2010). In wind farms, having clusters of wind turbines, wake induced turbulent fluxes help turbine systems extract the energy entrained from the upper high momentum boundary layer flow (Lebron et al., 2012). Furthermore, Cal et al. (2010) showed that these turbulent kinetic energy fluxes are on the same order of magnitude as the power extracted by the wind turbines in wind farms.
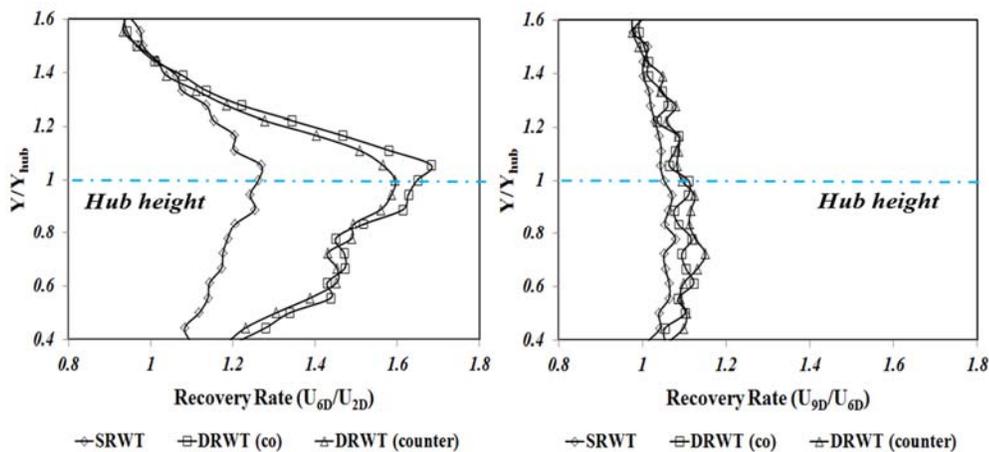
Figure 6-17 The streamwise velocity recovery rates for SRWT and DRWT systems between 2D - 6D (top) and 6D - 9D (bottom)

Figure 6-16 reveals the fact that DRWT systems produces much higher levels of vertical kinetic energy flux at the top tip level compared to the SRWT systems, thus providing higher entrainment flux towards the wake center. This phenomenon suggests that for DRWT systems, wake flows could recover much faster, and especially knowing the fact that they leave much lower momentum zone in their wake, far wake turbulent flow structure characteristics should be further investigated for the feasibility of implementing DRWTs in wind farms. Therefore, Figure 6-17 shows the streamwise velocity recovery rates for SRWT and DRWT systems in the far wakes. It was observed that wake recovered much faster for DRWT systems, and

recovery was found to be effective between 2D and 6D downstream distances. This suggests that higher velocity deficits behind DRWT systems could be compensated with faster recovery rates so that the spacing between DRWT systems in a wind farm could be the same as the spacing between SRWT systems.

### d) Near wake PIV measurements – Phase locked results:

Phase locked PIV measurements were carried out to provide "frozen" images of unsteady wake vortex structures at different phase angles. At the phase angle of $\phi=0.0°$, the pre-marked turbine blade was adjusted to be in the most upward position. As phase angle increases, pre-marked turbine blade would rotate out of the vertical PIV measurement plane in counter clock-wise (CCW) direction. Figure 6-18, Figure 6-19 and Figure 6-20 show the phase-locked averaged PIV measurement results; normalized streamwise velocity deficit (left), vorticity (middle) and swirling strength (right), for SRWT and co- and counter-rotating DRWT systems at various phase angles of $\phi=0.0°$, $\phi=30.0°$, $\phi=60.0°$,and $\phi=90.0°$. It should also be noted that for DRWT systems, the upwind rotor was phase-locked while the downwind rotor was rotating freely (free-run) during the measurements.

Higher streamwise velocity deficit zone is evident from the phase locked averaged velocity gradients (strong shear) in the near wake. Towards the wake centerline zone, the velocity deficit would get stronger, and this effect was found to be more pronounced for DRWT systems, as mentioned before. Wave-shaped flow structures due to the periodic shedding of coherent (vortex) structures were also observed at the top tip height of the wake in agreement with the observations of Hu et al (2012).

The phase-locked PIV measurements reveal the unsteady wake vortex signatures of both the tip and root vortices. However, the wake flow contains strong shear, and vorticity cannot really distinguish between shear and the actual swirl. Thus, along with the z-vorticity component, $w_z = dV/dx - dU/dy$, the swirling strength (λ_{ci}) criterion, proposed by Zhou et al. (1999), was used for vortex visualization and identification Therefore, the imaginary part of the complex eigenvalue of the velocity gradient tensor (∇u) was used to quantify the strength of the local swirling motion inside the vortex (Kolar, 2007).

The tip vortices were formed between the oncoming freestream and the wake flow in the strong shear region at the top-tip level. As the phase angle increases, the tip vortices were found

to shed from the tip of the turbine blades. Interestingly, secondary vortices were also observed to shed in the vicinity of Y/D=0.35 region, and these vortices were found to be comparatively stronger than the tip vortices. This could be associated with the rotor blade design and its shape. Furthermore, those tip and secondary vortices ($w_z<0.0$) become weaker with the downwind distances due to viscous dissipation, turbulent mixing and wake instabilities. In addition, root vortices ($w_z>0.0$) were also found to exist closer to the rotational axis (Y/D<0.15).
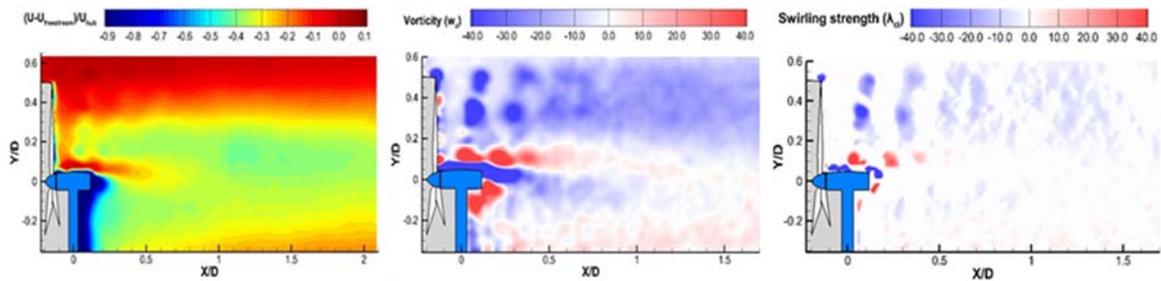
Phase angle, φ=0.0°
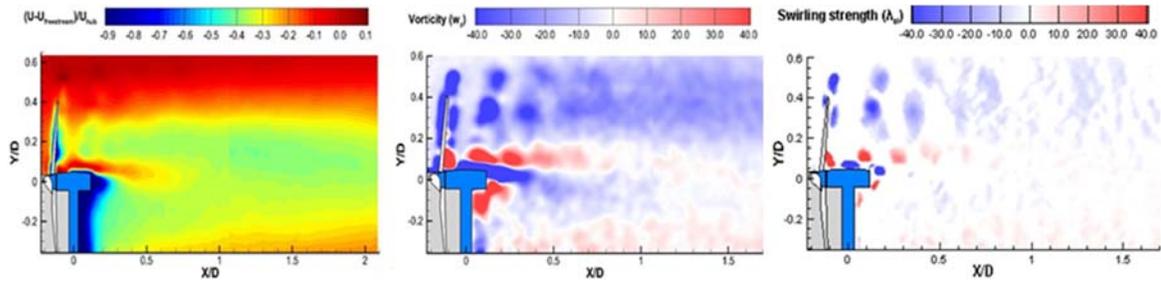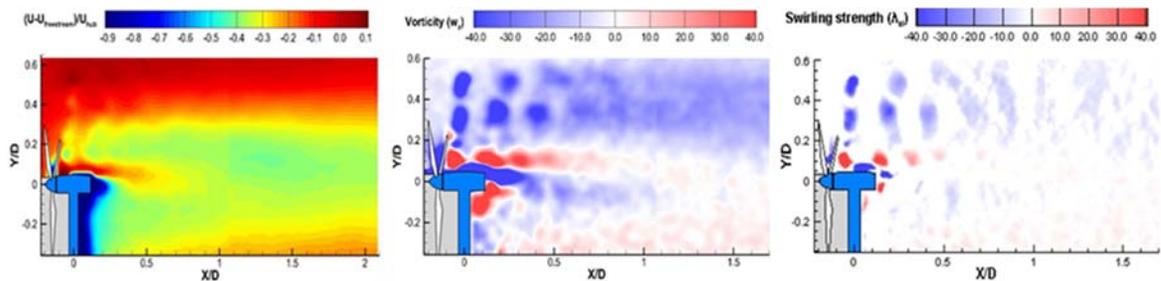
Phase angle, φ=30.0°
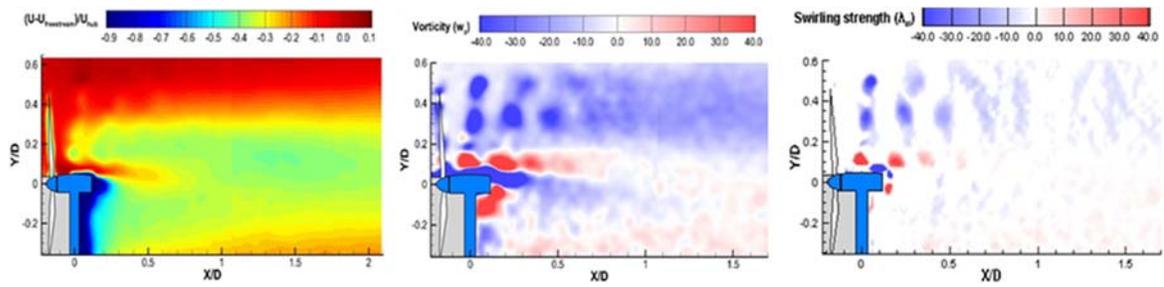
Phase angle, φ=60.0°

Phase angle, φ=90.0°

Figure 6-18 The phase-locked averaged PIV measurement results; normalized streamwise velocity deficit (left), vorticity (middle) and swirling strength (right), for SRWT system at various phase angles of φ=0.0°, φ=30.0°, φ=60.0°,and φ=90.0°
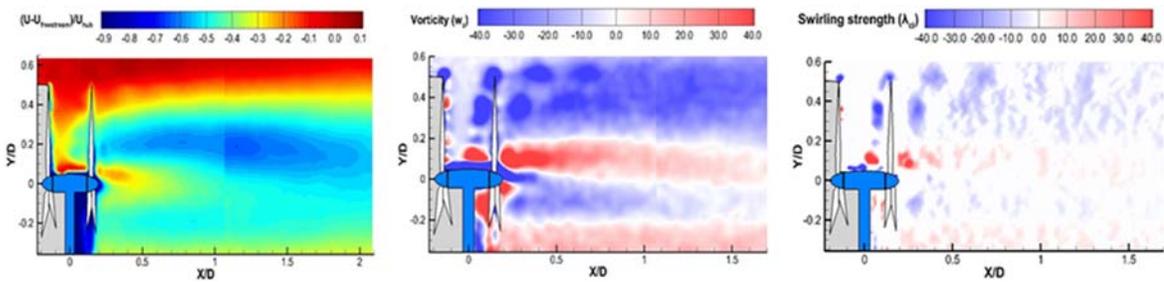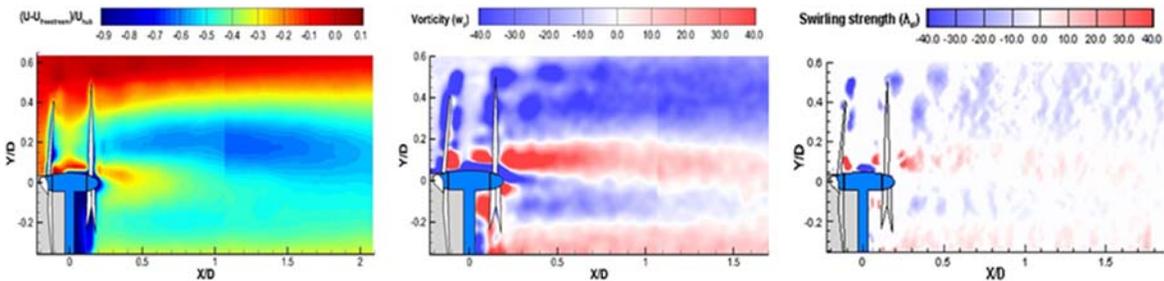
Phase angle, φ=0.0°
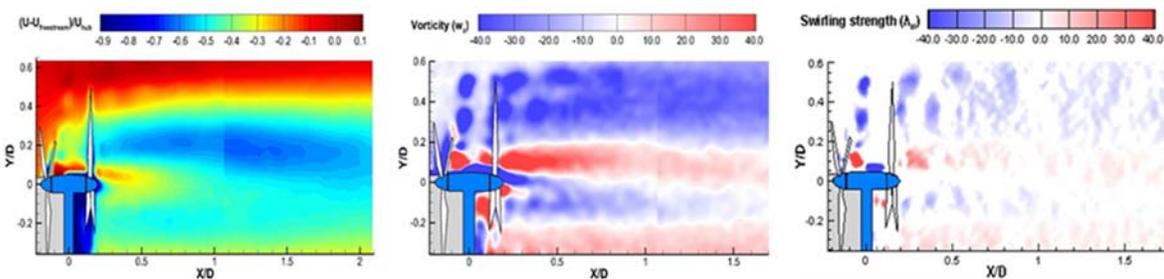
Phase angle, φ=30.0°
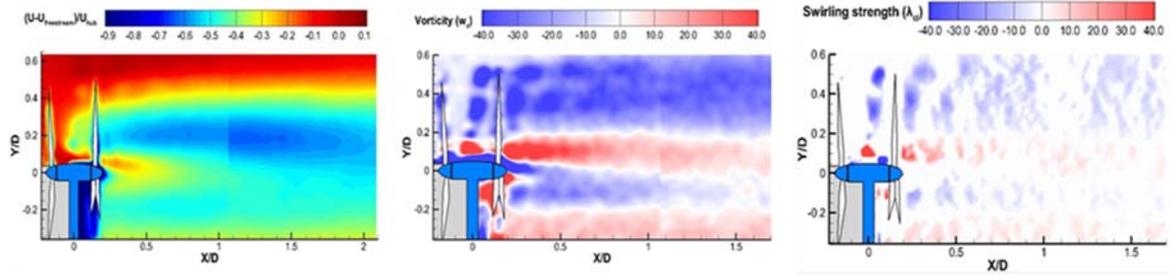
Phase angle, φ=60.0°

Phase angle, ɸ=90.0°

Figure 6-19 The phase-locked averaged PIV measurement results; normalized streamwise velocity deficit (left), vorticity (middle) and swirling strength (right), for co-rotating DRWT system at various phase angles of upwind rotor, ɸ=0.0°, ɸ=30.0°, ɸ=60.0°,and ɸ=90.0°
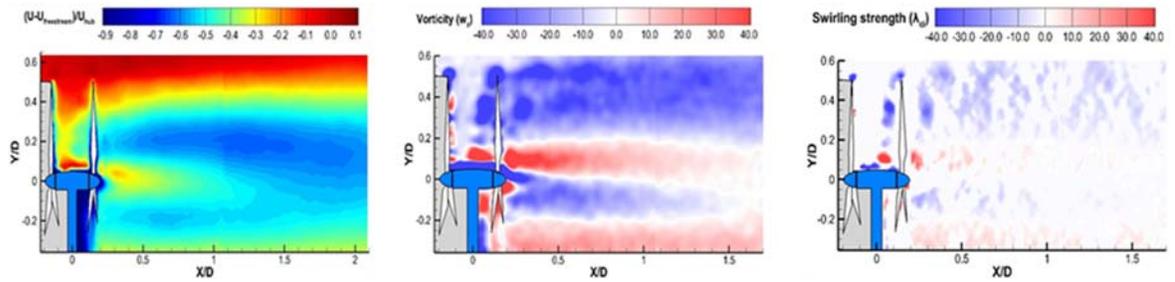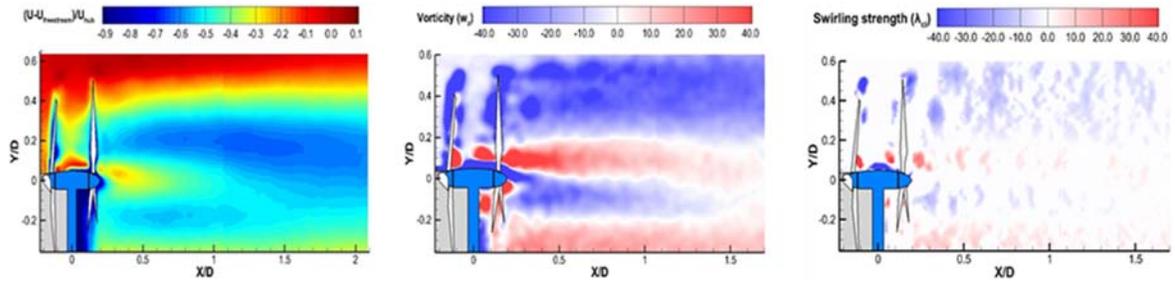
Phase angle, ɸ=0.0°
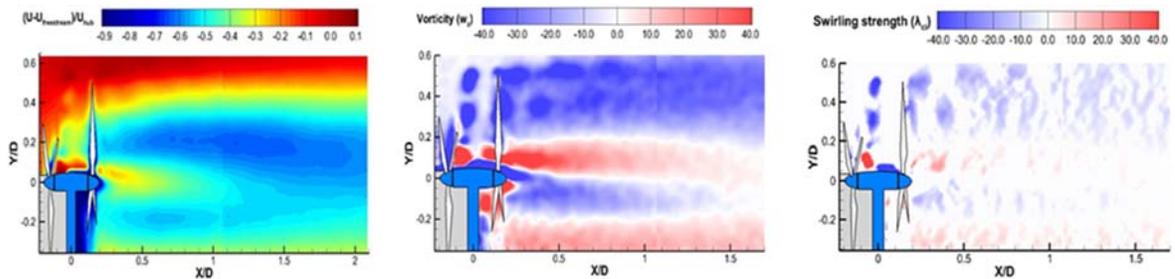
Phase angle, ɸ=30.0°
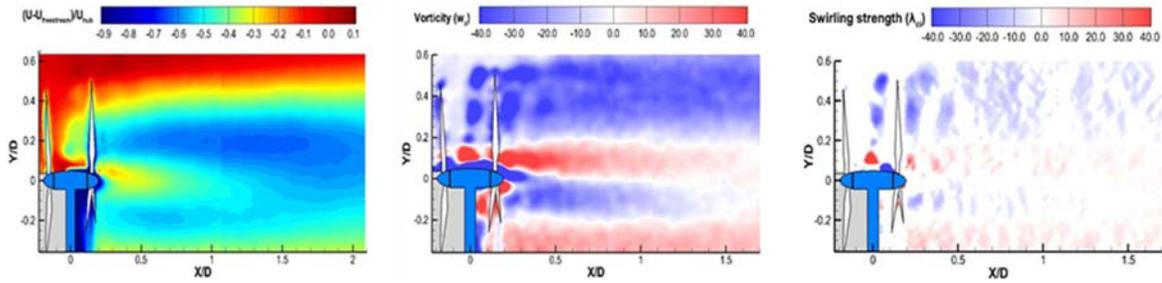
Phase angle, ɸ=60.0°

Phase angle, ϕ=90.0°

Figure 6-20 The phase-locked averaged PIV measurement results; normalized streamwise velocity deficit (left), vorticity (middle) and swirling strength (right), for counter-rotating DRWT system at various phase angles of upwind rotor, ϕ=0.0°, ϕ=30.0°, ϕ=60.0°,and ϕ=90.0°

The tip and root vortices contain the wake induced velocity components both in the direction of and opposing the mean streamwise flow (Sherry et al., 2013). The relative velocity vectors (after subtracting the local velocity at the center of the root and tip vortices) at a phase angle of ϕ=0.0° in the near wake of SRWT system were also given in Figure 6-21 to clearly demonstrate the vortex formation.
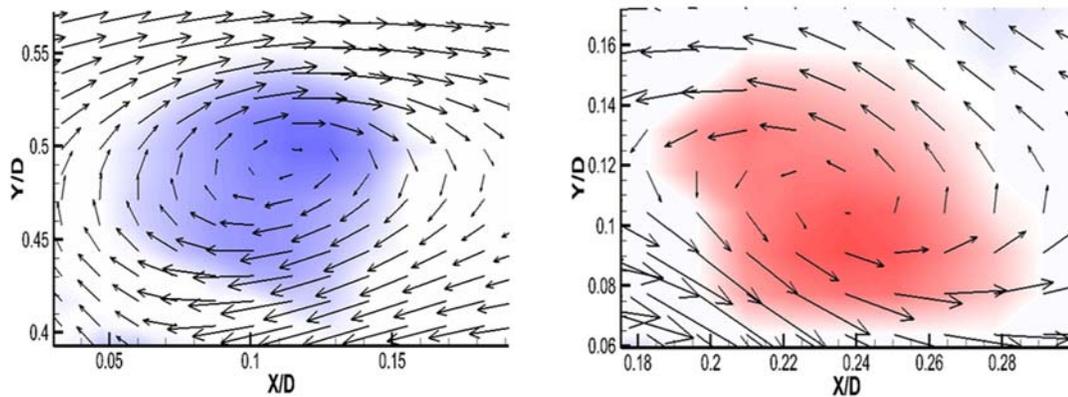
Figure 6-21 The relative velocity vectors in the vicinity of tip (top) and root (bottom) vortices (after subtracting the local central velocity) at a phase angle of ϕ=0.0° in the near wake of SRWT system

The vorticity created within the nacelle boundary layer was also observed immediately adjacent to the nacelle in agreement with the findings of Sherry et al. (2013), and it has opposite sign with respect to the root vortices. Furthermore, Sherry et al. (2013) attributed the rapid destruction of root vortices to the presence of the vortices with the opposite sign within the nacelle boundary layer.

For DRWT systems, the maximum absolute values of vorticity for shedding tip and secondary vortices were found to be stronger than those for the SRWT system. This is mainly due to the contribution of dU/dy term in vorticity equation which is associated with the vertical velocity gradient. Thus, greater velocity deficits would cause greater gradients in the vertical direction, as in the case of DRWT systems. However, no significant difference was observed on the maximum absolute vorticity values of co- and counter-rotating DRWT systems.

The swirling strengths, associated with the imaginary part of the complex eigenvalue of the velocity gradient tensor ($\nabla u = dU/dx \ dU/dy; \ dV/dx \ dV/dy$), for shedding tip and secondary vortices were also found to be greater for DRWT systems, with no significant difference between co- and counter-rotating DRWT systems, in agreement with the vorticity results. Moreover, vortex instability and its breakdown, due to vortex-vortex interaction and vortex diffusion, was observed to start earlier for DRWT systems in agreement with the TKE production results.

The strength of root vortices introduced in the near wake of the counter-rotating DRWT system was observed to be weaker due to cross-annihilation of root vortices from upwind and downwind rotors. Thus, corresponding TKE production levels obtained closer to the rotor was found to be relatively lower for counter-rotating DRWT in comparison to SRWT and co-rotating DRWT systems.

6.4 Conclusion

The measurement results revealed that the power production performances of DRWTs along with the static and dynamic wind loads acting on the system were found to be much higher compared to the single rotor (SRWT) system. Furthermore, the rotational direction of the dual rotors could have a significant effect on DRWT systems. The counter-rotating DRWT system, in which rotors rotate at opposite directions, was found to harvest more energy than co-rotating DRWT system. This is due to the fact that a second rotor installed in the near wake of an upwind one could harness the additional energy available in the swirl (tangential) flow when rotors rotate at opposite directions. Thus, the power production from the downwind rotor increases as it exploits the additional energy associated with the swirl flow thereby increasing the overall power production from DRWT system. Although DRWT systems were found to

improve the power production performance, higher static and dynamic wind loads acting on those systems would result in higher construction costs and shorter fatigue lifetime.

The near wake turbulent flow structure behind SRWT and DRWT systems were also investigated by free-run and phase-locked PIV measurements. It was found that largest velocity deficits were found to occur in the near wake of DRWT systems as they harness more energy from the oncoming boundary layer wind. As expected, higher vertical kinetic energy flux and TKE production were found to concentrate on the top-tip levels of the wake in agreement with the previous studies. Furthermore, DRWT systems were found to produce much higher turbulent fluxes at the top tip level compared to the SRWT system with no significant difference between co- and counter-rotating configurations. In particular, higher Reynolds shear stress in the top tip wake of DRWT systems would provide greater vertical turbulent kinetic energy (momentum) flux into the central wake region. Thus, wake flows could recover much faster for DRWT systems.

Phase-locked PIV measurements were also carried out to characterize the vortex structures in the wake of SRWT and DRWT systems. Vorticity (w_z) and swirling strength (λ_{ci}) were used for vortex characterization and identification. The maximum values of vorticity and swirling strength for shedding tip and secondary vortices were found to be greater in DRWT systems, with no significant difference between co- and counter-rotating configurations, when compared to those in SRWT system. In addition, wake instabilities were found to be introduced earlier and more intense in DRWT systems in the light of free-run and phase-locked PIV measurements.

Future research will focus on the investigation of the far wake structures and characteristics of SRWT and DRWT systems and utilization of DRWTs in wind farm operations in order to draw conclusions on the feasibility of using DRWTs for large scale wind farm applications.

GENERAL CONCLUSION/SUMMARY

The present thesis summarizes several topics concerning the wind tunnel investigation of the performance and loading of wind turbines/farms.

In Chapter 2, a wind tunnel study was conducted to assess and investigate the boundary layer wind flow characteristics over two dimensional Gaussian hill models with different geometries. Furthermore, power output performance of the wind turbines along with the dynamic wind loads acting on them were quantified so as to fully understand the effect of the terrain topology on the wind turbine performance and loading. Moreover, non-flat terrain wind farms were simulated by placing five wind turbines along the two Gaussian hill models with different geometries to characterize the wake interactions, and evaluate the performance of the wind farms in non-flat terrains. The experimental (quantitative) results from these terrains were then compared to those obtained from the simple (flat) terrain.

The results indicate that the flow field along the hilly terrain could be quite different than the flow field in flat terrain, thus significantly affecting the performance and loading of wind turbines/arrays. The flow field along the hill was exposed to several effects; such as speed-up effects, flow separation and shadowing effects. All these effects were found to strongly dependent on the geometry (slope) of the hill. In particular, speed-up and flow separation effects could be the key elements determining the performance and loading of the wind turbines/arrays. As the slope increases, the flow behind the hill tends to separate, and the separated region with higher velocity deficits and enhanced turbulence levels, would also mitigate the speed-up effects on the top of the hill. In case of the high slope hill simulated in the wind tunnel, the wind turbines sited in the separated region could experience greater power deficits and enhanced dynamic wind loads. Furthermore, wake interference effects (in case of a wind farm along the high slope hill) behind the hill would be almost negligible when compared to the flow separation effects. However, the traces of the speed-up effects could still be seen in the leeward side of the low slope hill with no flow separation. As opposed to the high slope hill case, wake interference effects behind the hill would be more obvious in the low slope hill case. However, flow separation effects were found to be more severe behind the high slope hill than the wake interference effects behind the low slope hill, thus causing greater power deficits and enhanced dynamic loads for the wind turbines behind the high slope hill.

As a result, hilly terrains with low/gentle slope could have great potential for wind energy production (speed-up effects). The wind farms sited along the low/gentle slope hills would be more efficient than the ones in flat terrain. However, the flow separation behind steep/high slope hills could deteriorate the performance of the wind turbines behind the hills, thus degrading the wind farm performance. Furthermore, the total power output from the wind farm sited along the steep hills would be much less than the one in the flat terrain. It should also be noted that dynamic loads (quantified by calculating the intensity of thrust fluctuations) imposed especially on the downstream turbines sited behind the steep hills could severely affect the fatigue lifetime of the wind turbine components. These fluctuating loads (more pronounced on the downstream turbines behind the hill, and greater than those observed in flat terrain) were primarily due to the flow separation behind the high slope hill, while they were primarily due to the wake interference effects behind the low slope hill.

In Chapter 3, the effects of the oncoming (ambient) flow conditions on the turbine wake characteristics and wind loads acting on a model wind turbine were investigated. The experiments were carried out in a large-scale atmospheric/aerodynamic boundary layer wind tunnel under different atmospheric boundary layer wind conditions with different wind profiles and turbulence characteristics. Therefore, a model wind turbine was sited in two different environments, corresponding to typical offshore and onshore environments (i.e., the offshore and onshore case), simulated in the wind tunnel. Along with the dynamic wind load measurements, detailed flow field measurements were conducted in the turbine wake by using a high resolution Particle Image Velocimetry (PIV) and Cobra Probe Anemometry system. In this investigation, the evolution of the unsteady vortex and turbulent structures in the wake were quantified and correlated with the dynamic loads in typical offshore and onshore boundary layer winds.

The results indicate that oncoming flow turbulence could play a central role in the wake development behind the wind turbine. The free-run and phase-locked PIV measurements revealed the information about the ensemble averaged flow statistics (mean flow velocity, Reynolds stress, and TKE) in the wake and shed light on the evolution of the unsteady tip vortex structures. The evolution of the unsteady tip vortex structures was found to be strongly dependent on the oncoming flow turbulence through phase-locked PIV measurements. Higher

levels of turbulence in the oncoming flow (onshore case) were found to speed up the breakdown process of the concentrated tip vortex structures. Thus, this process would cause a dramatic increase in the TKE and Reynolds stress levels at the top-tip height of the turbine wake. The higher TKE and Reynolds stress levels in the wake were found to promote vertical mixing through the transport of the kinetic energy from above, thereby re-charging the wake and facilitating the wake recovery. This effect was also revealed from the ensemble averaged velocity distributions in the turbine wake, and it was shown to be more effective for the onshore case, in comparison with the offshore case. Therefore, the wake interference effects and the corresponding power deficits would be less severe for the downstream turbines sited in the onshore wind farms, in comparison with those sited in the offshore wind farms. This could also be used to explain the so called 'deep array effect', which leads to the under-prediction of the wake losses in large offshore wind farms.

Furthermore, the effect of the breakdown process on the unsteady tip vortices was also revealed from the power spectra of the streamwise and vertical velocity fluctuations in the near wake. The signatures of the tip vortices in the offshore case were found to be much stronger than those in the onshore case due to the slower dissipation rate of the shedding tip vortices in the offshore case.

Finally, higher levels of turbulence in the oncoming flow (onshore case) were shown to cause greater fluctuations in the rotational speed of the wind turbine as well as in the dynamic wind loads acting on the wind turbine, which could impose greater fatigue loads on the wind turbine components. All these effects would be more severe for a turbine sited in an onshore environment, as compared to a turbine in an offshore environment.

In Chapter 4, the main focus is on the dynamics in wind farms of variable layouts (aligned and staggered) and turbine spacings, and the effect of the oncoming flow turbulence on the wind turbine/farm performance and loading as well as on the flow within the wind farm.

The results indicate that oncoming flow turbulence along with the turbine layout and spacing could significantly affect the flow dynamics inside the wind farm. The corresponding

wind turbine/farm performance and loading were found to be very sensitive to the changes in the flow dynamics within the array. The higher oncoming flow turbulence level (onshore applications) was found to increase the wind turbine/farm efficiency through strong turbulent mixing process (ensuring a faster wake recovery); however, it was also found out to be the cause of the dynamic (fatigue) loading on the wind turbine components. Furthermore, the advantages of the staggered wind farm layout over the aligned one with similar (3D) and double (6D) spacing were revealed. Staggering the turbines was found to not only mitigate the wake-induced effects but also impose a venturi effect thereby improving the power output performance of the wind turbine/farm. This study also suggests that staggering could be more effective on the wind turbine/farm performance than spacing the turbines farther apart. The results from this investigation shed light on some aspects of the wind farm optimization, and they could be used for validating numerical models and simulations as well. However, it should be noted that the wind farm optimization is a very complex problem with a lot of variables involved apart from the oncoming flow character, and turbine layout and spacing.

In Chapter 5, the performances of two wind turbine models in tandem arrangement with 2D spacing were tested on different upstream wind turbine yaw conditions to confirm the effectiveness of using yaw angle optimization method and further investigate the dependence of this method on the oncoming (offshore and onshore) wind turbulence level.

The results indicate that the effectiveness of upstream turbine yaw angle control for wind farm optimization was found to be strongly dependent on the turbulence intensity levels of the oncoming wind. The wind farm efficiency in offshore terrain environment with lower ambient turbulence levels could be improved up to 5% at an upstream turbine yaw angle of $\alpha=10°$ with 2D spacing between the turbines. However, although higher turbulence levels observed in onshore terrain environment increases the overall wind farm efficiency, yawing the upstream turbine was found to have a negative impact on the overall efficiency of the wind farm. This investigation could be further extended to offshore wind farms with clusters of wind turbines in order to investigate the effects of the yaw angle optimization on the efficiency of larger wind arrays.

In Chapter 6, the effects of adding an extra (downwind) rotor with counter-rotating (rotors rotate at opposite directions) and co-rotating (rotors rotate at same direction) concepts on the power production performance of the individual rotors of the system, overall DRWT system performance and the wind loads (both static and dynamic) acting on the system were investigated, and these results were compared to those of a traditional SRWT system. This chapter further discussed the near wake turbulent flow structure characteristics of DRWT systems in order to illustrate their differences from conventional SRWT systems. Therefore, wind-tunnel experiments were carried out using intrusive (point-wise) and non-intrusive (PIV) measurement techniques in order to characterize the near wake turbulent flow structures in a neutral boundary layer flow.

The results indicate that the power production performances of DRWTs along with the static and dynamic wind loads acting on the system could be much higher compared to the single rotor (SRWT) system. Furthermore, the rotational direction of the dual rotors was found to have a significant effect on DRWT systems. The counter-rotating DRWT system, in which rotors rotate at opposite directions, was found to harvest more energy than co-rotating DRWT system. This is due to the fact that a second rotor installed in the near wake of an upwind one could harness the additional energy available in the swirl (tangential) flow when rotors rotate at opposite directions. Thus, the power production from the downwind rotor increases as it exploits the additional energy associated with the swirl flow thereby increasing the overall power production from DRWT system. Although DRWT systems were found to improve the power production performance, higher static and dynamic wind loads acting on those systems would result in higher construction costs and shorter fatigue lifetime.

The near wake turbulent flow structures behind SRWT and DRWT systems were also investigated by free-run and phase-locked PIV measurements. It was found that largest velocity deficits were found to occur in the near wake of DRWT systems as they harness more energy from the oncoming boundary layer wind. As expected, higher vertical kinetic energy flux and TKE production were found to concentrate on the top-tip levels of the wake in agreement with the previous studies. Furthermore, DRWT systems were found to produce much higher turbulent fluxes at the top tip level compared to the SRWT system with no significant difference between co- and counter-rotating configurations. In particular, higher Reynolds

shear stress in the top tip wake of DRWT systems would provide greater vertical turbulent kinetic energy (momentum) flux into the central wake region. Thus, wake flows could recover much faster for DRWT systems.

Phase-locked PIV measurements were also carried out to characterize the vortex structures in the wake of SRWT and DRWT systems. Vorticity (w_z) and swirling strength (λ_{ci}) were used for vortex characterization and identification. The maximum values of vorticity and swirling strength for shedding tip and secondary vortices were found to be greater in DRWT systems, with no significant difference between co- and counter-rotating configurations, when compared to those in SRWT system. In addition, wake instabilities were found to be introduced earlier and more intense in DRWT systems in the light of free-run and phase-locked PIV measurements.

This investigation could be further extended to investigate the far wake structures and characteristics of SRWT and DRWT systems and utilize DRWTs in wind farm operations so as to draw conclusions on the feasibility of using DRWTs for large scale wind farm applications.

BIBLIOGRAPHY

20% Wind energy by 2030. (2008). U.S. Department of Energy (DOE) Report

AWEA (2014) – American Wind Energy Association, U.S. Wind Industry 2014 Market Reports

REN21 (2014) – Renewable Energy Policy Network for the 21st Century, Renewables 2014 Global Status Report

Abkar, M., & Porté-Agel, F. (2014). The effect of atmospheric stability on wind turbine wakes: A large-eddy simulation study, Journal of Physics 524 (2014) 012138 doi:10.1088/1742-6596/524/1/012138

Adaramola, M. S., & Krogstad, P. A. (2011). Experimental investigation of wake effects on wind turbine performance. Renewable Energy: An International Journal, 36(8), 2078-2086. doi:10.1016/j.renene.2011.01.024

Ainslie, J.F. (1988). Calculating the flow field in the wake of wind turbines. Journal of Wind Engineering and Industrial Aerodynamics

Alfredsson, P.H., Dahlberg, J.A., & Vermeulen, P.E.J. (1982). A comparison between predicted and measured data from wind turbine wakes. Wind Energy; 6(3):149-155.

American Society of Civil Engineering (2005). ASCE 7-05 minimum design loads for building and other structures, ASCE

Appa, Kari. (2002). Counter rotating wind turbine system, Energy Innovations Small Grant (EISG) Program Technical Report, California, U.S.

Archer, C.L., Mirzaeisefat, S., & Lee, S. (2013). Quantifying the sensitivity of wind farm performance to array layout options using large-eddy simulations. Geophysical Research Letters, 40(18), 4963-4970. doi: 10.1002/grl.50911

Architecture Institute of Japan (1996). AIJ recommendations for loads on buildings

Argyriadis, K. Wind conditions for offshore wind turbine design, RECOFF, comparison of Standards and Regulations. Germanischer Lloyd WindEnergie GmbH, Steinhöft 9, 20459 Hamburg, Germany

Arya, S., Capuano, M., & Fagen, L. (1987). Some fluid modeling studies of flow and dispersion over two-dimensional low hills. Atmospheric Environment Vol.21, No. 4, 753-764.

Arya, S. (1988). Introduction to Micrometeorology. Academic Press

Baker, R.W., & Walker, S.N. (1984). Wake measurements behind a large horizontal axis wind turbine generator. Sol Energy 33:5–12

Barthelmie, R. J., Rathmann, O., Frandsen, S. T., et al. (2007). Modelling and Measurements of Wakes in Large Wind Farms, Journal of Physics, Conference Series 75, 012049

Barthelmie, R.J., L. Folkerts, F. Ormel, et al. (2003). Offshore wind turbine wakes measured by SODAR, Journal of Atmospheric and Oceanic Technology, 30: p. 466-477

Barthelmie, R.J., Hansen, K., Frandsen, S.T., Rathmann, O., Schepers, J.G., Schlez, W., et al. (2009). Modelling and measuring flow and wind turbine wakes in large wind farms offshore. Wind Energy 12(5), 431-444. doi: 10.1002/we.348

Barthelmie, R. J. and Jensen, L. E. (2010). Evaluation of wind farm efficiency and wind turbine wakes at the Nysted offshore wind farm. Wind Energy, 13: 573–586. doi: 10.1002/we.408

Bastankhah, M., Porte-Agel, F., & Dios Romero, I. (2014). Optimization of wind farm performance based on yaw angle control, EGU General Assembly in Vienna, Austria, id. 14096

Beyer, H.G., Pahkle, T., Schmidt, W., Waldl, H-P., Dewitt, U. (1994). Wake effects in a linear wind farm. Journal of Wind Engineering and Industrial Aerodynamics, 51(3), 303-318. doi: 10.1016/0167-6105(94)90065-5

Bitsuamlak, G. T., Stathopoulos, T., & Bédard, C. (2004). Numerical evaluation of wind flow over complex terrain: Review. Journal of Aerospace Engineering, 17(4), 135-145. doi:10.1061/(ASCE)0893-1321(2004)17:4(135)

Burton, T., Sharpe, D., Jenkins, N., Bossanyi, E. (2001). Wind Energy Handbook, John Wiley & Sons Ltd, England

Cal, R.B., Lebron, J., Castillo, L., Kang, H.S., Meneveau, C. (2010). Experimental study of the horizontally averaged flow structure in a model wind-turbine array boundary layer. J Renew Sustain Energy 2:013–106

Calaf, M, Meneveau, C. and Meyers, J. (2010). Large eddy simulation study of fully developed wind-turbine array boundary layers Phys. Fluids 22 015110

Chamorro, L., Porte-Agel, F. (2010). Flow characterization of wind-turbine wake(s) developed in a boundary layer flow with different thermal stratifications: A wind-tunnel study. The fifth international symposium on computational wind engineering, North Carolina, USA

Chamorro, L., Arndt, R.E.A., & Sotiropoulos F. (2011). Reynolds number dependence of turbulence statistics in the wake of wind turbines. Wind Energy; 15: 733-742.

Chamorro, L., Arndt, R., & Sotiropoulos, F. (2011). Turbulent flow properties around a staggered wind farm. Boundary-Layer Meteorology, 141(3), 349-367. doi:10.1007/s10546-011-9649-6

Chamorro, L., Porté-Agel, F. (2009). A Wind-Tunnel Investigation of Wind-Turbine Wakes: Boundary-Layer Turbulence Effects. Boundary-Layer Meteorol 132(1): 129-149.

Chamorro, L., Guala, M., Arndt, R., & Sotiropoulos, F. (2012). On the evolution of turbulent scales in the wake of a wind turbine model. J. of turbul. 13:1-13

Chamorro, L., Tobin, N., Arndt, R.E.A., & Sotiropoulos, F. (2014). Variable-sized wind turbines are a possibility for wind farm optimization, Wind Energy, 17, pages 1483–1494, doi: 10.1002/we.1646

Choi, E.C.C. (2009). Proposal for unified terrain categories exposures and velocity profiles. The seventh Asia-Pacific conference on wind engineering (APCWE), November 8-12.

Corten, G., Schaak, P., & Hegberg, T. (2004). Turbine interaction in large offshore wind farms. Wind tunnel measurements. Netherlands Agency for Energy and Environment.

Dahlberg, J.A., Poppen, M., & Thor, S.E. (1991). Load/fatigue Effects on a Wind Turbine Generator in a Wind Farm', Proc. EWEC'91, Amsterdam, 251-255.

Dahlberg, J-A., & Thor, S-E. (2009). Power performance and wake effects in the closely spaced Lillgrund wind farm. Proceedings of European Offshore Wind Conference and Exhibition, Stockholm, Sweden.

De Vries O. (1983). On the theory of the horizontal-axis wind turbine. Ann Rev Fluid Mech.; 15:77-96.

Ferreira, A. D., Lopes, A. M. G., Viegas, D. X., and Sousa, A. C. M. (1995). Experimental and numerical simulation of flow around two-dimensional hills, Journal of Wind Engineering and Industrial Aerodynamics, 54/55, 173-181.

Fingersh, L., Simms, D., Hand, M., Jager, D.,Cotrell, J., Robinson, M., Schreck, S., and Larwood, S. (2001). Wind Tunnel Testing of NREL's Unsteady Aerodynamics Experiment, Proceedings of the 20th ASME Wind Energy Symposium, Reno, NV, pp. 194-200

Gebraad, P.M.O., Teeuwisse, F.W., van Wingerden, J.W., & Fleming, P.A. (2014). A data-driven model for wind plant power optimization by yaw control, American Control Conference (ACC). Retrieved from http://www.dcsc.tudelft.nl/~pietergebraad/docs/paperDataDrivenModel YawPREPRINT.pdf

González, J. S., Gonzalez Rodriguez, A. G., Mora, J. C., Santos, J. R., & Payan, M. B. (2010). Optimization of wind farm turbines layout using an evolutive algorithm. Renewable Energy: An International Journal, 35(8), 1671-1681. doi:10.1016/j.renene.2010.01.010

Grant, I., Parkin, P.A. (2000). DPIV study of the trailing vortex elements from the blades of a horizontal axis wind turbine in yaw. Experiments in Fluids; 28:368–376.

Guglsang, P., & Bak, C. (2004). Development of the Riso wind turbine airfoils, Wind Energy; 7: 145-162.

Habash, R.W.Y., Groza, V., Yang, Y., Blouin, C., Guillemette, P. (2011). Performance of a Contra rotating Small Wind Energy Converter. DELTA 2011, IEEE 6th International Workshop on Electronic Design, Test and Application, ISBN-13: 978-0-7695-4306-2, pp. 263-268, Queenstown, New Zealand.

Hansen, K. S., Barthelmie, R. J., Jensen, L. E., & Sommer, A. (2012). The impact of turbulence intensity and atmospheric stability on power deficits due to wind turbine wakes at Horns Rev wind farm. Wind Energy, 15: 183–196. doi: 10.1002/we.512

Holmes, J. (2007). Wind loading of structures. Second edition published by Taylor & Francis

Hsu, S. A., Meindl, E. A., & Gilhousen, D. B. (1994). Determining the power-law wind profile exponent under near-neutral stability conditions at sea. J. Applied Meteor., 33(6), pp. 757-765.

Hu, H., Yang, Z., & Sarkar, P. (2012). Dynamic wind loads and wake characteristics of a wind turbine model in an atmospheric boundary layer wind. Experiments in Fluids, 52(5), 1277-1294. doi:10.1007/s00348-011-1253-5

Irwin, H. (1981). The Design of Spires for Wind Simulation. Journal of Wind Engineering and Industrial Aerodynamics; 7:361-366.

Jackson, P. S., & Hunt, J. C. R. (1975). Turbulent Wind Flow Over a Low Hill. Q. J. R. Meteorological Society, Vol. 101, 929-955

Jain, P. (2007). Wind energy engineering. McGraw Hill. ISBN: 978-0-06-171477-8

Jia, Y.Q., Sill, B.L., Reinhold, T.A. (1998). Effects of Surface Roughness Element Spacing on Boundary Layer Velocity Profile Parameters. Journal of Wind Engineering and Industrial Aerodynamics; 73:215-230

Johnson, K. (2004). Adaptive torque control of variable speed wind turbines, Ph.D. dissertation,Dept.Elec.Eng., Univ. of CO, Boulder, CO.

Jung, S. N., No, T. S., & Ryu, K. W. (2005). Aerodynamic performance prediction of a 30kW counter-rotating wind turbine system. Renewable Energy, 30:631–644.

Kaimal, J., & Finnigan, J. (1994). Atmospheric Boundary Layer Flows: Their structure and measurement. New York: Oxford University Press.

Kang, H.S., & Meneveau, C. (2010). Direct mechanical torque sensor for model wind turbines. Meas. Sci. Technol. 21 105206 (10pp), IOP Publishing Ltd, doi:10.1088/0957-0233/21/10/105206.

Katic, I., Hojstrup, J., & Jensen, N.O. (1986). A simple model for cluster efficiency. Proceedings of European Wind Energy Conference and Exhibition, Rome; 407-410

Kim, H. G., Lee, C. M., Lim, H. C., & Kyong, N. H. (1997). An Experimental and Numerical Study on the Flow over Two-dimensional Hills, Journal of Wind Engineering and Industrial Aerodynamics, Vol. 66, 17-33

Kobayashi, M. H., Pereira, J. C. F., & Siquiera, M. B. B. (1994). Numerical study of the turbulent flow over and in a model forest on a 2D hill, Journal of Wind Engineering and Industrial Aerodynamics, 53(3), 357-375.

Kolar, V. (2007). Vortex Identification: New Requirements and Limitations. Int'l J. Heat and Fluid Flow, vol. 28, pp. 638-652.

Lebron, J., Cal, R., Kang, H., Castillo, L., & Meneveau, C. (2009). Interaction between a wind turbine array and a turbulent boundary layer. 11th Americas Conference on Wind Engineering, San Juan, Puerto Rico.

Lebrón, J., Castillo, L., & Meneveau, C. (2012). Experimental Study of the Kinetic Energy Budget in a Wind Turbine Streamtube. *Journal of Turbulence, 13* (43), 1-22.

Lee, S., Churchfield, M., Moriarty, P., Jonkman, J., & Michalakes, J. (2011). Atmospheric and wake turbulence impacts on wind turbine fatigue loading. NREL/CP-5000-53567

Lignarolo, L.E.M., Ragni, D., Krishnaswami, C., Chen, Q., Simao Ferreira, C.J., & van Bussel, G.J.W. (2013). Experimental analysis of the kinetic energy transport and turbulence production in the wake of a model wind turbine. ICOWES Conference, Lyngby, 16-19 June.

Locke, J., Valecia, U., Ishikawa, K. (2003). Design Studies for Twist-Coupled Wind Turbine Blades. ASME 2003 Wind Energy Symposium (WIND2003), Reno, Nevada, USA, January 6–9

Lun, Y. F., Mochida, A., Murakami, S., Yoshino, H., & Shirasawa, T. (2003). Numerical simulation of flow over topographic features by revised k - ε models, Journal of Wind Engineering and Industrial Aerodynamics, 91(1-2), 231-245.

Makridis, A. (2012). Modelling of wind turbine wakes in complex terrain using computational fluid dynamics. Ph.D. Dissertation

Mamidipudi, P., et.al. (2011). Yaw Control: The Forgotten Control Problems, Europe's Premier Wind Energy Event, EWEA 2011, Brussels, Belgium.

Manwell, J.F., McGowan, J.G., & Rogers, A.L. (2003). Wind Energy Explained: Theory, Design and Application. John Wiley & Sons, Chichester.

Markfort, C.D., Zhang, W., & Porté-Agel, F. (2012). Turbulent flow and scalar transport through and over aligned and staggered wind farms. Journal of Turbulence. 13(1) N33: 1-36. doi:10.1080/14685248.2012.709635.

Mason, P.J. & King, J.C. (1985). Measurements and Predictions of Flow and Turbulence over an Isolated Hill of Moderate Slope. Quart. J. Roy. Meteorol. Soc. Vol. 111, 617-640

Massouh, F., & Dobrev, I. (2007). Exploration of the vortex wake behind of wind turbine rotor. Journal of Physics 75 (2007) 012036 doi:10.1088/1742-6596/75/1/012036

Medici, D., & Alfredsson, P. (2006). Measurement on a wind turbine wake: 3D effects and bluff body vortex shedding. Wind Energy; 9: 219-236.

Medici, D. (2005). Experimental studies of wind turbine wakes-power optimization and meandering, Technical Report of Royal Institute of Technology (KTH), Stockholm

Meneveau, C., & Meyers, J. (2012). Optimal turbine spacing in fully developed wind-farm boundary layers. Wind Energy 15, 305-317. doi:10.1002/we.469

Meyers, J., & Meneveau, C. (2013). Flow visualization using momentum and energy transport tubes and applications to turbulent flow in wind farms. Journal of Fluid Mechanics 715, 335-358.

Moriarty, P.J., Holley, W.E., & Butterfield, S.P. (2004). Extrapolation of extreme and fatigue loads using probabilistic methods. NREL/TP-500-34421

Mwanyika, H.H., & Kainkwa, R.M. (2006). Determination of the power law exponent for southern highlands of Tanzania. Tanz. J. Sci. Vol 32(1)

Ozbay, A., Tian, W., Yang, Z., & Hu, H. (2012). An experimental investigation on the wake interference of multiple wind turbines in atmospheric boundary layer winds. AIAA Paper, AIAA- 2012-2784.

Pedersen, T. F., Gjerding, S., Ingham, P., Enevoldsen, P., Hansen, J. K., & Jorgensen, H. K. (2002). Wind Turbine Power Performance Verification in Complex Terrain and Wind Farms. Roskilde: Risø National Laboratory.

Pérez, B., Mínguez, R., & Guanche, R. (2013). Offshore wind farm layout optimization using mathematical programming techniques. Renewable Energy: An International Journal, 53, 389-399. doi:10.1016/j.renene.2012.12.007

Politis, E. S., Prospathopoulos, J., Cabezon, D., Hansen, K. S., Chaviaropoulos, P. K., & Barthelmie, R. J. (2012). Modeling Wake Effects in Large Wind Farms in Complex Terrain: the Problem, the Methods and the Issues, Wind Energy, Vol. 15, 161–182

Porte-Agel, F., Wu, Y.T., Lu, H., Conzemius, R.J. (2011). Large-eddy simulation of atmospheric boundary layer flow through wind turbines and wind farms. J Wind Eng Ind Aerodyn 99:154–168

Porte-Agel, F., Lu, H., & Wu., Y.T. (2014). Interaction between large wind farms and the atmospheric boundary layer, Elsevier, Volume 10, 307-318. doi: 10.1016/j.piutam.2014.01.026

Robinson, M.C., Hand, M.M., Simms, D.A., & Schreck, S.J. (1999). Horizontal Axis Wind Turbine Aerodynamics: Three-Dimensional, Unsteady, and Separated Flow Influences. NREL/CPP-500-26337. 3rd ASME/JSME Joint Fluids Energy Conference, San Francisco, CA

Rokenes, K. (2009). Investigation of terrain effects with respect to wind farm siting. Doctoral theses at NTNU, 2009:199

Rosen, A., & Sheinman, Y. (1996). The Power Fluctuations of a Wind Turbine. Journal of Wind Engineering and Industrial Aerodynamics, 59: 51–68

Samorani, M. (2013). The wind farm layout optimization problem, Handbook of Wind Power Systems, Energy systems, doi: 10.1007/978-3-642-41080-2_2, Springer – Verlag Berlin.

Sanderse, B. (2009). Aerodynamics of Wind Turbine Wakes: Literature review. Energy Research Center of the Netherlands (ECN), ECN-E-09-016, Petten, The Netherlands, Tech.

Sarpkaya, T., & Daly, J.J. (1987). Effect of ambient turbulence on trailing vortices, Journal of Aircraft, 24(6), 399-404. doi:10.2514/3.45459

Schreck, S., & Robinson, M. (2005) Blade Three-Dimensional Dynamic Stall Response to Wind Turbine Operating Condition. Journal of Solar Energy Engineering; 127: 488-495.

Sheinman, Y., & Rosen, A. (1992). A dynamic model of the influence of turbulence on the power output of a wind turbine. Journal of Wind Engineering and Industrial Aerodynamics, 1992; 39: 329–341.

Shen, W.Z., Zakkam, V.A.K., Sørensen , J.N., & Appa, K. (2007). Analysis of Counter-Rotating Wind Turbines, Journal of Physics: Conference Series, Vol.75, IOP Publishing Ltd, doi:10.1088/1742-6596/75/1/012003

Sherry, M., Sheridan, J., & Jacono, D. (2013). Characterisation of a horizontal axis wind turbine's tip and root vortices. Experiments in Fluids, 54(3), 1-19. doi:10.1007/s00348-012-1417-y

Sill, B.L. (1988). Turbulent Boundary Layer Profiles over Uniform Rough Surfaces. Journal of Wind Engineering and Industrial Aerodynamics; 31:146-163

Spera, D.A. (1994). Wind Turbine Technology: Fundamental concepts of the wind turbine engineering; ASME Press, New York

Szilagyi, J., Katul, G.G., Parlange, M.B., Albertson, J.D., & Cahill A.T. (1996). The local effect of intermittency on the inertial subrange energy spectrum of the atmospheric surface layer. Boundary-Layer Meteorology 79: 35-50, 1996.

Tian, W., Yuan, W., Ozbay, A., & Hu, H. (2013). An Experimental Study on the Performances of Wind Turbines over Complex Terrains, AIAA-2013-0612; 51st AIAA Aerospace Sciences Meeting including the New Horizons Forum and Aerospace Exposition, Grapevine, Texas, USA.

Tian, W., Ozbay, A., Yang, Z., Sarkar, P., & Hu, H. (2012). An Experimental Investigation on the Wake Interference of Multiple Wind Turbines in Atmospheric Boundary Layer Winds. AIAA-2012-2784, 30th AIAA Applied Aerodynamics Conference, New Orleans, Louisiana

Tong, W. (2002). Wind Power Generation and Wind Turbine Design, WIT Press

Vermeer, L. J., Sørensen, J. N., & Crespo, A. (2003). Wind turbine wake aerodynamics. Progress in Aerospace Sciences, 39(6), 467. doi:10.1016/S0376-0421(03)00078-2

Villarreal, C.M.I., & Espiritu, J.F. (2011). Optimization of wind turbine placement using a viral based optimization algorithm, Elsevier, Volume 6, 469-474, doi:10.1016/j.procs.2011.08.087

Wessel A., & Lange B. (2004). A new approach for calculating the turbulence intensities inside a wind farm. In Proceedings of the DEWEK, Wilhelmshaven

Whale, J., Anderson, C.G., Bareiss, R., & Wagner, S. (2000). An experimental and numerical study of the vortex structure in the wake of a wind turbine. Journal of Wind Engineering and Industrial Aerodynamics, Volume 84, 1-21. doi:10.1016/S0167-6105(98)00201-3

Wharton, S., & Lundquist, J.K. (2012). Atmospheric stability affects wind turbine power collection. Environ. Res. Letters 7: doi:10.1088/1748-9326/7/1/014005

Wieringa, J. (1992). Updating the Davenport roughness classification, J. Wind Eng. Ind.Aerodynam., 41-44, 357-368.

Wilson, R.E. (1994). Aerodynamic behavior of wind turbines. In: Spera DA, editor. Wind turbine technology: fundamental concepts of wind turbine engineering. ASME Press, pp215-282

Wood, N. (2000). Wind flow over complex terrain: A historical perspective and the prospect for large-eddy modelling. Boundary-Layer Meteorology, 96(1), 11-32. Retrieved from https://login.ezproxy.net.ucf.edu/login?auth=shibb&url=http://search.ebscohost.com.ezproxy.net.ucf.edu/login.aspx?direct=true&db=aph&AN=15606417&site=ehost-live

Wu, Yu-Ting, & Porté-Agel, F. (2012). Atmospheric turbulence effects on wind-turbine wakes: An LES study. Energies (19961073), 5(12), 5340-5362. doi:10.3390/en5125340

Yang, Z., Sarkar, P., & Hu, H. (2012). Visualization of the tip vortices in a wind turbine wake. Journal of Visualization; 15:39-44.

Zahle, F., & Sørensen, N. (2011). Characterization of the unsteady flow in the nacelle region of a modern wind turbine. Wind Energy 14:271–283

Zhang, W., Markfort, C.D., & Porte-Agel, F. (2012). Near-wake flow structure downwind of a wind turbine in a turbulent boundary layer. Experiments in Fluids; 52:1219-1235.

Zhang, W., Markfort, C., & Porté-Agel, F. (2013). Wind-turbine wakes in a convective boundary layer: A wind-tunnel study. Boundary-Layer Meteorology, 146(2), 161-179. doi:10.1007/s10546-012-9751-4

Zhou, Y., & Kareem, A. (2002). Definition of Wind Profiles in ASCE 7. Journal of Structure Engineering; 128:1082-1086.

Zhou, J., Adrian, R.J., Balachandar, S., & Kendall, T.M. (1999). Mechanisms for generating coherent packets of hairpin vortices in channel flow. J. Fluid Mech. 387, 353–396.